The Dissertation Committee for Xiaolei Peng Certifies that this is the approved version of the following Dissertation:

Optothermal Manipulation of Colloidal Particles and Biological Objects

Committee:

Yuebing Zheng, Supervisor

Xiaoqin Li

Michael F. Becker

Adela Ben-Yakar

Chong Xie

Optothermal Manipulation of Colloidal Particles and Biological Objects

by

Xiaolei Peng

Dissertation

Presented to the Faculty of the Graduate School of

The University of Texas at Austin

in Partial Fulfillment

of the Requirements

for the Degree of

Doctor of Philosophy

The University of Texas at Austin

August 2019

Acknowledgements

First, I would like to thank my PhD adviser, Prof. Yuebing Zheng for providing me the invaluable opportunity to work on the project titled "Virtual Plasmonic Tweezers for Versatile Manipulation of Cells and Biomolecules", which was funded by Arnold and Mabel Beckman Foundation. Prof. Zheng has given me considerable freedom in starting a new optical lab and exploring various research areas. I am extremely grateful for his unparalleled guidance and support in transforming an undergraduate with a physics background to a materials scientist and an optical engineer.

I must also thank the insightful suggestions from my committee members including Prof. Xiaoqin Li, Prof. Michael F. Becker, Prof. Adela Ben-Yakar, and Prof. Chong Xie. I am grateful to Prof. Becker for his instructions on Fourier Optics and spatial light modulators. I also appreciate the help received from the students in Prof. Li's, Prof. Ben-Yakar's, and Prof. Xie's group. They were always ready to answer any questions related to optics, microfluidics, and biological cells.

I feel highly honored to collaborate with Dr. Linhan Lin on elucidating the underlying physics of optothermo-matter interaction and rational optical engineering for optothermal manipulation of colloidal particles and living cells. The constructive advice and strict training from him cannot be overestimated in conducting my doctoral research.

I also wish to extend my sincere thanks to other group members, Dr. Mingsong Wang, Dr. Zilong Wu, Dr. Eric Hill, Dr. Kan Yao, Dr. Yunlu Sun, Dr. Abhay Kotnala, Yaoran Liu, Bharath Bangalore Rajeeva, Jingang Li, Zhihan Chen, Pavana Siddhartha Kollipara, Hongru Ding, Jie Fang, Jimi Wang, Youngsun Kim, and Rohit Unni.

I very much appreciate the assistance from Wei Li in Prof. Deji Akinwande's group, Taizhi Jiang in Prof. Brian Korgel's group, Pranaw Kunal in Prof. Simon Humphrey's group, Emanuel Lissek in Prof. Ludwig Florin's group and Prof. Daniel Heinzen.

Thanks also should go to Prof. Jinbo Yang, Prof. Qinghong Cao, Prof. Xi Lin from the School of Physics, Prof. Ya Xu from the Department of English at Peking University, for their recommendations and encouragement in applying for the Materials Science and Engineering program at UT.

I am deeply indebted to my family for their unconditional support and love, as my success and achievements would not have been possible without them.

Abstract

Optothermal Manipulation of Colloidal Particles and Biological Objects

Xiaolei Peng, Ph.D.

The University of Texas at Austin, 2019

Supervisor: Yuebing Zheng

Optical based manipulation techniques play an important role in bottom-up assembly of micro- and nano-structures, discovery of new materials, and biomedical diagnostics. Traditional optical tweezers have limitations for the requirement of rigorous optics and high optical power. Optothermal manipulation, which exploits light-heat conversion and particle migration under a light-directed temperature field, is an emerging strategy for achieving diverse manipulation functionalities in a low-power fashion. In this work, we have developed a series of optothermal manipulation techniques, including bubble-pen lithography, opto-thermophoretic tweezers, opto-thermoelectric tweezers, and opto-thermoeletric printing. In bubble-pen lithography, microbubbles generated at solid-liquid interfaces through laser heating of a plasmonic substrate are used to pattern diverse colloidal particles on the substrate. Through directing the laser beam to move the bubble, we create arbitrary single-particle patterns and particle assemblies with different resolutions and architectures. The key to optothermal tweezers is the ability to achieve negative Soret effect, or deliver colloidal particles from cold to hot regions in a temperature field. Two types of optothermal tweezers with different driving forces are explored for versatile manipulation of colloidal particles and biological objects. Opto-thermophoretic

tweezers rely on an abnormal permittivity gradient built by layered solvent molecules at the particle-solvent interface, while opto-thermoelectric tweezers exploit a thermophoresis-induced thermoelectric field for low-power trapping of nanoparticles. Furthermore, we have demonstrated opto-thermoelectric printing of colloidal particles on substrates in salt solutions and hydrogel solutions. With the low-power operation, simple optics, and diverse functionalities, optothermal manipulation techniques will find a myriad of applications in colloidal science, materials science, nanotechnology, and life sciences, as well as in developing functional colloidal devices and biomedical devices.

Table of Contents

List of Tables

List of Figures

Figure 3.8: Working principle of cell trapping with the thermophoretic tweezers. (a) Simplified structure of the lipid bilayer in the membrane of a biological cell. The phosphate groups in the phospholipid provide the negative charges on the cell membrane and induce an electric field **E** to drive the water molecules toward the membrane. (b) Orientated water molecules form in the electric double layer of the cell membrane under the electric field. The permittivity of the water in the electric double layer (ε_{ed}) strongly depends on the orientation of the molecules, which is different from that of the bulk water (ε_{bulk}). (c) Thermal response of the permittivity in the electric double layer (*i.e.*, permittivity gradient $\nabla\varepsilon_{ed}$) on the cell membrane under a temperature gradient field ∇T, which induces the thermal perturbation and increases the entropy of the water molecules. The sign of $\nabla\varepsilon_{ed}$ is opposite to that of $\nabla\varepsilon_{bulk}$. (d) The permittivity gradient $\nabla\varepsilon_{ed}$ generates a slip velocity v_s pointing from hot to cold and the cell migrates in an opposite direction with a velocity v_p, which leads to the trapping of the cell at the hot laser spot. The electric static repulsive force between the cell membrane and the substrate, both of which have negative charges, balances the trapping force. 37

Figure 5.8: Opto-thermoelectric assembly and immobilization of various colloidal superstructures in hydrogel solutions. Assembly of (a) 1 μm, (b) 2 μm, and (c) 5 μm PS spheres into 2D close-packed superstructures. (d) 1D assembly of 2 μm PS spheres. (e) 2D hybrid assembly of a Saturn-ring superstructure with a 5 μm PS sphere and eight 2 μm PS spheres. (f) 3D assembly of a close-packed tetrahedron superstructure with four 2 μm PS spheres. (g) 2D hybrid assembly of a 5 μm PS sphere surrounded with four 2 μm silica spheres. (h) 2D hybrid assembly of two 5 μm PS spheres and two 2 μm silica spheres. (i-j) 2D hybrid assembly of a 1 μm, 2 μm, and 5 μm PS sphere into two close-packed superstructures with an opposite chirality. The pink images are the corresponding optical microscopy images. The inset in (c) shows the scanning electron micrograph of the corresponding superstructure after cross-linking of the hydrogel. All the colloidal superstructures were assembled in hydrogel solutions of 20 mM CTAC and patterned *via* UV-induced cross-linking. For assembly, 20 mM is an optimized concentration for strong depletion attraction between the assembled particles. A 532 nm laser beam with a diameter of 2 μm was used for assembly. Scale bars: 5 μm.....99

Chapter 1: Introduction to Optothermal Manipulation[1]

Optical manipulation arises from direct or indirect light-matter interactions, which provide a light-directed driving force to deliver or trap colloidal particles. In optical tweezers, the deflection of incident light at the particle-environment interface generates an optical gradient force, which can directly trap particles at the beam center.[1] Optical tweezers are versatile in manipulating a wide range of particles in three-dimensions (3D).[2] However, the strength of the optical gradient force highly depends on the optical setup and the intensity of the trapping laser.[3] The working power of optical tweezers is generally high (10^2-10^3 mW), which can damage fragile objects such as functional colloids and biological cells.[4]

Several different strategies have been established to overcome the limitations of optical tweezers. The excitation of localized surface plasmons at metal nanoantennas can significantly amplify the electromagnetic field in the vicinity of the nanoantennas, providing a plasmon-enhanced optical gradient force for near-field optical trapping and thus reducing the operational power of plasmonic tweezers.[5] However, the localized nature of plasmonic hot spots limits the dynamic manipulation capability of plasmonic tweezers.[6] Another strategy is to introduce a light-controlled electric field or temperature field for indirect optical manipulation. For example, optoelectronic tweezers exploit the dielectrophoretic migration of particles under a non-uniform optoelectronic field for low-power manipulation.[7] Optical manipulation through optical heating, or optothermal manipulation, is alluring because photon-phonon conversion is an entropically favorable

[1] Chapter 1 was published in the journal: L. Lin, E. H. Hill, **X. Peng**, and Y. Zheng, Optothermal Manipulations of Colloidal Particles and Living Cells, *Acc. Chem. Res.*, 2018, 51, 1465-1474. I am a co-author of this review paper.

process and heat-directed migration is applicable to variable particles in different fluidic environments.

Optothermal manipulation is a two-step process, that is, photon-phonon conversion to optically build a temperature field and directed particle migration under the temperature field. The migration of colloidal particles under a temperature field involves multiple physical processes.[8, 9] It has been shown that the migration of particles is sensitive to a variety of parameters such as surface charge of the particles, solvent composition, environmental temperature, and morphology of the fluidic chamber, making it challenging to design a general optothermal platform for colloidal manipulation.[10, 11] Over the past 20 years, researchers have developed theories that describe the directed migration of colloidal particles within a temperature field.[12-15] Optothermal manipulation techniques for controlling colloidal particles under specific conditions have recently been demonstrated.[16-19] Herein, we discuss the working principles, design concepts, and applications of various optothermal manipulation techniques, including bubble-pen lithography, opto-thermophoretic tweezers, opto-thermoelectric tweezers, and opto-thermoelectric printing.

Chapter 2: Bubble-Pen Lithography[2]

Lithography[20-23] and chemical synthesis[24, 25] are considered as two primary strategies for nanofabrication. Photolithography has remained as the driving force for semiconductor industry. However, its resolution is reaching an ultimate limit. E-beam lithography and ion-beam lithography feature high resolution and arbitrary patterning, however, are limited by high cost and low throughput. Chemical synthesis has advantages in both low cost and precise control of compositions, sizes, and shapes of nanomaterials. With their precisely tailorable properties down to the atomic level, colloidal micro-/nano-particles are promising as building blocks for functional devices.[26-28] However, the device applications require the patterning of particles on solid-state substrates. For this purpose, a wide range of techniques have been developed, including self-assembly,[29-33] Langmuir-Blodgett (LB) method,[34] dip-pen nanolithography,[35, 36] polymer pen lithography,[37] and contact-printing.[38]

Optical tweezers have been proven effective in manipulating the colloidal micro-/nano-particles in solutions.[1, 39, 40] Despite its capability of offering remote, real-time, and versatile manipulation of colloidal particles, conventional optical tweezers require high laser power (100 mW/μm^2) that can damage the colloidal particles and have remained challenging to immobilize the particles onto the substrates. Although a combination of optical trapping and convective fluid flow leads to immobilized particles of a single type of featureless close-packed aggregates on the substrates upon the solvent evaporation,[41] there remains a critical need for new light-based techniques that can create arbitrary patterns of colloidal particles immobilized on the substrates. Recently, Feldman and his

---

[2] Chapter 2 was published in the journal: L. Lin*, **X. Peng***, Z. Mao, W. Li, M. N. Yogeesh, B. B. Rajeeva, E. P. Perillo, A. K. Dunn, D. Akinwande, and Y. Zheng, Bubble-Pen Lithography, *Nano Lett.*, 2016, 16, 701-708. I am a leading author.

co-workers used the optical tweezers to trap the metallic nanoparticles at the resonance wavelength, guide them to the substrate, and bind the particles *via* van der Waals attraction to the substrate.[42] Optoelectronic tweezers represent another milestone in extending the capability of optical tweezers.[7, 43-45] Based on the optically patterned virtual electrodes on a photosensitive substrate, optoelectronic tweezers can grab and immobilize colloidal particles on the surface of hydrogenated amorphous silicon.[46]

2.1 WORKING PRINCIPLE OF BPL

Herein, we have developed BPL to optically write arbitrary patterns of colloidal particles on the substrates. In BPL, an optically controlled microbubble is generated to capture and immobilize colloidal particles on the plasmonic substrates through the coordinated actions of Marangoni convection, surface tension, gas pressure, and substrate adhesion in the substrate-bubble-solution system. The irradiation of a plasmonic substrate with a focused laser beam at the plasmon resonance wavelength generates a microbubble at the substrate-solution interface. Due to the plasmon-enhanced photothermal effects, the bubbles of variable sizes can be generated at a significantly reduced power. We can generate bubbles down to 1 μm in diameter, which are much smaller than the microbubbles (diameter in the range of 50-100 μm) commonly used in microfluidic devices for manipulation of particles.[47-49]

Fig. 2.1a illustrates the experimental setup for BPL. A laser beam is focused onto the plasmonic substrate by a high-magnification objective from the bottom of the sample. An optical microscope with a white light source, objectives, and a CCD is integrated into the system for real-time monitoring of the patterning process. Colloidal particles suspended in deionized (DI) water were sandwiched between a plasmonic substrate and a cover slip with a spacer of 120 μm. As illustrated in Fig. 2.1b, a microbubble is generated on the

plasmonic substrate upon the irradiation of a laser beam of 2 μm in diameter due to water vaporization from the plasmon-enhanced photothermal effects.[50, 51] The colloidal particles are dragged toward the microbubble, trapped at the bubble/water interface and eventually immobilized on the substrate. By controlling the laser beam, we can move the microbubble to create patterns of particles dictated by the trajectories of bubble movement.

The optical generation of microbubbles at the solid-water interface using plasmonic substrates consisting of Au nanoparticles was reported previously.[50, 52, 53] Herein, we employ plasmonic substrates consisting of quasicontinuous Au nanoislands (AuNIs), which are tuned to match their plasmon resonance wavelength with the laser wavelength (532 nm) and to have a high nanoparticle density in order to minimize the critical optical power for the bubble generation. The typical plasmonic substrate has Au nanoparticles of 20-40 nm in diameters and 5-10 nm in interparticle distances with a particle density of 1×10^{11} particles/cm^2 (Fig. 2.1c), which is much higher than the particle density in the plasmonic substrates in previous work.[50, 52] As shown by simulated electromagnetic field distribution over SEM image of the AuNIs (Fig. 2.1c), the laser irradiation leads to a high-density electromagnetic "hot spots" that arise from strong near-field coupling between neighboring Au nanoparticles. The network of "hot spots" on the AuNIs allows spatially continuous generation and movement of microbubbles for arbitrary patterning. Both simulated and experimental absorption spectra (Fig. 2.1d) reveal that the plasmon resonance peak wavelength of the AuNIs matches the laser wavelength, which significantly enhances light absorption and photothermal effects for low-power bubble generation.

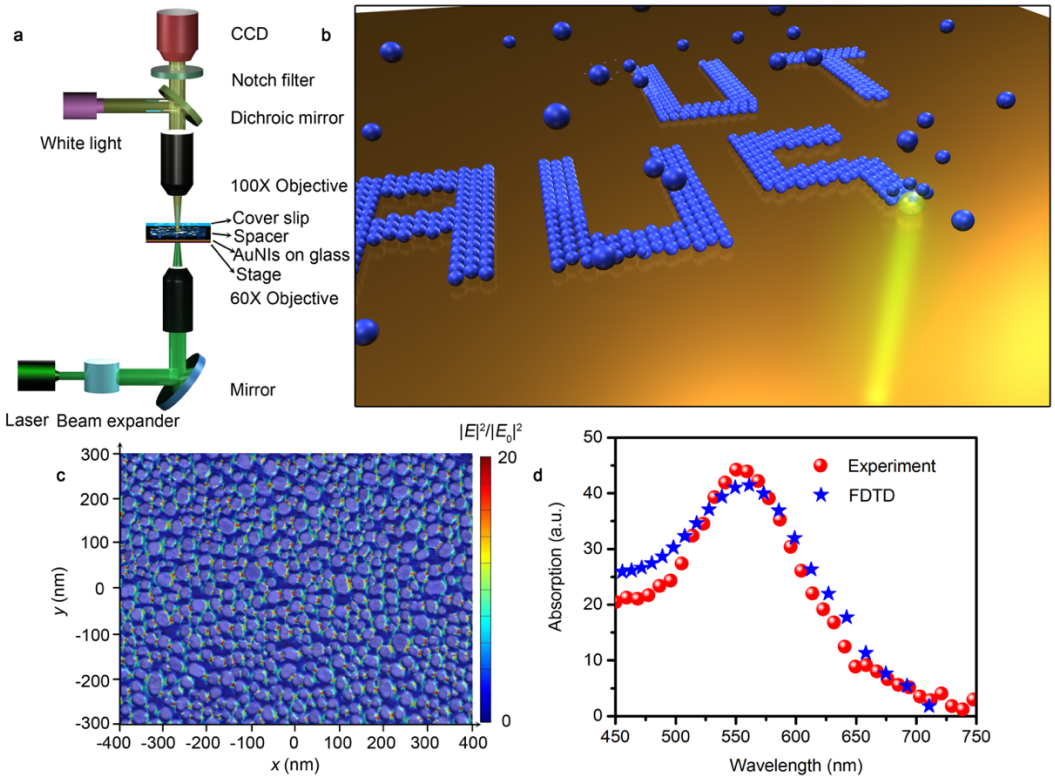

Figure 2.1: Working principle of BPL. (a) An overview of experimental setup for BPL. (b) Schematic illustration of pattern-writing process using an optically controlled microbubble on a plasmonic substrate. The small blue spheres represent colloidal particles. (c) An overlay of scanning electron microscopy (SEM) image and simulated electric field distribution of quasicontinuous Au nanoislands (AuNIs). (d) Simulated and experimental absorption spectra of the AuNIs substrate.

In BPL, both natural convection and Marangoni convection are responsible for particle trapping at the microbubbles. The former is caused by a temperature gradient on the plasmonic substrate. The latter is induced by a surface-tension gradient along the microbubble surface (Fig. 2.2a). The convective flow drags colloidal particles down to the plasmonic substrate and the in-plane drag force drives particles toward the microbubble. The trapping occurs when a particle touches the microbubble, as shown in the inset of Fig. 2.2a. The surface tension force F_S at the gas/liquid interface leads to an effective drag force

F_D, which attracts the particle toward the microbubble. The pressure inside the microbubble, which can reach 3.4 bar for a 1 μm bubble,[52] is much higher than the pressure in water, which can be treated as atmospheric pressure. The balance is achieved when the ratio between F_D and F_P becomes 1:

$$\frac{F_D}{F_P} = \frac{R_B}{R}\frac{sin(|\theta_C - \beta|)}{sin\,\beta} = 1 \quad (1)$$

where R_B is the radius of the microbubble, F_P is the force induced by the gas/liquid pressure difference, R is the radius of the colloidal particle, θ_C is the contact angle between the particle and the bubble, and β is the half-central angle.

We used computational fluid dynamics (CFD) simulations to obtain the temperature distribution around a 1 μm bubble (Fig. 2.2b) when the substrate is illuminated by a focused laser beam with a diameter of 2 μm and power density of 0.56 mW/μm^2 (measured at the focus plane of the objective). The resultant bottom-to-top temperature difference of ~60 ^oC creates a surface tension gradient along the bubble surface. The flow velocity distribution around this microbubble is displayed in Fig. 2.2c, with a maximum flow velocity of ~0.3 m/s at the gas/liquid interface. The flow velocity decreases when the distance from the microbubble is increased. It ranges from 1 to 100 μm/s at the distances of 15-5 μm. Due to the convective flow, the particles are dragged toward the microbubble according to Stokes' law:

$$F_D = 6\pi\mu R v(R) \quad (2)$$

where μ is the dynamic viscosity of the solution and $v(R)$ is the flow velocity of solvent relative to the particles, which is also dependent on R. As shown in Fig. 2.2c, the larger particles have the mass center farther away from the substrate surfaces, experiencing a different flow velocity from the smaller particles. At a constant mass density, the acceleration of the particles is estimated as $a \propto \mu R^{-2} v(R)$.

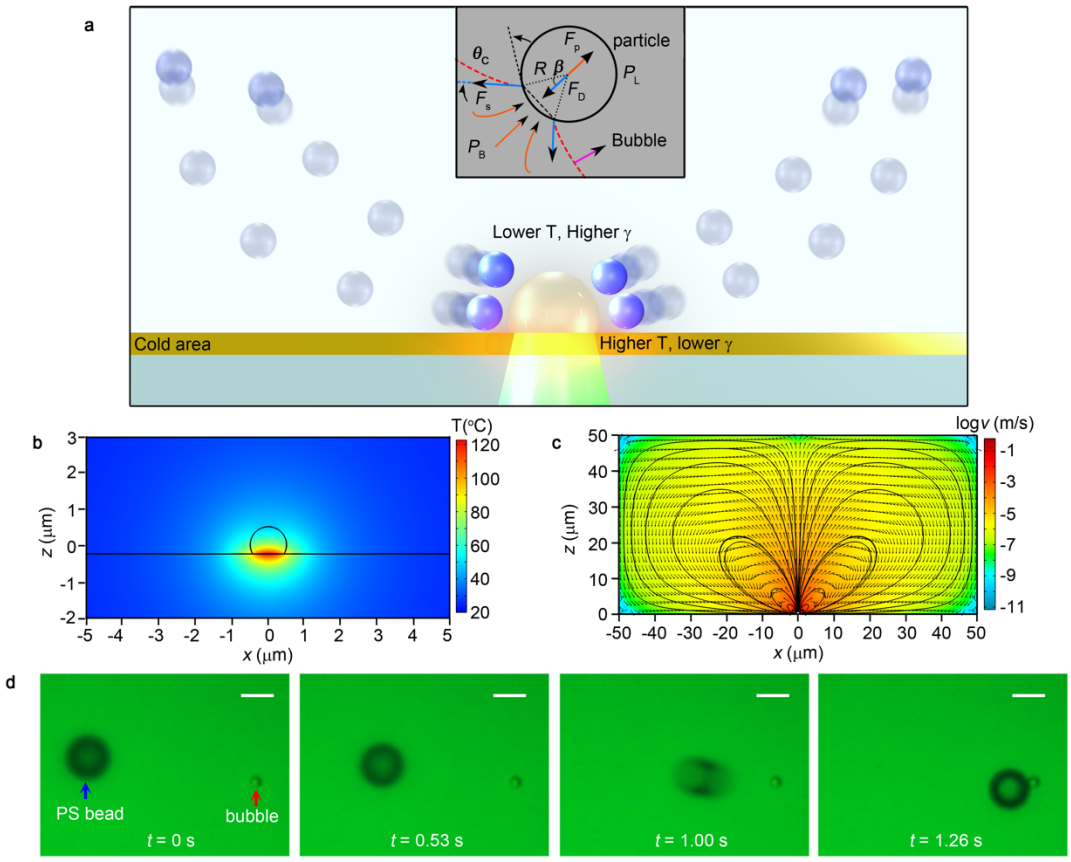

Figure 2.2: Particle trapping at a microbubble that is generated through plasmon-enhanced photothermal effects. (a) Schematic illustration (in a cross-sectional view) of the particle-trapping mechanism by a single microbubble. The blue spheres indicate the suspended particles in the DI water. The particles follow the convective flow due to the frictional force. The inset shows the force analysis when a particle is trapped by the microbubble (indicated as the red dash line). P_B and P_L indicate the pressure in the bubble and liquid, respectively, which introduce a net force of F_P pushing the particle outward. The surface tension F_S introduce a drag force F_D. (b) Simulated temperature distribution around a 1 μm bubble in a cross-sectional view. (c) Simulated flow velocity distribution around a 1 μm bubble with logarithmic scale in a cross-sectional view. The black lines indicate streamlines of the convective flow. (d) Time-resolved trapping process of a single 5.31 μm PS bead by a 1 μm bubble. Scale bar: 5 μm.

We measured the particle-trapping speed by recording the time-resolved trapping processes of single PS beads with diameters of 5.31 μm (Fig. 2.2d). A traveling distance

of ~20 μm is used to estimate the average trapping speed. The 5.31 μm PS bead exhibits an average speed of 18.1 μm/s. The drag force and trapping speed depend on the distance between the particle and the microbubble. There is a dramatic increase of the trapping speed when the particle approaches the microbubble (Fig. 2.2d), indicating that the relative velocity v dominates the trapping process.

2.2 Patterning of PS Micro-/Nano-Particles on Plasmonic Substrates

We exploit plasmon-enhanced photothermal effects, which improve the adhesion between the PS beads and the substrate, to immobilize the bubble-trapped particles on the substrates for particle patterning. Fig. 2.3a shows the optical micrographs of the variable microbubbles generated under the light illumination with different power densities. The bubble pattern in Fig. 2.3a was generated in series by translating the sample stage and recorded in sequence. The smallest bubble with a diameter of 1 μm is generated at the laser power density of 0.56 mW/μm^2. An increase in the optical power density enlarges the bubbles because an increased amount of water steam was generated and air molecules diffused into the bubbles. As shown in Figs. 2.3b-c, the 540 nm PS beads can be immobilized on the substrate by the bubbles, leading to different patterns. At the lowest optical power density, three PS beads form a cluster with 2D configuration. When the power density is increased to 0.97 mW/μm^2, a large bubble with a diameter of >3 μm leads to a three-dimensional (3D) hollow structure of the beads on the substrate (Fig. 2.3d), revealing that the trapped PS beads are aligned along the whole gas/liquid interface. Besides the bubble size, the patterns of beads also depend on the concentration of the beads in the solution and the laser irradiation time.

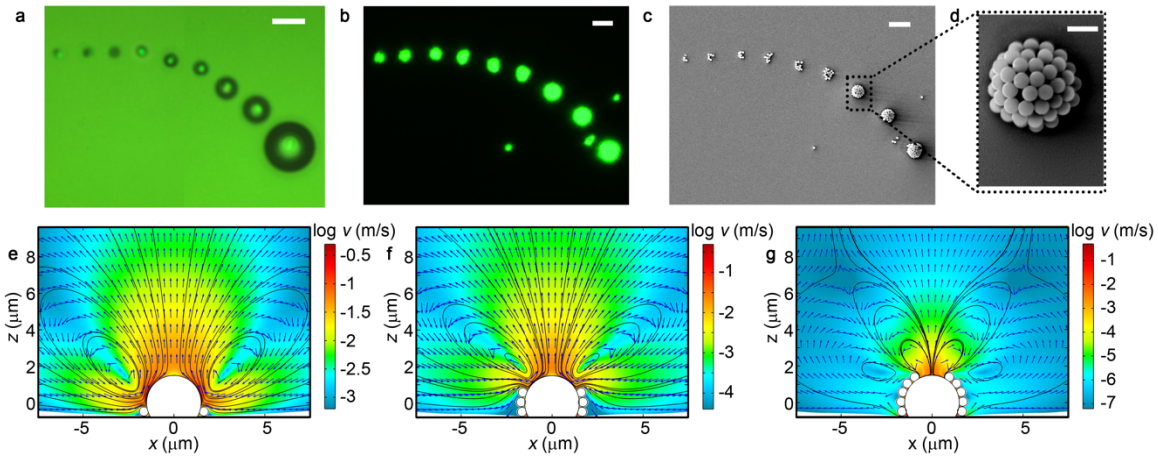

Figure 2.3: Patterning of the PS beads on the substrate at different laser powers. (a) Optical micrographs of a series of microbubbles generated with different laser power densities: 0.56, 0.64, 0.68, 0.77, 0.83, 0.91, 0.97, 1.04, and 1.12 mW/μm^2 (from small to large bubbles). (b) Dark-field optical micrographs and (c) SEM image of the series of patterned 540 nm PS beads generated with corresponding power densities in (a). (d) High-magnification image of the 3D hollow structure formed at a laser power density of 0.97 mW/μm^2. The flow velocity distribution (logarithmic scale) around a 3μm microbubble in a cross-sectional view when (e) single layer (f) three layers and (g) five layers of 540 nm PS beads are trapped at the gas/liquid interface. Scale bar: (a)-(c) 5 μm; (d) 1 μm.

We apply CFD simulations to gain an insight into the formation mechanism of the 3D hollow structures of PS beads. As illustrated in Figs. 2.3e-g, the convective flow drags the beads toward the bubble/substrate interface and generates the 3D hollow structure by the "bottom-up" layer-by-layer stacking. Such a stacking process is enabled by the fact that the initially trapped beads at the bubble surface block the Marangoni stress and modify the convective flow distribution in a way that the convective flow points toward the upper part of the bubble. In addition, the trapped beads reduce the surface tension gradient and thus the flow velocity along the bubble surface. However, a reverse convective flow occurs when the bubble traps five layers of beads (Fig. 2.3g). The reverse flow pushes the free beads in suspension away from the trapped ones. The velocity around the microbubble is

4-5 orders of magnitude lower than that before the beads are trapped, indicating that the trapping process stops once the bubble surface is covered with beads. The 3D hollow structures are generated when the microbubbles are significantly larger than the beads. When the bubbles and beads have comparable sizes, one-layer or two-layers 2D aggregates are generated due to the limited surface area of the bubbles.

Taking advantage of the quasicontinuous nature of the plasmonic substrate, we have achieved continuous writing of colloidal particle patterns on the substrate by scanning the laser beam or translating the sample stage. Fig. 2.4a illustrates the writing process for a straight line of 540 nm PS beads at a laser power density of 0.56 $mW/\mu m^2$. At a lower power density (top panel of Fig. 2.4a), no microbubble was generated. Still, the optically generated temperature gradient led to the natural convection, moving the PS beads upward at the illuminated area without trapping and immobilization. When the laser power density was increased to the critical value, a microbubble was generated and the PS beads were collected and immobilized on the illuminated spot (second panel in Fig. 2.4a). During the translation of the sample stage, the original microbubbles disappeared, leaving behind the immobilized beads, and new ones were generated at the new locations to trap and immobilize the beads, leading to patterns of the beads that follow the trails of the bubbles (third and fourth panels in Fig. 2.4a). As an example, we wrote an "SP" patterns of 540 nm PS beads using a 1 μm microbubble (Fig. 2.4b). Since the sizes of the PS beads and the microbubble are comparable, the patterns feature a 2D configuration. Due to the high trapping and immobilization efficiencies, the microbubble enable rapid scanning of the laser beam and high-throughput patterning at a large scale.

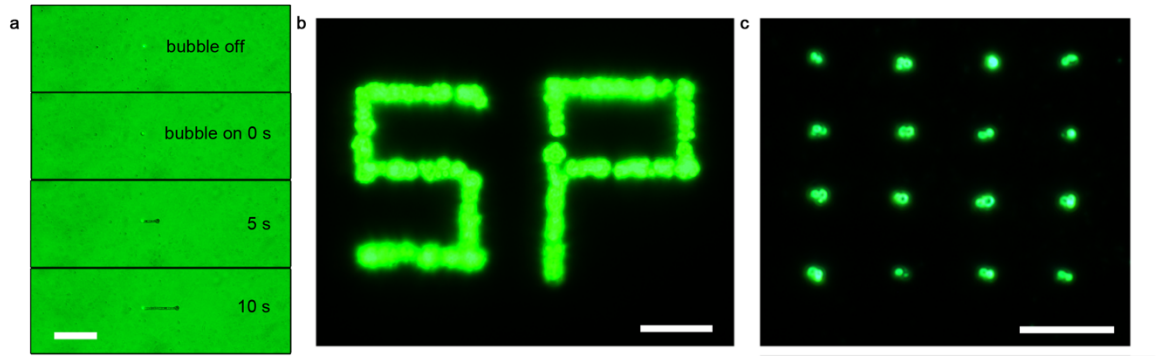

Figure 2.4: Patterning of PS beads of different sizes on the plasmonic substrates. (a) Time-resolved process for continuous writing of a straight-line pattern of 540 nm PS beads on the AuNIs substrate. (b) Dark-field optical image of an "SP" pattern of 540 nm PS beads. (c) Dark-field optical image of a 4×4 array of 3D hollow structures of 60 nm PS beads. Scale bar: (a) 50 μm; (b) and (c), 10 μm.

In another example, Fig. 2.4c shows a 4×4 array of the PS beads with a diameter of 60 nm. Since the beads (60 nm) are much smaller than the microbubble, the 3D hollow structures are obtained. Moreover, the 3D hollow structure can be continuously written on the substrate, leading to the hollow-ridge patterns of the beads. Such 3D hollow structures may find applications in omnidirectional optical device, wide-angle-view imaging, and microlens.[54-56]

We evaluate the resolution of BPL based on our current experimental setup. As shown in Fig. 2.5a, patterning of single PS beads with a size ranging from 540 nm to 9.51 μm has been achieved. Individual beads can also be patterned into "BPL" (bead diameter: 0.96 μm) and "UT" (bead diameter: 5.31 μm) logos (Figs. 2.5b-c). With the capability of patterning single beads, BPL can be a pivotal tool in single-particle sensing[57] and single-cell analysis.[58] It will be interesting to test the ultimate resolution of BPL, which will require better imaging and concentration control for the nanoparticles below 100 nm.

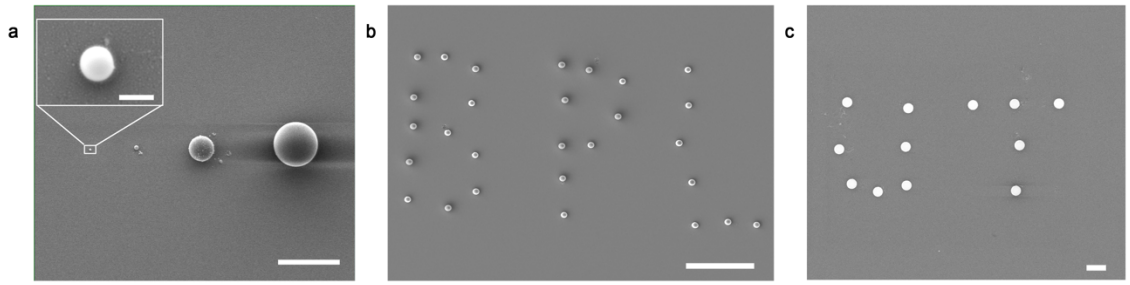

Figure 2.5: Patterning of PS beads at single-particle resolution. (a) Patterning of single PS beads with different sizes: 540 nm, 0.96 μm, 5.31 μm, and 9.51 μm, respectively (from left to right). (b) SEM image of a "BPL" pattern of 0.96 μm PS beads. (c) SEM image of a "UT" pattern of 5.31 μm PS beads. Scale bar: (a)-(c) 10 μm; inset of (a) 500 nm.

2.3 PATTERNING OF PS MICROPARTICLES ON 2D ATOMIC-LAYER MATERIALS

BPL is applicable to patterning particles on the surfaces beyond plasmonic substrates. We have achieved arbitrary patterning of PS beads on 2D atomic-layer materials. For a demonstration, we grew MoS_2 atomic monolayers with chemical vapor deposition (CVD) and transferred them onto the AuNIs substrate (Fig. 2.6a). As illustrated in Fig. 2.6b, an "MoS_2" pattern of individual PS beads with a diameter of 0.96 μm was created on the MoS_2 monolayer using BPL. In Fig. 2.6c, photoluminescence (PL) spectrum taken from the patterned area, as indicated by the red circle in Fig. 2.6b, reveals that there is no damage to the 2D monolayer during patterning by BPL. A sub-nanoscale thickness (6.7 Å) of the 2D monolayer with a thermal conductivity of 34.5 W/mK[59] makes it possible to generate microbubbles on its top. In principle, BPL is applicable to a variety of particles and 2D materials. By synergizing the unique properties of 0D and 2D systems, the heterostructures of micro-/nano-particles and 2D materials could exhibit novel functions for different applications. In addition, the particles can work as masks for further patterning of 2D monolayer through selective etching or deposition of new materials.

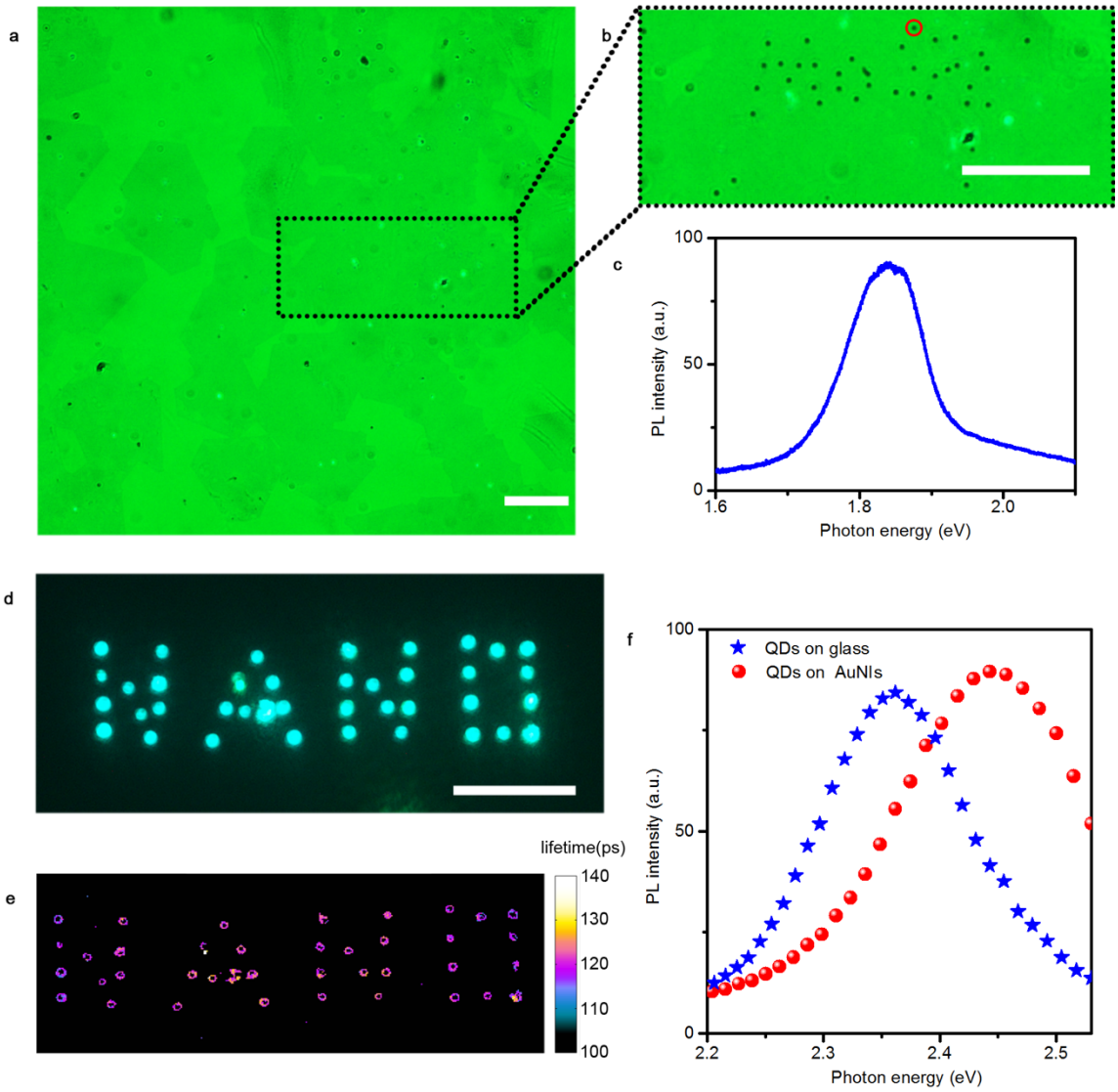

Figure 2.6: Versatility of BPL in patterning 2D materials and quantum dots. (a) Optical micrograph of 2D MoS_2 monolayers on the AuNIs substrate. (b) Optical micrograph of an "MoS_2" patterns of individual 0.96 μm PS beads written on the 2D MoS_2 monolayers. (c) PL spectrum of the MoS_2 recorded from the regime with a single PS bead, as indicated by the red circle in (b). (d) Fluorescence image of a "NANO" pattern of 6 nm CdSe/ZnS quantum dots on the AuNIs. (e) Fluorescence lifetime image of the patterned CdSe/ZnS quantum dots as shown in (d). (f) PL spectra of the quantum dots patterned on the plasmonic substrate and of the quantum dots on glass substrate. Scale bar: 50 μm.

2.4 Patterning of Quantum Dots on Plasmonic Substrates

To further demonstrate the versatility of BPL, we have accomplished its use for arbitrary patterning of quantum dots with a size much smaller than that of the PS beads. As an example, we used CdSe/ZnS core/shell quantum dots with a diameter of 6 nm for BPL. As shown in Fig. 2.6d, an "NANO" pattern of the quantum dots was created on the AuNIs substrate. We measured the fluorescence lifetime of the patterned quantum dots using time-correlated single-photon counting technique (Fig. 2.6e). An average lifetime of ~120 ps for the patterned quantum dots is much shorter than that of the original quantum dots (8.1 ns). The reduced lifetime implies the strong plasmon-exciton interactions within the coupled system consisted of quantum dots and plasmonic substrates.[60] The plasmon-exciton coupling is further confirmed by PL spectra of the quantum dots, which made a blueshift from 2.35 to 2.45 eV upon patterning on the AuNIs (Fig. 2.6f). With their well-controlled and highly tailorable nanostructures, the patterned quantum dots on plasmonic substrates can not only serve as platforms for fundamental study of plasmon-exciton coupling, but also find applications in nanophotonics and optoelectronics such as ultrafast light sources.

2.5 Conclusion

In summary, we have developed a versatile lithography technique known as BPL for arbitrary patterning of colloidal particles on the solid-state substrates using optically controlled microbubbles. Through combining experiments and numerical simulations, we have established that the coordinated actions of Marangoni convection, surface tension, gas pressure, and substrate adhesion hold the key to the trapping and immobilization of particles in BPL. Using plasmon-enhanced photothermal effects on the properly engineered plasmonic substrates, BPL can operate efficiently in a continuous-scanning mode and at low laser power. The versatility of BPL is reflected in its capability of writing

arbitrary patterns of single and clusters of particles in 2D or 3D configurations and on its applicability to various colloidal particles and substrates beyond plasmonic nanostructures. The high tunability of bubble size, substrate temperature, and flow convention in BPL has significantly enriched the configurations of particles in the patterns. The ultimate resolution of BPL has remained to be tested.

It is worthy of noting that the current study exploits photothermal effects for the immobilization of particles on the substrates, which is applicable to thermoresponsive particles like PS beads and CdSe/ZnS quantum dots with polymer coating. We believe that surface-functionalization methods can be employed to enhance the substrate-particle interactions for the immobilization of a wide range of particles, including electrostatic attraction and chemical recognition. Besides serving as a platform for fundamental research on colloidal nanoscience, the patterned particles on AuNIs substrates can be used as-prepared or transferred to different substrates for functional device applications. For the former, the plasmonic effects can be exploited to enhance the performance of the particles such as the shortened fluorescence lifetime of quantum dots on the AuNIs substrates. The capability of patterning colloidal particles on 2D materials opens up new opportunities for functional hybrid materials and devices that benefit from the synergistic integration of 0D and 2D materials.

Chapter 3: Opto-Thermophoretic Tweezers

3.1 Opto-Thermophoretic Manipulation of Colloidal Particles in Non-Ionic Liquids[3]

Recent years have witnessed tremendous efforts in exploiting thermophoretic forces for optical-based manipulation.[17, 61-65] Confinement and control of single nanoparticles have been achieved with dynamic temperature fields by Cichos's group.[62, 63] Noninvasive thermophoretic transport of DNAs and vesicles, has been recently of particular interest to the community of optothermal manipuation.[17, 61, 64, 65] In response to an optically controlled temperature gradient ∇T, colloidal particles undergo thermophoresis and migrate to either the cold or the hot region with a drift velocity $\boldsymbol{u} = -D_{\mathrm{T}}\nabla T$, where D_{T} is the thermophoretic mobility. Opto-thermophoretic tweezers enable versatile low-power manipulation of colloidal particles and living cells.[18, 66-69] The key to opto-thermophoretic trapping is realization of a negative sign of D_{T} that drives colloidal particles from the cold to hot region. However, the system-specific thermophoretic drift of colloidal particles has not been fully understood, resulting in variable manipulation scenarios depending on various parameters such as temperature, ionic strength of solutions, surface chemistry of particles and solute concentrations.[9, 70]

Thermoelectricity is considered as a driving force for particle migration and opto-thermal manipulation.[14, 71-74] It is induced by thermal diffusion and spatial separation of dissolved ions in an ionic liquid under a temperature gradient field. Wurger *et al.* proposed a general opto-thermal system, in which surface "thermocharge" accumulation under a local temperature field leads to a thermoelectric field that can be used to concentrate or deplete colloidal particles at the thermal hot spot.[72] However, previous studies of

[3] Section 3.1 was published in the journal: **X. Peng**[*], L. Lin[*], E. H. Hill, P. Kunal, S. M. Humphrey, and Y. Zheng, Opto-thermophoretic Manipulation of Colloidal Particles in Nonionic Liquids, *J. Phys. Chem. C*, 2018, 122, 24226-24234. I am a leading author.

thermophoresis in the fluidic systems of low ionic strength and low acidity reveal the existence of non-ionic effects.[75, 76] Putnam *et al.* observed an intrinsic negative D_T for carboxyl particles in LiCl electrolyte at a low ionic strength, which arises from local excess enthalpy at the particle-solvent interface.[75] Piazza *et al.* observed a negative D_T for proteins at a low temperature, which is attributed to hydrophobic interactions at the protein-solvent interface.[76] We have recently reported the cold to hot migration of colloidal particles under light-generated temperature gradient field in water.[67, 77] However, the applicability of the opto-thermophoretic tweezers to different solvents has remained unknown.

Herein, we report opto-thermophoretic manipulation of colloidal particles in various non-ionic liquids, including water, ethanol, isopropyl alcohol (IPA), and 1-butanol, and establish the working principle of opto-thermophoretic tweezers at the molecular level. Our experiments and molecular dynamics (MD) simulations reveal that thermophoretic trapping is driven by the entropy at the particle-liquid interface, with a minor effect from the dispersion force. The trapping stability of particles can be improved by tuning the particle hydrophilicity, solvent type, and ionic strength that determine the layered structure of solvent molecules at the particle surface. We have further achieved opto-thermophoretic trapping, rotation, and translation of silver nanowires (AgNWs) at a low optical power. This work demonstrates the applicability of opto-thermophoretic tweezers to a broad range of colloidal systems.

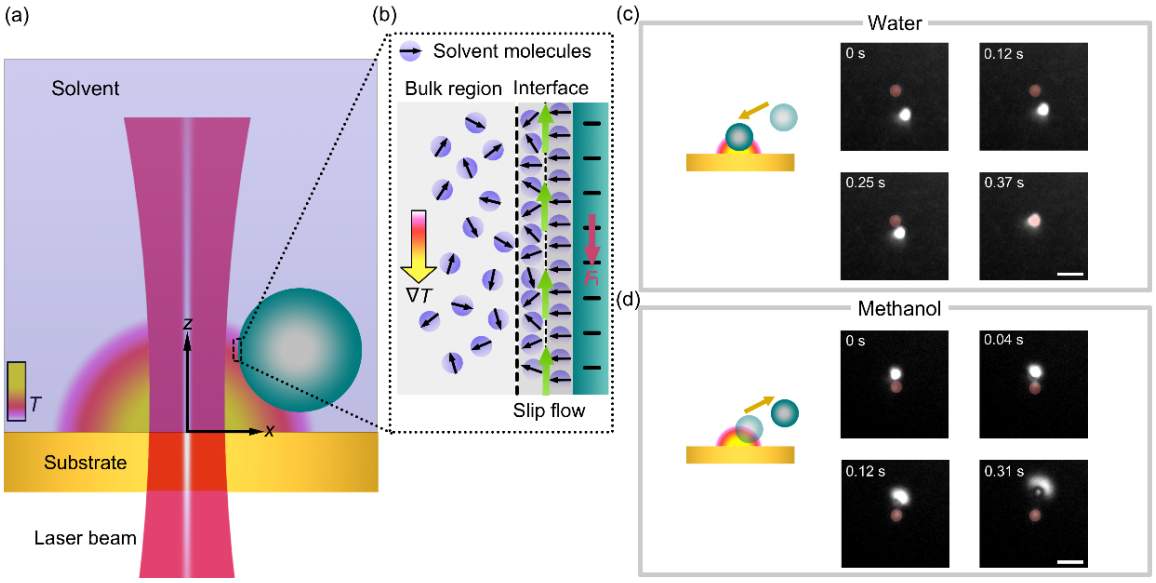

Figure 3.1: Working principle of opto-thermophoretic tweezers. (a) Schematic illustration of thermophoretic trapping of a colloidal particle at the hot region of an opto-thermal substrate upon irradiation by a laser beam. (b) Schematic illustration of a layered structure of solvent molecules at the particle-solvent interface. The interfacial-entropy-driven force F_i (red arrow) originates from an induced slip flow (green arrows) under a temperature gradient field ∇T, driving the particle from the cold to hot region for its trapping at the laser beam. (c) Schematics and optical images of trapping of a 1 μm polystyrene (PS) sphere in water due to the dominance of the interfacial entropy-driven force F_i. (d) Schematic and optical images of anti-trapping (*i.e.*, repulsion from the light-irradiated hot region) of a 1 μm PS sphere in methanol due to the dominance of the dispersion force F_d. A laser beam with a diameter of 2 μm and a power intensity of 0.16 mW/μm^2 was irradiated onto the opto-thermal substrate (indicated by the red circles in the optical images of c & d). A 20 μm thick chamber that contains the colloidal solution was stacked on top of the substrate. Scale bars in the optical images of (c-d) are 5 μm.

The working principle of opto-thermophoretic tweezers is illustrated in Figs. 3.1a-b. A laser beam is focused onto an opto-thermal substrate to create a temperature gradient field at the substrate-solvent interface. Colloidal particles with surface charges are suspended in non-ionic polar solvents. Under the temperature gradient field, a colloidal particle migrates from the cold to hot region and gets trapped at the laser beam center with

the balance of the entropy-driven force F_{i}, the optical gradient force, the optical scattering force and particle-substrate interaction.

Migration of the particle due to the entropy-driven force F_{i} can be described by Anderson's model where the thermophoretic drift velocity $\boldsymbol{u}$ is expressed as[75, 78]

$$\boldsymbol{u} = -D_{\mathrm{T}}\nabla T = \frac{2}{\eta T}\frac{2\kappa}{2\kappa + \kappa_{\mathrm{P}}}\int_0^{\infty} zh(z)dz\nabla T \tag{3}$$

where D_{T} is the thermophoretic mobility, ∇T is the temperature gradient, η is the viscosity of the solvent, T is the temperature, κ and κ_P are the thermal conductivities of the solvent and the particle respectively, and $\int_0^{\infty} zh(z)dz$ is the slip-velocity coefficient with $h(z)$ as the local excess enthalpy density at a distance z from the particle surface (compared with that at an infinite distance). If the local excess enthalpy density is mainly caused by polarization of solvent molecules under the interfacial electrical field, $h(z)$ can be evaluated as $\frac{1}{2}\varepsilon(z)(1 + \frac{\partial \ln \varepsilon(z)}{\partial \ln T})E^2(z)$, where ε is the dielectric constant of the solvent as a function of z and $E(z)$ is the local electrical field.[75] We approximate $E(z)$ as $\frac{\xi}{\lambda}e^{-\frac{z}{\lambda}}$, $\varepsilon(z)$ as ε_b, and $\frac{\partial \ln \varepsilon(z)}{\partial \ln T}$ at the particle-solvent interface as an effective value τ, where ζ is the surface potential of the particle, λ is the effective decay length of the local electrical field and ε_{b} is the dielectric constant of the solvent in the bulk region. Therefore, the thermophoretic drift velocity $\boldsymbol{u}$ is given by

$$\boldsymbol{u} = \frac{\varepsilon_b}{2\eta T}\frac{2\kappa}{2\kappa + \kappa_P}(1 + \tau)\zeta^2\nabla T \tag{4}$$

We can see that one of the parameters that determine the particle migration direction is τ, which is related to the structures of the solvent molecule at the particle-solvent interface.[79-82] As described in the BDM model proposed by Bockris, Devanathan, and Muller,[79] solvent molecules adsorb onto the charged surface of a colloidal particle to form layered structures at the particle-solvent interface. As shown in Fig. 3.1b, the molecules in the first layer have their orientation aligned with the electric field from the

surface charges, while those in the second layer are partially oriented toward the particle surface. The molecules in the third layer and beyond (*i.e.*, bulk region) become disordered.

Under an externally applied temperature gradient, the orientation of the interfacial molecular dipoles at the hot side of the particle becomes disordered due to the increased entropy, leading to a higher permittivity and thus a higher electric energy density. Interestingly, the increased permittivity at the higher temperature leads to a positive τ in Equation (4), rendering the thermophoretic motion of the particle from the cold to the hot region to achieve opto-thermophoretic trapping. As illustrated in Fig. 3.1b, the permittivity gradient induces a slip flow,[9] which leads to the interfacial-entropy-driven force F_i (red arrow) and drags the particle to the hot region.

There is also a dispersion force F_d, which arises from the density gradient of the solvent under the temperature gradient.[9] In contrast to the interfacial-entropy-driven force, the dispersion force drives particles from the hot to cold region. Common solvents expand upon heating with one exception (*i.e.*, water below 5 ℃). The colder solvent with a higher density experiences a stronger van der Waals attraction from the particle, leading to a slip flow that drives the particle toward the cold region. According to Wurger's hydrodynamic model,[9] the thermophoretic drift velocity due to the dispersion force is written as

$$\boldsymbol{u} = -\frac{2\beta H}{9\pi\eta d_0}\nabla T \tag{5}$$

where β is the thermal expansivity of the solvent, H is the Hamaker constant of the particle-solvent interactions, d_0 is a molecular length scale, and η is the viscosity of the solvent.

For a charged colloidal particle under a temperature gradient ∇T, the thermophoretic migration can also be contributed by temperature gradient-induced distortion of the Debye layer.[83] A temperature gradient will deform the Debye layer,

leading to an electric force acting on the surface charges of the colloidal particle and a solvent-friction force on the surface of the colloidal particle. The two forces are typically a factor $\frac{\varepsilon_0}{\varepsilon_b}$ smaller than that caused by the temperature dependence of the internal electrostatic energy at the interface (Equation (4)). We thus exclude their contributions on the thermophoretic migration as the polar solvents in our experiments have relatively large dielectric constant ε_b (spans from $20\varepsilon_0$ to $80\varepsilon_0$). Thermo-osmotic flow also coexists with the thermophoretic migration once a temperature gradient is created at the substrate-solvent interface. Thermo-osmotic flow that is parallel to the substrate surface has a negative effect in trapping, which is significant for a very thin Debye layer compared to the particle size.[9, 84] We neglect the thermo-osmosis effect for a low ionic strength of the polar solvents and a large Debye screening length (in the order of μm) of the charged substrate surface.

As an example, we use polystyrene (PS) spheres in water to compare the contributions of the dispersion force and the interfacial-entropy-induced force on the thermophoresis of the colloidal particles. Since the ionic sulfate groups grafted on the surface of PS spheres make a rough interface, the van der Waals interactions between the particle and water is weak and the molecular length scale d_0 should be estimated based on the size of the ionic sulfate groups rather than the size of the solvent molecules. With d_0 ~ 1 nm, $H \sim 2 \times 10^{-20}$ J, $\beta \sim 2.56 \times 10^{-4}$ K^{-1} and η ~1.08 × 10^{-3} cP at 25 ℃, D_T induced by the dispersion force is 0.35 μm^2 K^{-1} s^{-1}. With $\zeta \sim$ 50 mV and τ ~2,[85] D_T induced by the interfacial-entropy-induced force gives a value of -3 μm^2 K^{-1} s^{-1}, which is 1 order of magnitude higher than that caused by the dispersion force. The opposite signs of D_T indicate that the dispersion force drives the particle from the hot to the cold region whereas the interfacial-entropy-induced force drives the particle from the cold to the hot region. It should be noted that the dispersion force can dominate over the entropy-driven

force for colloidal particles in solvents with a high thermal expansivity β and a low viscosity η (*e.g.*, methanol).

To experimentally explore the roles of the entropy-induced force and dispersion force in opto-thermophoretic manipulation of colloidal particles, we studied kinetics of 1 μm PS particles under a light-generated temperature gradient field in water and methanol, respectively. We carried out real-time tracking of the particles with a fast CCD camera, as shown in Figs. 3.1c-d. A laser beam with a diameter of 2 μm and a power intensity of 0.16 mW/μm^2 was focused onto the optothermal substrate to create a localized temperature gradient field. The particle suspensions were contained in a 20 μm thin chamber above the substrate to reduce thermal convection.[10] Upon irradiation of the laser beam, a particle in water was rapidly delivered toward and trapped at the beam center (Fig. 3.1c). In contrast, a particle in methanol was repelled away from the beam center and the substrate upon the irradiation of the laser beam (Fig. 3.1d). It should be noted that particle migration was driven by the temperature gradient field rather than the optical gradient force. Our weakly focused laser beam, which has a diameter of 2 μm, generates a small optical gradient force compared to the opto-thermophoretic force.

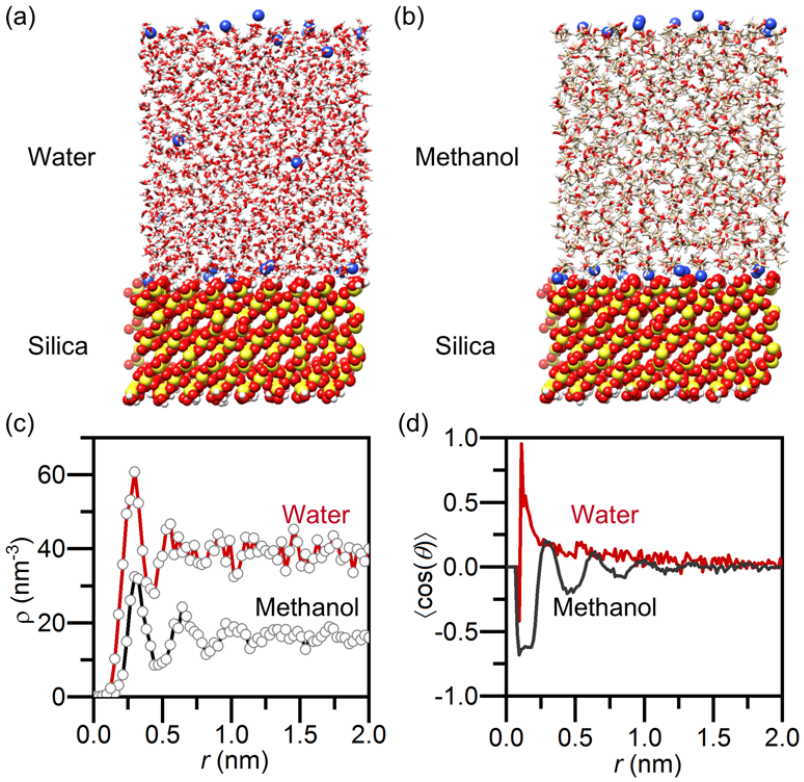

Figure 3.2: Molecular dynamics simulation of silica-water and silica-methanol interfaces. Snapshots of the simulation box with (a) water and (b) methanol in contact with a silica surface at pH 7.5. (c) Number density profiles of water molecules (red) and methanol molecules (black) at the interface. (d) Orientational polarization profiles (relative to axis perpendicular to the silica surface) of water molecules (red) and methanol molecules (black) at the interface. In (c-d), the origin of the *r*-axis is set to the silica surface.

We further measured the drift velocities of the particles under the temperature gradient field in water and methanol. For 1 μm PS particles, we obtained an absolute value of ~ 10 μm s^{-1} in both solvents. Considering an average in-plane temperature gradient of 4 K μm^{-1}, we calculated the drift velocity of 12 μm s^{-1} in water (Equation 4), which is close to the experimental value. Wurger's hydrodynamic model gives a drift velocity of -12 μm s^{-1} in methanol, which indicates that the dispersion force drove the anti-trapping of the particle due to the weak entropy-induced force. We also measured the drift velocities of 2

μm PS particles in water and methanol. The drift velocity for 2 μm PS particles in methanol is slightly smaller than that of 1 μm PS particles in methanol. The smaller velocity is attributed to the weaker average temperature gradient field and negligible hydrodynamic boundary effect due to repulsion of the particle away from the substrate.[77, 86]

To identify the mechanisms and driving forces of colloidal thermophoresis, molecular dynamics simulations have been applied to study thermophoretic migration behaviors for a small number of systems.[87, 88] To validate the mechanism behind the entropy-driven force in opto-thermophoretic tweezers at the molecular level, we carried out molecular dynamics (MD) simulations to investigate the structure of solvent molecules at the particle-solvent interface. As similar trapping and anti-trapping of silica spheres under a temperature gradient field in water and methanol was observed with the case of PS spheres, we used a well-established model of the silica surface to simulate the interfacial solvent structure. Snapshots of the simulation boxes after 80 ns *NVT* simulation are shown in Figs. 3.2a-b, together with the number density profiles (Fig. 3.2c) and orientational polarization profiles (Fig. 3.2d). As shown in Fig. 3.2c, the number density for both water and methanol molecules exhibits an oscillatory behavior, suggesting the formation of layered structures of solvent molecules, *i.e.*, layers (peaks) and sublayers (dips), at the silica-solvent interfaces.[89, 90] The slight out-of-phase of the two curves is due to the different molecular sizes between water and methanol. The number density becomes relatively uniform as it approaches the bulk phase with increased distance from the silica surface.

The orientational polarization profile $< \cos(\theta) >$, which represents the degree of ordering in the solvent layers, was obtained by calculating the normalized cosine of the angle between the molecular dipoles and the normal of the silica surface, as plotted in Fig. 3.2d. In water, the orientation of dipoles decays exponentially as distance from the interface

increases, with the dipole orientation becoming random in the bulk region. This justifies our permittivity gradient model in evaluating the thermophoretic mobility D_T in Equation (4). Beyond the electrostatic charge-dipole interactions, hydrogen bonding at the interface also plays a critical role in the structuring of the solvent molecules, which is termed as a "solvation layer".[81, 91] In methanol, the polarization profile exhibits damped oscillations, which is due to the formation of an antiparallel bilayer structure.[90] Within the layered solvent structure, the first layer of well-oriented methanol molecules (r ~ 0.25 nm) interacts with the silica surface *via* hydrogen-bonding and presents a hydrophobic surface, inducing an opposite polarization in the second layer (r ~ 0.5 nm). This layered structure accounts for the weak entropy-driven force in methanol because the cancellation effect of the antiparallel layers leads to a significantly diminished slip flow at the particle-methanol interface. Although surface defects need to be considered for realistic surfaces of silica spheres, the surface defects will not affect the formation of layered structures but increase the population and dynamics of the molecules at the interface, in other words, it will amplify the interfacial effect for thermophoretic trapping.[90]

According to our established working mechanism, the entropy-driven force must dominate over the dispersion force to enable opto-thermophoretic trapping of colloidal particles. We can choose suitable polar solvents to meet this requirement. For ethanol, IPA and 1-butanol where d_0 ~ 2 nm and $H \sim 1 \times 10^{-20}$ J, D_T contributed by the dispersion force is ~ 0.55, ~ 0.26 and ~ 0.11 $\mu m^2\ K^{-1}\ s^{-1}$, respectively, which is smaller than the contribution from the entropy-driven force (in the order of $\mu m^2\ K^{-1}\ s^{-1}$). Thus, we expect that opto-thermophoretic trapping of particles can be achieved in these solvents, which has been verified experimentally. As examples, we demonstrated opto-thermophoreic trapping of 500 nm PS spheres in water, ethanol, IPA, and 1-butanol. Moreover, the trapping stability in these solvents was studied by tracking the position fluctuations of the particles

under the temperature gradient field. The histograms of the particle displacement are presented in Figs. 3.3a-d (x direction). Gaussian fitting was used to measure the variance σ of the Brownian motion and to extract the trapping stiffness $\kappa = \frac{2k_B T}{\sigma^2}$.[92] The trapping stiffness in water has the largest value of 7.5 ± 5.0 pN/μm. The particle trapping in 1-butanol is not stable where the position fluctuation reaches a non-harmonic region that is outside the laser beam. Since the trapping stiffness $\kappa \propto D_T$,[11] the trapping stability is influenced by the term $\frac{\varepsilon_b}{\eta T}\frac{2\kappa}{2\kappa+\kappa_P}$ in Equation (4), the values of which are summarized in Table 1. 1-butanol leads to a trapping stiffness 1 order of magnitude smaller than water due to its small dielectric constant and large viscosity. The ratio of the trapping stiffness in ethanol to that in water is less than the value predicted by Equation (4) (Table 1), which can be attributed to the smaller τ [90] and the larger dispersion force in ethanol. The trapping stiffness in IPA is comparable to that in ethanol where strong particle-solvent interactions with extended interfacial structures occur.[93] The consistency between the experiments and the models of the particle-trapping in the various solvents further validates the mechanism of the entropy-driven force in opto-thermophoretic tweezers.

Solvents	ε_b	η (cP)	κ (W m^{-1} K^{-1})	$\frac{\varepsilon_b}{\eta T}\frac{2\kappa}{2\kappa+\kappa_P}$ (cP^{-1}.K^{-1})
Water	78.5	1.082	0.606	0.118
Methanol	31.5	0.545	0.198	0.090
Ethanol	24.3	0.890	0.159	0.042
IPA	18.0	1.960	0.136	0.014
1-butanol	17.3	2.544	0.155	0.011

Table 3.1: Parameters for calculation of D_T in different solvents at 25 ℃ (κ_P is 0.03 W m^{-1} K^{-1}).

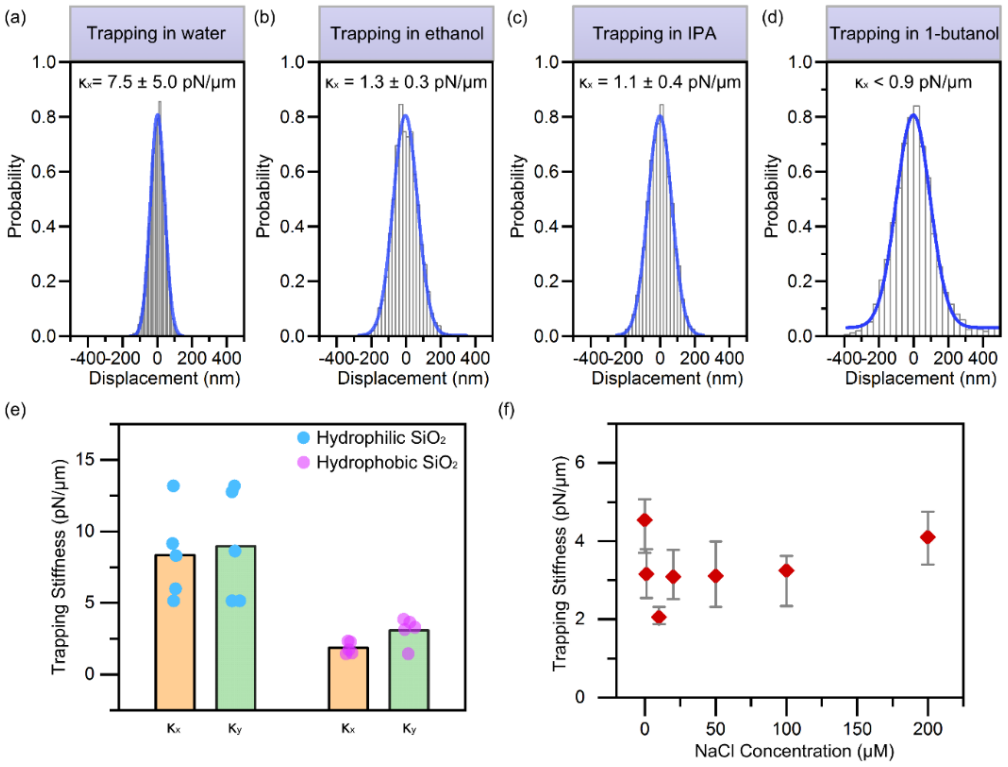

Figure 3.3: Effects of solvent, particle hydrophilicity, and ion concentration on opto-thermophoretic trapping of colloidal particles. (a-d) Measured histograms of particle displacement and the corresponding trapping stiffness (x direction) for 500 nm PS spheres in water, ethanol, IPA and 1-butanol. (e) Measured trapping stiffness for 1 μm hydrophilic and hydrophobic silica (*i.e.*, SiO_2) particles in water. The dots indicate the values of different particles. The columns indicate the average values. (f) Measured trapping stiffness for 1 μm PS spheres in IPA as a function of NaCl concentration. A focused laser beam with a diameter of ~520 nm and an optical power of ~0.5 mW was illuminated onto the optothermal substrate with a thin chamber of (a-d, f) 20 μm in depth and (e) 120 μm in depth. Standard deviations (a-d) and error bars (f) of the trapping stiffness were obtained by tracking 5 to 6 different particles.

We have further demonstrated fine tuning of opto-thermophoretic trapping of colloidal particles by controlling surface chemistry of the particles or ionic strength of the solvents. Both surface chemistry and ionic strength can modify the interfacial molecule layers and thus the entropy-driven force. Fig. 3.3e shows the trapping stiffness of 1 μm

hydrophilic and hydrophobic silica (SiO_2) particles in water. To increase the hydrophobicity, the as-purchased hydrophilic silica particles were coated with (pentaflurotrimethyl)triethoxysilane, which reduced the concentration of silanol groups on the particle surfaces and extended the hydrophobic areas. The surface charge was not changed by the coating, as shown by zeta-potential measurements (Fig. 3.4). A lower trapping stability was observed for the hydrophobic particles. This is because the poor adsorption of water molecules on the hydrophobic surfaces weakened the layered structure and thus reduced the entropy-driven force.[89] It should be noted that the optical gradient force is much weaker than the entropy-driven force, which is verified by the release of a trapped hydrophilic silica particle when translating it from the optothermal substrate to the glass substrate. We used 120 μm chambers to avoid spontaneous adhesion of silica particles to the substrate. Alhough a stronger convection at thicker chambers may lower the trapping stability,[77] hydrophilic particles will maintain a higher trapping stiffness than that of hydrophobic ones for a stronger entropy-driven force. Fig. 3.5 shows the measured trapping stiffness of 500 nm PS spheres in water as a function of NaCl concentration. The trapping stiffness decreased when the NaCl concentration was increased, and trapping could not be achieved any more once the NaCl concentration was increased to 400 μM. We believe that the increased ionic strength, and thus the ion-molecule interactions, destabilized the layered structure at the particle-solvent interface.[67] In addition, a thermoelectric effect that led to $D_T \sim 2\ \mu m^2\ K^{-1}\ s^{-1}$ occurred,[9, 15] setting an upper limit of ionic concentration for opto-thermophoretic tweezers. However, as the saturated NaCl concentration in IPA is much lower than that in water, trapping stability is maintained across the entire NaCl concentration range in IPA, as shown in Fig. 3.3f.

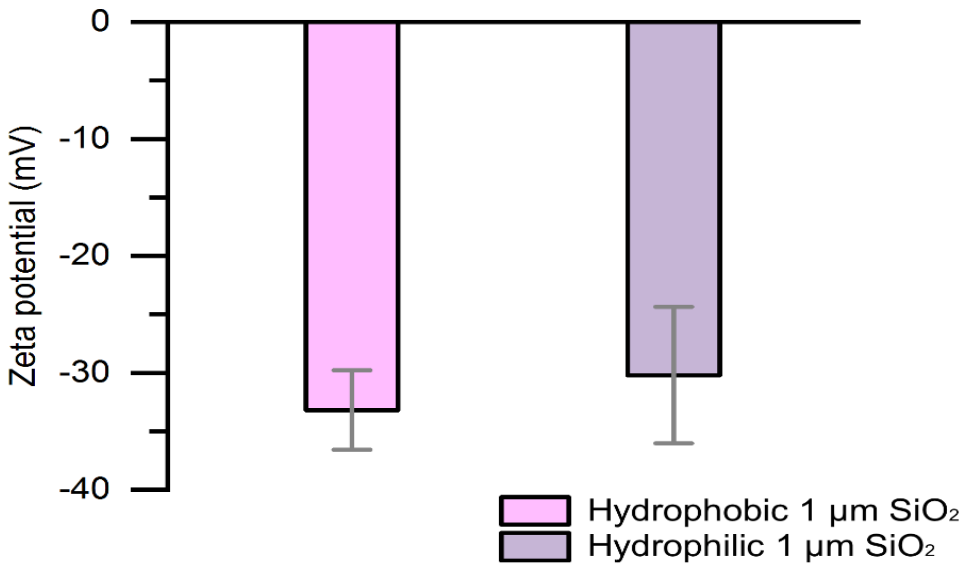

Figure 3.4: Zeta potentials of 1 μm hydrophobic and hydrophilic silica (SiO_2) particles in water.

Lastly, we demonstrated opto-thermophoretic manipulation of Ag nanowires (AgNWs). The AgNWs have a length in the range of 2-12 μm and a width in the range of 50-300 nm. Optical manipulation of metal nanostructures is challenging due to enhanced optical absorption and scattering, which dramatically increases the optical radiation force. We dispersed the AgNWs in IPA where the entropy-driven force could overcome the optical scattering force to achieve opto-thermophoretic trapping of the AgNWs. We further achieved the opto-thermophoretic transport and rotation of AgNWs at a low optical power using a one-dimensional optothermal potential, as shown in Figs. 3.6a-b. The controlled rotation of a single AgNW above the other AgNW immobilized on the substrate was also demonstrated (Figs. 3.6c-d), showing the potential of opto-thermophoretic tweezers for assembly of nanowires into functional components and devices.

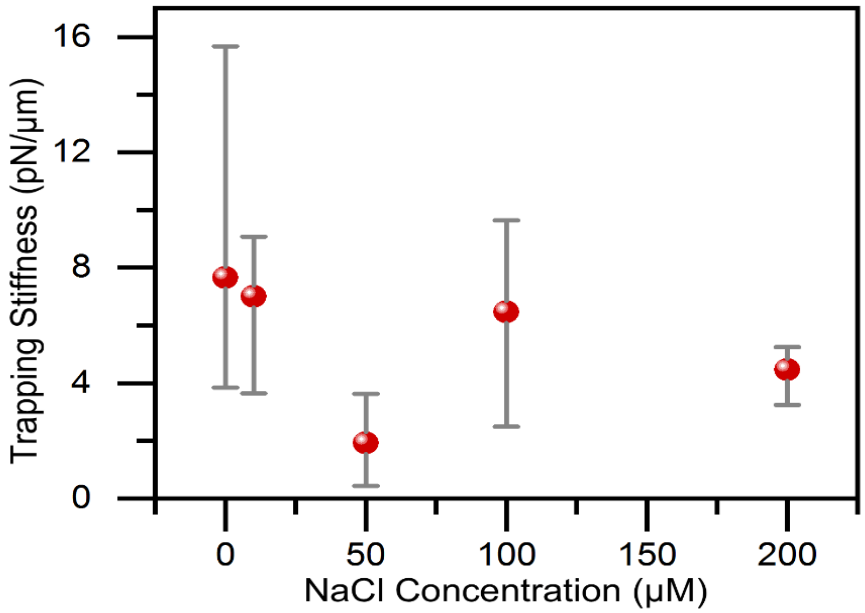

Figure 3.5: Measured trapping stiffness for 500 nm PS spheres in water as a function of NaCl concentration.

We have established the working mechanism of opto-thermophoretic tweezers for colloidal particles in non-ionic liquids at the molecular level. Specifically, opto-thermophoretic trapping is driven by the entropy at the particle-liquid interface with a minor effect from the dispersion force. The entropy-driven force arises from the structured solvent layers at the particle-solvent interfaces, which is supported by all-atom MD simulations. Parameters such as particle hydrophilicity, particle surface charge, solvent type, and ionic strength can be adjusted to control the interfacial structure of the solvent molecules in order to improve the trapping stability of colloidal particles. With their low-power operation and simple optics, opto-thermophoretic tweezers will find applications in colloidal science, materials science, cell biology, and nanofabrication.

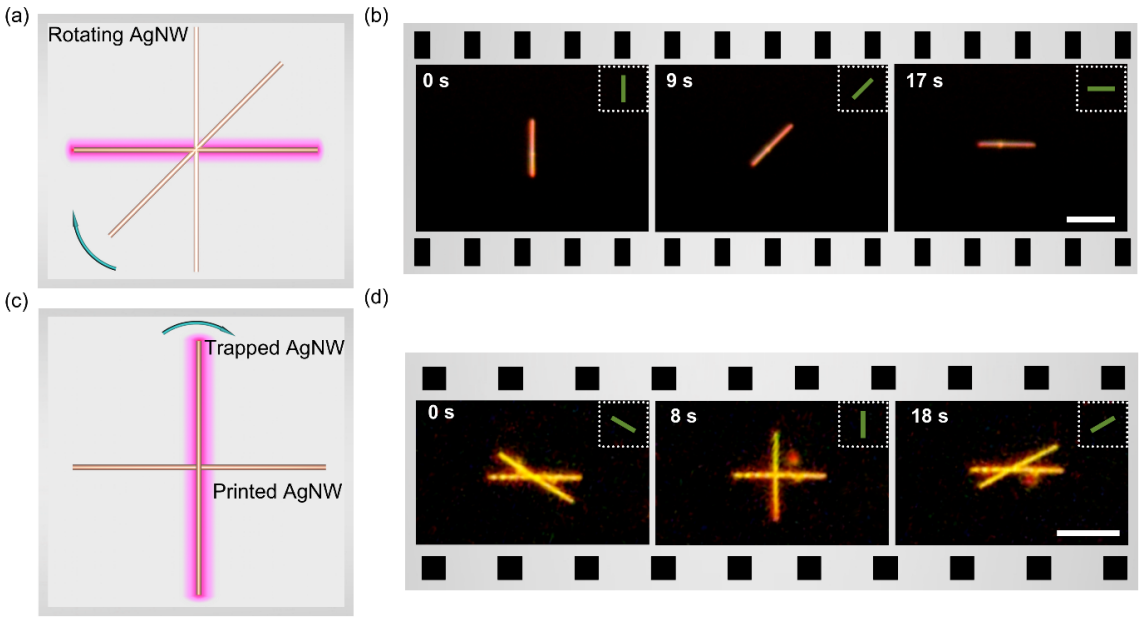

Figure 3.6: Opto-thermophoretic manipulation of AgNWs in IPA. (a) Schematic illustration and (b) time-resolved dark-field optical images of rotation of a AgNW with one-dimensional optothermal potential. (c) Schematic illustration and (d) time-resolved dark-field optical images of rotation of a AgNW over another AgNW printed on the substrate. Insets in (b) and (d) show the orientations of the 10 × 1 μm^2 line-shaped laser beam with an optical power of 0.67 mW. Scale bars: (b) 10 μm and (d) 5 μm.

3.2 Opto-Thermophoretic Manipulation of Biological Cells in Water[4]

The manipulation of biological cells and nanoparticles has important applications in life sciences and nanoscience such as cell manipulation,[94, 95] early disease diagnosis,[96, 97] immunological interaction,[98, 99] and colloidal nanotechnology.[100-102] Scientific and technological advances have led to quite a few types of light-based tweezers such as optical tweezers,[1, 39, 103, 104] optoplasmonic tweezers,[5, 105-107] optoelectronic tweezers,[7] optoacoustic tweezers,[108] and electrothermoplasmonic tweezers,[109] which exploit direct or indirect

[4] Section 3.2 was published in the journal: L. Lin*, **X. Peng***, X. Wei, Z. Mao, C. Xie, and Y. Zheng, Thermophoretic Tweezers for Low-Power and Versatile Manipulation of Biological Cells, *ACS Nano*, 2017, 11, 3147-3154. I am a leading author.

optical force and energy for particle or cell manipulation. Despite tremendous successes in the light-based tweezers, the low-power, versatile, and all-optical manipulation of general nanoparticles and cells remains elusive. Optical tweezers offer high-resolution trapping of single particles in three-dimensional (3D) configuration. However, the use of optical tweezers is limited by the requirements of a tightly focused high-power laser beam and the prominent refractive index contrast between the trapped objects and the liquid media. Because optoelectronic tweezers use projected light patterns to form virtual electrodes on a photosensitive substrate and conductive electrolytes as liquid media, they require both electric bias and low optical power for arbitrary manipulation of particles and cells.[7] With the capability of concentrating light into the nanoscale, metallic nanostructures have been exploited in plasmonic tweezers to enhance the optical trapping.[5, 105-107, 110] Despite their low-power trapping of nanoparticles, plasmonic tweezers have limitations in long-range transport and arbitrary manipulation of the target objects.[6, 109] Recently developed electrothermoplasmonic tweezers can transport nanoparticles over a long distance and trap them at the plasmonic structures.[109]

Thermophoresis has been proven as an effective strategy to transport suspended particles in the fluids.[11, 14, 15, 111] With its capability of selectively driving suspended objects into warm or cold regions along a temperature gradient, thermophoresis provides a noninvasive approach toward trapping and concentrating biomolecules.[9, 16, 17, 112, 113] Confinement of single nanoparticles and macromolecules has been demonstrated by driving the particle and molecule *via* a dynamic temperature field.[62, 63, 114] However, the use of thermophoresis in trapping and manipulating individual biological cells in an arbitrary manner has not been achieved. Herein, through exploitation of the interactions between the cell membrane and the water molecules in the electric double layer, we have experimentally demonstrated harnessing of light-induced thermophoresis for versatile

manipulation of yeast cells and *Escherichia coli* cells using low-power light and the associated temperature gradient. Our cell manipulation enables diverse functionalities for applications in cellular biology and biomedicine, including precise intercellular distance control for the study of cell-cell interactions, targeted cell delivery, cell assembly, and orientation control at the single-cell level.

To demonstrate thermophoretic tweezing of biological cells, we use a solid-state substrate that consists of Au nanoparticles (AuNPs) on a glass slide, a chamber that contains suspensions of particles or biological cells in water, and an optical imaging and control system based on a digital micromirror device **(**DMD) (Fig. 3.7a). A single laser beam is directed onto a computer-controlled DMD and the optical images reflected off the DMD are focused on the substrate to define the optical landscape. We optimize the size of the AuNPs to match the surface plasmon resonance wavelength with the incident laser wavelength (Fig. 3.7b) to improve the absorption efficiency. The absorbed optical power is described by $Q = N\sigma_{\mathrm{abs}}I$, where σ_{abs} is the absorption cross section of the AuNPs, N is the number of particles under illumination and I is the irradiance of the incident laser. The absorbed optical power is converted to heat according to the Joule effect. A steady-state temperature profile is attained when the heat diffusion between the AuNPs and the surrounding environment achieves balance. By experimentally measuring the absorbed optical power of the AuNPs, we simulated the temperature distribution around the laser beam, as shown in Fig. 3.7c. The maximum temperature gradients of $\nabla T_{\mathrm{z}} = -8.49 \times 10^{6}\ K/m$ and $\nabla T_{\mathrm{r}} = -3.58 \times 10^{6}\ K/m$ were created under a low-power light irradiation. The DMD-defined optical landscape on the substrate controls the optothermal potential at the substrate-liquid interface for the cell trapping.

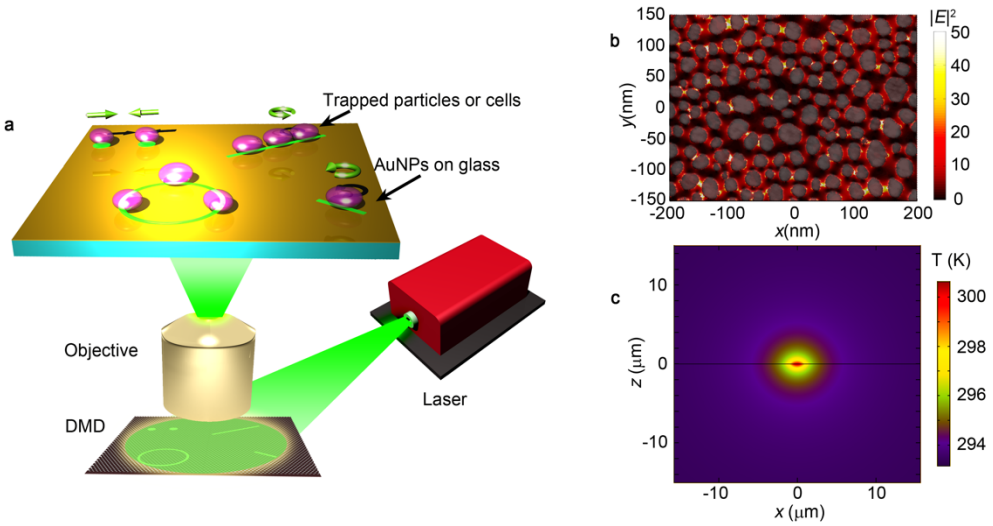

Figure 3.7: Experimental setup of thermophoretic tweezers. (a) Optical setup of thermophoretic tweezers. An incident laser is directed to a DMD and the resultant optical images are focused on a AuNP substrate for excitation of surface plasmons. The plasmon-enhanced optothermal potentials defined by the DMD-controlled optical images are employed to trap and arbitrarily manipulate colloidal particles or biological cells. (b) Scanning electron micrograph of the AuNP substrate overlaid with simulated electric field to show a network of high-density electromagnetic "hot spots". (c) Cross-sectional view of simulated temperature distribution at the substrate-liquid interface. The horizontal line at z=0 indicates the substrate-liquid interface.

To achieve the themophoretic trapping of biological cells, we explore the interfacial interaction between the cell membrane and the water molecules, as shown in Fig. 3.8. Most of the biological cells have negative surface charge due to the phospholipid bilayers in the cell membrane, which is schematically illuminated in Fig. 3.8a. The phospholipid is composed of a negatively charged hydrophilic headgroup, with the charge contributed by the phosphate group, and two hydrophobic fatty acid tails. The hydrophobic interaction between the tails creates a bilayer structure, with the charged headgroup in contact with the water molecules at extracellular side. The surface charges induce an electric field **E** pointing to the cell membrane surface. The water molecules can be treated as electric dipoles and they adsorb on the cell membrane to form an orientated layer with a fixed

alignment to the membrane surface under the electric field **E**, as shown in Fig. 3.8b. The water dipoles on the second layer have a loosely orientated structure.

It has been known that the permittivity of water is highly dependent on the dipolar orientation, and the permittivity in the electric double layer (ε_{ed}) is significantly lower than that in bulk water (ε_{bulk}), according to BMD model.[79] When a temperature gradient field ∇T is applied, the permittivity in bulk water and the electric double layer will be modified in opposite signs along the temperature gradient. The permittivity in the electric double layer will be increased due to thermal perturbations, or increased entropy, resulting in a positive value of $\partial\varepsilon/\partial T$ (Fig. 3.8c). The entropy change is approximated as $H(z) = \frac{1}{2}\left(\varepsilon + \frac{T\partial\varepsilon}{\partial T}\right)E^2(z)$. The electric field E is a function of the Debye length κ^{-1} and the surface potential of the cell ζ: $E(z) = \kappa\zeta\exp(-\kappa z)$, where z is the distance from the membrane surface. Therefore, the thermophoretic mobility can be calculated by:[12, 78]

$$D_T = -\frac{2}{\eta T}\frac{2\Lambda_1}{\Lambda_1 + \Lambda_P}\int_0^\infty zH(z)dz == -\frac{2}{\eta T}\frac{2\Lambda_1}{\Lambda_1 + \Lambda_P}\left(\varepsilon + \frac{T\partial\varepsilon}{\partial T}\right)\zeta^2 \qquad (6)$$

where η is the solvent viscosity, while Λ_1 and Λ_p are the thermal conductivity of the solvent and the cell, respectively. Therefore, the cell will migrate to the hot region with a velocity $v_p = -D_T\nabla T$, leading to the trapping of the cell at the laser spot (Fig. 3.8d).

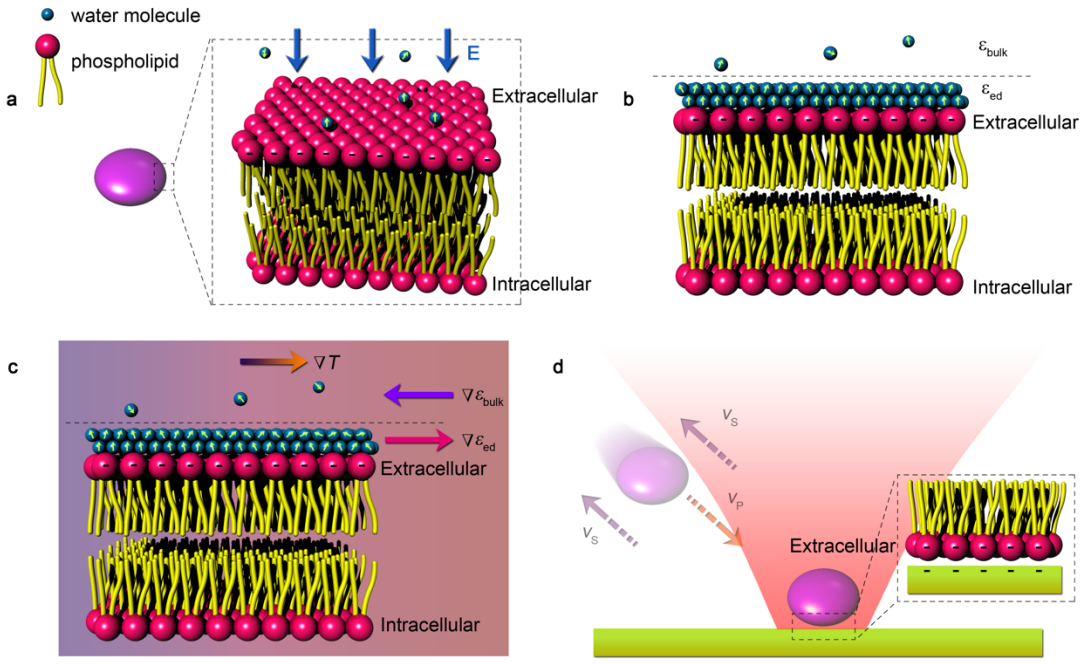

Figure 3.8: Working principle of cell trapping with the thermophoretic tweezers. (a) Simplified structure of the lipid bilayer in the membrane of a biological cell. The phosphate groups in the phospholipid provide the negative charges on the cell membrane and induce an electric field **E** to drive the water molecules toward the membrane. (b) Orientated water molecules form in the electric double layer of the cell membrane under the electric field. The permittivity of the water in the electric double layer (ε_{ed}) strongly depends on the orientation of the molecules, which is different from that of the bulk water (ε_{bulk}). (c) Thermal response of the permittivity in the electric double layer (*i.e.*, permittivity gradient $\nabla\varepsilon_{ed}$) on the cell membrane under a temperature gradient field ∇T, which induces the thermal perturbation and increases the entropy of the water molecules. The sign of $\nabla\varepsilon_{ed}$ is opposite to that of $\nabla\varepsilon_{bulk}$. (d) The permittivity gradient $\nabla\varepsilon_{ed}$ generates a slip velocity v_s pointing from hot to cold and the cell migrates in an opposite direction with a velocity v_p, which leads to the trapping of the cell at the hot laser spot. The electric static repulsive force between the cell membrane and the substrate, both of which have negative charges, balances the trapping force.

The use of a solid-state substrate induces the hydrodynamic boundary effect, which can dramatically increase the Soret coefficient when the cell-substrate distance is much smaller than the radius of the cell, with an enhancement factor of[86]

$$\phi(\hat{h}) = 3(1+\hat{h})\frac{(2+6\hat{h}+3\hat{h}^2)\ln\left(\frac{\hat{h}+1}{\hat{h}}\right)-\frac{3}{2}(3+2\hat{h})}{2+9\hat{h}+6\hat{h}^2-6\hat{h}(1+\hat{h})^2\ln\left(\frac{\hat{h}+1}{\hat{h}}\right)} \quad (7)$$

where $\hat{h}=h/R$ and h is the cell-substrate distance. An enhancement factor of ~8 is obtained when $\hat{h}=0.01$. The hydrodynamic boundary effect leads to a large thermophoretic force even at a moderate temperature gradient.

It should be noted that optical heating of the substrate could also induce thermal convection of the fluid. To exclude thermal convection as the driving force in our thermophoretic tweezers, we simulated the convective flow distribution at a laser spot with the same optical power used for cell trapping (Fig. 3.9a). The in-plane velocity of the convective flow above the substrate is lower than 150 nm/s. To evaluate whether this convective flow can lead to stable trapping, we measured the Brownian motion of polystyrene (PS) beads with different sizes as a function of environmental temperature (Fig. 3.9b). We can clearly see that the convective flow cannot overcome the Brownian motion at the low-power light illumination used in our trapping experiments. The minor role of convective flow in trapping is further verified by placing a PS bead 20 μm away from the laser spot, where the temperature gradient is weak and thermophoresis can be ignored. Without the thermophoresis, the convective flow alone cannot deliver the particle to the laser spot, as shown in Fig. 3.9c. At a higher optical power of 0.4 mW, A 2 μm PS can be delivered to the laser spot at a low velocity of ~400 nm/s, indicating a convective drag force of 6.7 fN on the particle. The small drag force is insufficient for particle trapping. In addition, we reduced the chamber thickness to suppress the thermal convective flow. As shown in Fig. 3.9d, the convective flow distribution in the chamber of 20 μm in thickness were simulated. The maximum convective flow velocities are 2 orders of magnitude lower

than the values shown in the 1 mm chamber. We have conducted trapping experiments in the ultrathin chambers and can still achieve the trapping. Surprisingly, we observed an enhanced trapping stability in the thin chamber. Fig. 3.9e shows the escape velocities of trapped 0.96 μm PS beads measured in both 20 μm and 1 mm chambers. The escape velocity in the thin chamber is more than 5 times larger than that in the thick one, revealing that the suppression of thermal convection reduces the gap between the trapped particle and the substrate and thus leads to a stronger hydrodynamic boundary effect in the thermophoretic tweezers. Our observation of increased migration velocity of the particle when it approaches the heating laser and similar trapping behavior of the PS beads in the mixture of H_2O and D_2O further verify that the thermal convection is not the driving force of the trapping. Although convection effect is weak in our thermophoretic trapping, if needed, the convection flow velocity can be significantly improved by increasing the optical power to deliver the faraway objects toward the trapping sites.

We further exclude plasmon-enhanced optical force in our thermophoretic tweezers. Our calculation of optical force based on the Maxwell stress tensor method gives an optical gradient force of only 4 fN for a 500 nm PS bead. However, the measured escape velocity of the 500 nm PS beads at the same optical power gives a trapping force of 170 fN, revealing the ignorable contribution of optical force in our tweezers.

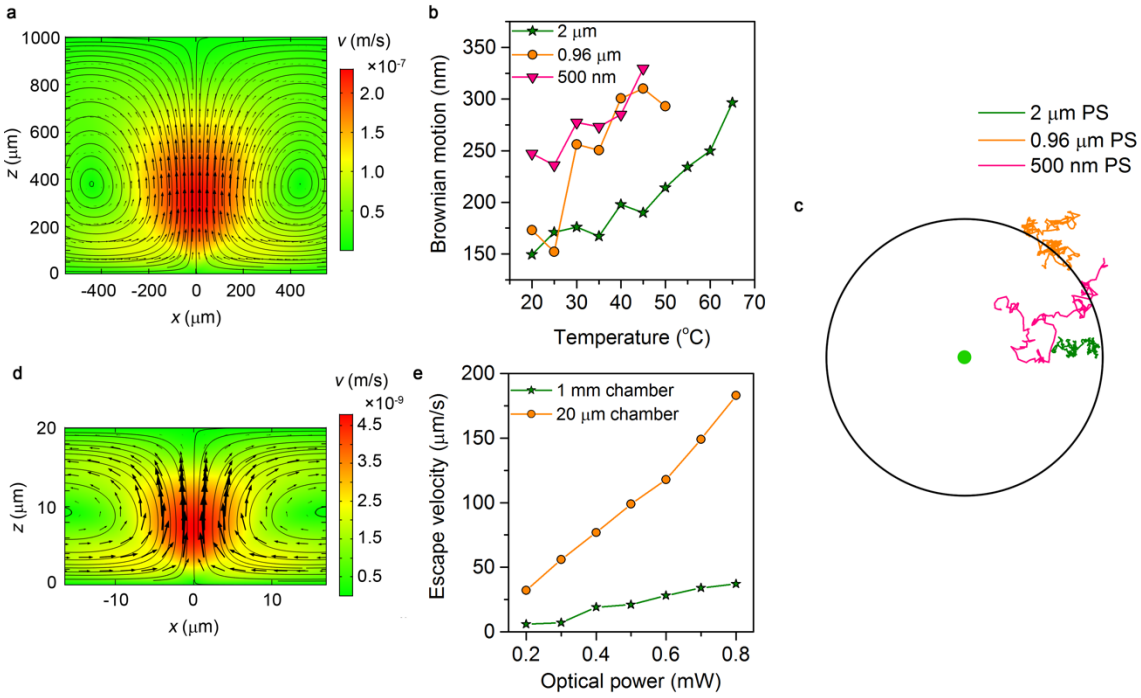

Figure 3.9: Thermal convection effect in the thermophoretic tweezers. (a) Convective flow velocity distribution in a 1 mm chamber. (b) Brownian motion of single PS beads with sizes of 2 μm, 0.96 μm and 500 nm as a function of the working temperature. (c) Measured trajectories of PS beads with sizes of 2 μm, 0.96 μm and 500 nm when the particles were placed 20 μm away from the laser beam for 30 s. The green disk at the center represents the location of the laser beam and the black ring has a radius of 20 μm. (d) Convective flow velocity distribution in a 20 μm chamber. (e) Measured escape velocities of trapped PS beads with a diameter of 0.96 μm in the liquid chambers with a thickness of 1 mm and 20 μm, respectively. In (a-d), an incident laser beam with a diameter of 2 μm and a power of 0.2 mW is focused at the substrate-liquid interface from the substrate side.

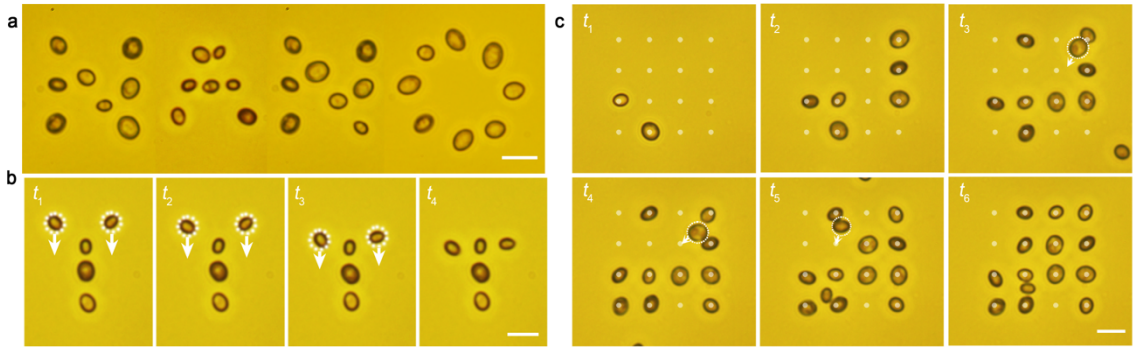

Figure 3.10: Parallel trapping and transport of yeast cells. (a) Parallel trapping of yeast cells in "NANO" pattern. The parallel trapping was achieved for each letter, which was stitched to complete the whole pattern. (b) Transformation of trapped yeast cells from "Y" to "T" pattern by moving two cells as indicated by the arrows. (c) Time-resolved parallel trapping of yeast cells in an array with a 4×4 optical lattice (indicated by white dots). Scale bar: 10 μm.

Live cell trapping and manipulation has been demonstrated using optical tweezers.[95, 115, 116] However, the optical force highly depends on the refractive index contrast between the cells and the solvents, which is known to be small in aqueous solution and limits the optical force. This requires a higher optical power to achieve stable trapping. Because thermophoretic force does not rely on the refractive index contrast between particles and solvents, thermophoretic tweezers allow the low-power and noninvasive manipulation of biological cells. It should be noted that the thermophoretic trapping force relies on the temperature gradient ∇T rather than the temperature increment ΔT or absolute temperature value T, which allows stable trapping without a large temperature rise. Further, the experimental setup can be integrated with a cooling system, which helps to lower the absolute temperature value for cell safety while maintaining the temperature gradient for the cell trapping.

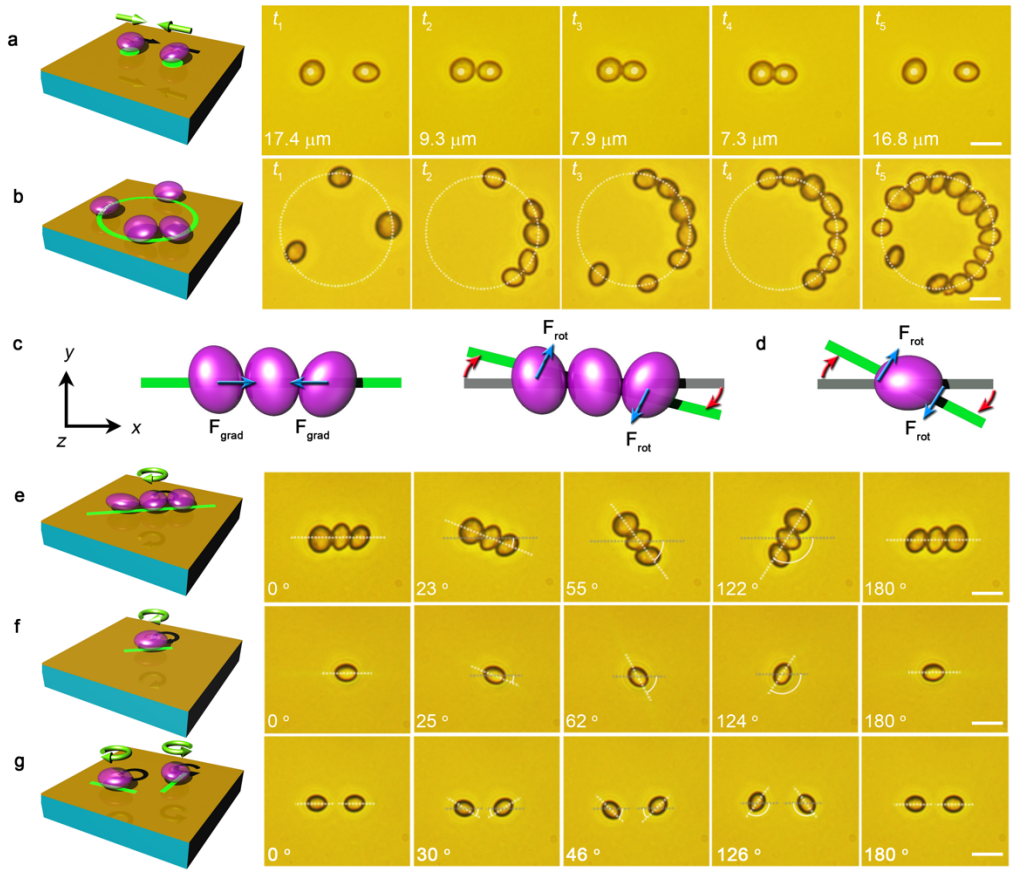

Figure 3.11: Versatile manipulation of yeast cells. (a) Reversible distance control between a pair of yeast cells. The center-to-center inter-cellular distances are indicated. (b) Arrangement of yeast cells in a ring shape. (c) Force analysis in the 1D assembly of yeast cells. (d) Force analysis in the rotation of single yeast cell. (e) Rotation of 1D assembly of three yeast cells. (f) Rotation of a single yeast cell. (g) Independent rotation of two yeast cells using a pair of 1D optothermal potentials. The rotation angles are indicated. Scale bar: 10 μm.

As an example, we used DMD to generate multiple laser beams that simultaneously trapped and arranged yeast cells in "NANO" pattern (Fig. 3.10a). With the power intensity of 0.2 mW (0.06 mW/μm^2) for each beam, all the trapped cells stayed alive. Furthermore, the collective effect among the nanoscale heating sources on the substrate allows

continuous and dynamic manipulation of the temperature gradient field, and therefore the trapped cells. In Fig. 3.10b, we transformed the cell pattern from "Y" to "T" by moving two yeast cells *via* DMD control. From time-resolved parallel trapping of yeast cells into a 4 × 4 array (Fig. 3.10c), we can see that cells occupied 80% of the optical lattice at time t_6. The unoccupied sites are caused by the non-uniform intensity distribution of the optical lattice.

To meet various requirements for studies in life sciences such as cell-cell communication and single-cell analysis,[117] we further demonstrate the capability of thermophoretic tweezers in versatile manipulation of cells. As shown in Fig. 3.11a, we reversibly tuned the cell-cell distance and thus the intercellular interaction between a pair of yeast cells at a resolution of 100 nm. From time t_1 to t_3, the pair underwent from separation to direct contact. Further approaching of the two cells induced pressure and deformation on the cell membranes at the contact point (t_4). The pair was separated again at time t_5.

Geometric design of optothermal potentials in thermophoretic tweezers allows arbitrary control of cell assemblies. As shown in Fig. 3.11b, a ring-shape potential trapped and arranged yeast cells alike. These cells are tangentially free for interactions and radially confined by the optothermal potential. An increased number of the trapped cells led to their close arrangement with direct contact.

Precise control of cell orientation for advanced applications such as 3D cellular microscopy and heterogeneous cell-cell interactions presents a big challenge to many tweezers.[118] The versatility of our thermophoretic tweezers is reflected on their capability of aligning and rotating both single and assemblies of cells at an angular resolution of one degree. As shown in Fig. 3.11c, when three cells were delivered to the 1D potential, the in-plane trapping force confined them along *y* axis. The 1D closely packed cells were aligned

along x axis with cell-cell interactions. Due to intensity gradient of the laser beam along x axis, a weak gradient force F_{grad} pushed the cells toward the center of the 1D optical landscape where the maximum intensity exists. The rotation of the 1D assembly of cells can be achieved by rotating the 1D optical landscape. The rotation of optical landscape creates an offset between the cell location and the optothermal potential, which leads to the in-plane trapping force that acts as the rotation force F_{rot}. When a cell has an elongated shape, the in-plane trapping force intends to align the long axis of the cell with the 1D optical landscape, enabling the rotation of a single cell (Fig. 3.11d). Fig. 3.11e shows the rotation of linear assembly of three yeast cells using a one-dimensional (1D) potential. Rotation of a single yeast cell (Fig. 3.11f) and a pair of yeast cells (Fig. 3.11g) are also demonstrated.

To extend the applicability of thermophoretic tweezers, we have also demonstrated the trapping, alignment, and orientation control of a highly anisotropic *Escherichia coli* cell. As illustrated in Fig. 3.12a, a disk-like optical landscape with a diameter of 2 μm is capable of trapping an *Escherichia coli* cell. With a fixed location of the optical disk, the trapping site on the cell can change during the dynamic manipulation of the cell (Frames t_4 and t_5 in Fig. 3.12a). In contrast, the 1D potential trapped the *Escherichia coli* cell with the cell body aligned along the optical landscape (Fig. 3.12b). Furthermore, the rotation of the *Escherichia coli* cell was also achieved by rotating the optical image with the DMD, as shown in Fig. 3.12c.

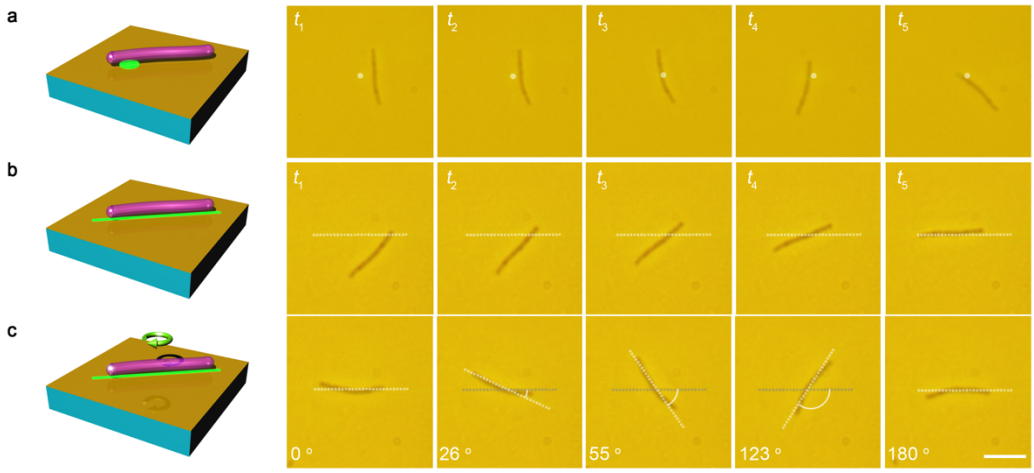

Figure 3.12: Versatile manipulation of *Escherichia coli* cells. (a) Trapping of a single *Escherichia coli* cell using a disk-like optothermal potential with a diameter of 2 μm. Panels t_1 – t_3 show that the cell approached the optical disk. Panels t_4 and t_5 indicate the change of trapping site on the cell. (b) Trapping and orientation control of a single *Escherichia coli* cell using a 1D optothermal potential. Panels t_1 – t_5 show dynamics of the cell trapping and orientation control. (c) Rotation of a single *Escherichia coli* cell. Optical landscapes are indicated by either a white dot or a dotted line. Scale bar: 10 μm.

We have developed thermophoretic tweezers based on coordinated management of light, heat, and fluids *via* the optothermal effect and the interfacial permittivity gradient. The thermophoretic tweezers, which harness thermophoretic force instead of radiation pressure, could also work with incoherent light sources such as light-emitting diodes and Mercury lamps. Sharing the same substrates, surface-enhanced optical spectroscopy can be integrated seamlessly with the thermophoretic tweezers to enable simultaneous measurements of the trapped cells and nanoparticles near the substrates. With the versatile manipulation, simple optics, low power, and *in-situ* high-sensitive spectroscopy, the thermophoretic tweezers will find applications for fundamental and applied research in life sciences and colloidal science, as well as in disease diagnosis and nanomanufacturing.

Chapter 4: Opto-Thermoelectric Tweezers

4.1 Opto-Thermoelectric Trapping of Plasmonic Nanoparticles[5]

Optical manipulation of plasmonic nanoparticles offers the possibility of dynamic control of light-matter interactions at the nanoscale, which is of interest for various applications in nanophotonics, materials science, and life sciences. Optical tweezers have been shown to trap metal nanoparticles in diffraction-limited laser beams with high light intensity, since they provide a sufficient optical gradient force.[119] Although the use of optical tweezers succeeded in trapping Au and Ag nanoparticles with different sizes and shapes,[3, 40, 101, 120-123] it typically encounter technical obstacles. First of all, upon excitation of localized surface plasmons (LSPs) at metal nanoparticles by the trapping laser beam, enhanced light absorption and scattering result in optical heating of the particles and strong optical radiation forces, thereby significantly reducing the trapping stability.[119, 124, 125] As a result, optical trapping is limited to near-infrared lasers with wavelengths far away from the LSP resonance of the metal nanoparticles.[40, 121, 124] Second, optical tweezers can only trap metal nanoparticles with sizes significantly smaller than the laser wavelength (*i.e.*, in the Rayleigh regime), where the nanoparticle can be treated as a dipole. Optical trapping of metal particles with sizes comparable to, or larger than the laser wavelength, is challenging because the enhanced light-scattering cross-section increases the optical scattering force.[119, 126] Finally, high laser power (tens to hundreds of mW) is required to trap subwavelength metal nanoparticles. Such a high optical power can potentially damage the functional materials, surface molecules, or even the trapped metal nanoparticles.[4]

---

[5] Section 4.1 was published in the journal: L. Lin*, M. Wang*, **X. Peng***, E. N. Lissek, Z. Mao, L. Scarabelli, E. Adkins, S. Coskun, H. E. Unalan, B. A. Korgel, L. M. Liz-Marzán, E.-L. Florin, and Y. Zheng, Opto-Thermoelectric Nanotweezers, *Nature Photon.*, 2018, 12, 195-201. I am a leading author.

Optical trapping of metal nanoparticles with LSPs excited at a low optical power is expected to facilitate *in-situ* optical spectroscopy, leading to insights into plasmon coupling and its applications in sensing, imaging, and photothermal therapy. The photothermal effect, or Joule loss, is often recognized as an intrinsic limitation for the use of metal plasmonic nanoparticles in nanophotonic devices.[127, 128] But the Joule loss can also be turned into an advantage. It has been demonstrated that the heat generated can benefit optical trapping by creating an electrothermoplasmonic flow that delivers nanoparticles to the trapping site.[109] Optical confinement of single nanoparticles or macromolecules has been achieved *via* a dynamic temperature field.[62, 63] However, the particles or molecules in the dynamic temperature field undergo frequent and broad position fluctuations. Thermal convective flow and thermophoresis were also employed to trap dielectric microparticles in the hot regions.[19, 129] However, a tweezing platform based on photothermal effects with both low operation power and general applicability is still elusive. More recently, we have proposed a strategy that implements a thermoelectric field to reversibly assemble metal nanoparticles into clusters.[130] Herein, by exploring nanoparticle migration along a light-controlled thermoelectric field, we developed opto-thermoelectric nanotweezers (OTENT) that allow us to capture and manipulate metal nanoparticles at single-particle resolution.

To enable OTENT, we added a cationic surfactant, cetyltrimethylammonium chloride (CTAC), to the nanoparticle colloid solution. CTAC molecules adsorb on the particle surface and form a positively charged molecular double layer (Fig. 4.1a).[131, 132] Simultaneously, CTAC molecules self-assemble into micelles when above the critical micelle concentration (cmc, 0.13-0.16 mM). With a high charge density and nanoscale size, CTAC micelles act as macro cations (known as micellar ions, Fig. 4.1b), which, together with the Cl^- counter-ions (Fig. 4.1c), provide the thermoelectric field in OTENT.

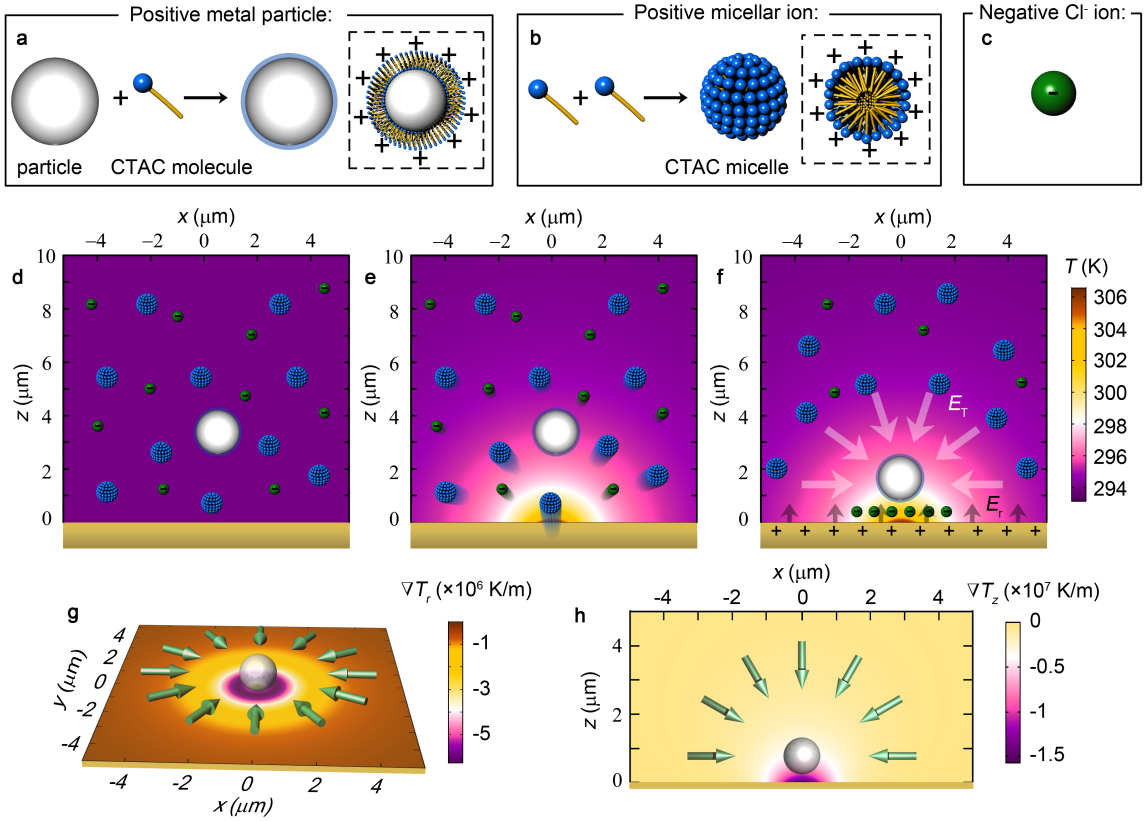

Figure 4.1: Working principle of OTENT. (a) Surface charge modification of a metal nanoparticle by CTAC adsorption. (b) Formation of CTAC micelles. (c) Schematic view of a Cl^- ion. (d) Dispersion of a single metal particle and multiple ions in the solution without optical heating. (e) Thermophoretic migration of the ions under optical heating. (f) Steady ionic distribution under optical heating generates a thermoelectric field E_T for trapping the metal nanoparticle. The repulsive electric field E_r arises from the positive charge of the thermoplasmoic substrate and balances E_T. (g) Simulated in-plane temperature gradient and direction of the corresponding trapping force. (h) Simulated out-of-plane temperature gradient and direction of the corresponding trapping force. The incident laser beam in (e-h) has a diameter of 2 μm and an optical power of 0.216 mW. The green arrows in (g, h) show the direction of the trapping force.

Without optical heating, both the ions and the metal particles are randomly dispersed in the solution, without a preferred migration direction (Fig. 4.1d). To generate an optically controllable temperature gradient field, we directed a laser beam to a

thermoplasmonic substrate, *i.e.*, a porous Au film which was fabricated by simple deposition of a Au layer followed by thermal annealing. A cross-sectional view of the simulated temperature distribution (embedded in the scheme) at the substrate-solution interface is shown in Fig. 4.1e. We can see that a temperature difference of ~12 K was obtained when the porous Au film was irradiated by a 532 nm laser beam at an optical power of 0.216 mW and a beam diameter of 2 μm. It should be noted that the CTAC micelles are thermally stable over a wide temperature range, which is broader than the working temperature range in this work.[133] Both the micellar ions and Cl^- ions undergo thermophoresis, migrating from a hot to a cold region. At the steady state, the spatial redistribution of both CTAC micelles and Cl^- ions generates an electric field, which is given by[15]

$$\boldsymbol{E}_{\mathrm{T}} = \frac{k_{\mathrm{B}} T \nabla T}{e} \frac{\sum_i Z_{\mathrm{i}} n_{\mathrm{i}} S_{\mathrm{T}i}}{\sum_i Z_{\mathrm{i}}^2 n_{\mathrm{i}}} \tag{8}$$

where i indicates the ionic species, *i.e.* CTAC micellar ions or Cl^- ions, k_{B} is the Boltzmann constant, T is the environmental temperature, ∇T is the temperature gradient, e is the elemental charge, while Z_i, n_i, and $S_{\mathrm{T}i}$ are the charge number, the concentration, and the Soret coefficient of i species, respectively.

Since the CTAC micelle has a higher molecular mass and a larger Soret coefficient than the Cl^- ions, *i.e.* S_{T} (micelle) ~10^{-2} K^{-1} > S_{T} (Cl^-) ~7.18×10^{-4} K^{-1}, we obtain an electric field E_{T} pointing toward the laser beam arising from the spatial redistribution of both the CTAC micelles and the Cl^- ions[130, 134], which can trap the positively charged metal nanoparticle at the laser spot, as shown in Fig. 4.1f. Under a temperature gradient of 0.5-3×10^7 K m^{-1}, we estimate the trapping electric field to be 50-300 V m^{-1}. The corresponding in-plane and out-of-plane temperature gradients and trapping forces $F_{\mathrm{T}} = qE_{\mathrm{T}}$ are schematically presented in Figs. 4.1g-h, where q is the charge of the metal nanoparticles.

This trapping electric field is balanced by the repulsive electric field, E_r, arising from the positive charge of the thermoplasmonic substrate, which is also coated by the CTAC double layers. Different from optical tweezers, where the particles are trapped by the optical gradient force from a highly focused laser beam, the trapping electric field in OTENT arises from optical heating, which can relax the rigorous optical requirements of optical tweezers.

We first demonstrate the use of OTENT for trapping and manipulating single Au nanospheres (AuNSs) and Ag nanospheres (AgNSs). Due to their strong light scattering at the LSP resonance wavelengths, AuNSs and AgNSs were tracked with *in-situ* dark-field optical imaging. Fig. 4.2a shows the trapping process of a single 100 nm AgNS using a low-power 532 nm laser beam. The optical intensity we used was 0.05-0.4 mW μm^{-2}, which is 2-3 orders lower than the typical optical intensity in optical tweezers (10-100 mW μm^{-2}). Different from the plasmon-enhanced optical force on plasmonic nanoantennas, which is limited by the decay length of LSPs[6, 109], the temperature gradient field has a much larger working range (Figs. 4.1g-h). Thus, OTENT can effectively deliver the metal nanoparticles to the trapping center within a surrounding region of 5-10 μm in radius and dynamically transport the trapped particle at will by directing the laser beam. As shown in Fig. 4.2b, we delivered a trapped AgNS over a distance of ~110 μm in 9 s. Interestingly, the trapped particle was released as soon as the heating laser was turned off and the temperature gradient field disappeared (Fig. 4.2c).

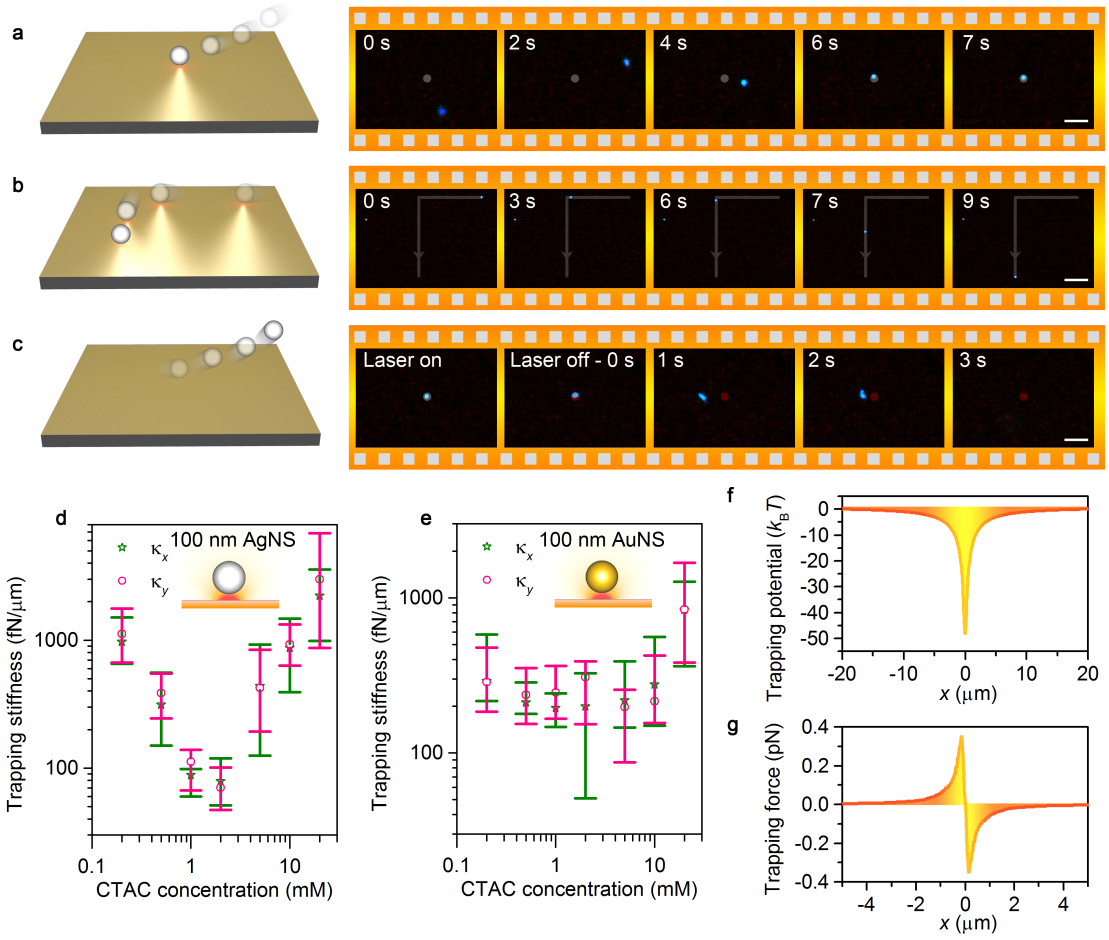

Figure 4.2: Single-nanoparticle trapping and manipulation. Schematic illustration and successive optical images showing (a) trapping (b) dynamic manipulation, and (c) release of a single 100 nm AgNS. The grey disks and the red disks mean that the laser is turned on or turned off, respectively. The grey lines show the manipulation trajectory of the trapped AgNS. Measured trapping stiffness of single (d) 100 nm AgNSs and (e) 100 nm AuNSs as a function of CTAC concentration. κ_x and κ_y are the trapping stiffness along x and y axis, respectively. The error bars show the deviation in multiple measurements with different particles. (f) Trapping potential and (g) trapping force of a single 100 nm AgNS at CTAC concentration of 20 mM. The laser has a wavelength of 671 nm and an optical power of 0.4 mW in d-g. Scale bars: 10 μm (a, c) and 20 μm (b).

To evaluate the trapping stability, we measured the trapping stiffness of OTENT by tracking the Brownian motion of the trapped nanoparticles using a quadrant photodiode.

A low-power laser beam (671 nm, 0.4 mW) was used to trap single metal nanoparticles, including 100 nm AgNSs and 100 nm AuNSs. The measured trapping stiffness ranges from 80 to 2600 fN μm^{-1}. The trapping stiffness is comparable to that of a single 200 nm polystyrene bead trapped by plasmonic Au nanodimers. However, the optical power used in OTENT is 3 orders of magnitude lower than that in the plasmonic tweezers[5]. We also compared the trapping stiffness of OTENT with that of traditional optical tweezers in the trapping of metal nanoparticles. Specifically, for traditional optical tweezers at an optical power of 0.4 mW, optical trapping of a single 100 nm AuNS using a highly focused 1064 nm laser beam has a stiffness of ~2.5 fN μm^{-1}, indicating that the trapping stiffness of OTENT is 2-3 orders of magnitude higher than that of optical tweezers[3].

Furthermore, we can optimize the trapping capability of OTENT by tuning the CTAC concentration that influences the micelle thermophoresis. We have measured the trapping stiffness of 100 nm AgNSs and 100 nm AuNSs at different CTAC concentrations, as summarized in Figs. 4.2d-e. An increase of surfactant concentration reduces the Soret coefficient of the micelles[135, 136] and in turn the electric field intensity, according to Equation (8). In Figs. 4.2d-e, we observe that the trapping stiffness decreases when the CTAC concentration is increased from 0.2 mM to 2 mM, for both 100 nm AgNSs and 100 nm AuNSs. Interestingly, the trapping stability is dramatically improved when the CTAC concentration is further increased. We attribute the improved trapping stability to the increased substrate-particle interaction driven by depletion of CTAC micelles. The thermophoresis of CTAC micelles, *i.e.*, migration from the hot to the cold regions, causes the depletion of CTAC micelles at the particle-substrate gap. The micelle depletion generates an osmotic pressure exerted on the particle to improve its trapping stability. In addition, the depletion attraction significantly reduces the particle-substrate distance, which increases logarithmically the Soret coefficient of the particle[86]. In OTENT, the opto-

thermoelectric field is proportional to the Soret coefficient of the particle, indicating an increased trapping force due to the reduction of the particle-substrate gap. At a CTAC concentration of 20 mM, the trapping stiffness of OTENT for both 100 nm AgNSs and 100 nm AuNSs reaches 1 pN μm^{-1} and even higher despite a low optical power of 0.4 mW. Since the temperature gradient is almost linear at the beam center, the trapping potential there can be treated as harmonic and the whole trapping potential can be further calculated according to the temperature distribution. Fig. 4.2f shows the trapping potential of a single 100 nm AgNS in 20 mM CTAC solution, with a trapping depth of 48 $k_B T$. The maximum trapping force reaches 350 fN (Fig. 4.2g), indicating that a stable trapping of nanoparticles can be achieved at a low optical power. It should be noted that, although the depletion attraction force is not the main driving force to initialize the trapping in OTENT, it is critically important to improve the trapping stability at high CTAC concentration. At 20 mM, the particle-substrate interaction (including depletion attraction, van der Waals interaction, and electrostatic interaction) becomes dominant, yielding a trapping potential of 24 k_BT for a single 100 nm AuNS and reasonably agrees with the measured trapping potential (22.8 k_BT).

To carry out *in-situ* dark-field optical spectroscopy of the trapped metal nanoparticles, we incorporated a high-performance spectrometer into OTENT, as shown in Fig. 4.3a. It should be noted that particle-substrate plasmonic coupling can occur when the particles are trapped in the vicinity of the substrate. However, in OTENT, the backward scattering from the porous Au film is very weak and the particle-substrate plasmonic coupling can be ignored, which provides the possibility to detect the intrinsic scattering spectra from the trapped particles. In Fig. 4.3b, we selectively trapped individual AgNSs according to their scattered colour and recorded the scattering spectra[137]. By matching the experimental spectra with simulated spectra, we verified the sizes of the AgNSs. The colour

of AgNSs changes from violet to blue when the diameter increases from 70 nm to 100 nm, with an improved polarizability, a reduced electric field enhancement factor, and a LSP peak red-shift from 440 to 495 nm. The *in-situ* scattering imaging and spectroscopy of single AuNSs of 80-100 nm in diameter are summarized in Fig. 4.3c. Optical trapping of metal nanoparticles imposes critical requirements on the laser wavelength. For example, it would be challenging to trap AuNSs with a 532 nm laser using optical tweezers, due to the enhanced repulsive optical scattering force by excitation of the LSPs. However, with OTENT we can achieve trapping using lasers with working wavelengths either close to, or far away from the resonance wavelength of the metal nanoparticles.

The versatility of OTENT was explored by trapping nanoparticles with different morphologies. Shown in Fig. 4.3d is the trapping of single anisotropic Au nanotriangles (AuNTs) with different side lengths of 140 nm and 60 nm, respectively. It should be noted that the trapped 60 nm AuNT shows a yellow colour, which arises from a mixture of the red light scattered by the AuNT (646 nm) and the fluorescence and scattering light from the thermoplasmonic substrate. We have also achieved stable trapping of single small Au nanorods (AuNRs) without increasing the incident optical power (Fig. 4.3e). The fluorescence light from the thermoplasmonic substrate dominated over the weak scattered light from the single AuNR, due to its small size. As a result, an overall green colour was observed from the trapped AuNR. Non-luminescent or non-plasmonic substrates with a high absorption coefficient and low thermal conductivity can be used to improve the *in-situ* characterization capability for smaller particles. To further verify that single metal nanoparticles were trapped, we printed the particles on the substrates and checked the samples using scanning electron microscopy. The smallest particles we trapped using low optical power in the current experimental setup were 20 nm AuNSs. It should be noted, while low-power trapping of smaller particles with OTENT is possible, the experimental

demonstration of trapping such particles was limited by our capability for *in-situ* spectroscopic analysis of the trapped particles over the thermoplasmonic substrate. With a suitable detection method, we could experimentally push the size limit of trapped particles down to sub-10 nm through substrate optimization or the use of an ultrafast laser. We have also utilized OTENT to trap large metal nanoparticles (*e.g.*, 400 nm AuNSs), however, the upper size limit remains to be tested. In addition, we also demonstrated that OTENT can be used to manipulate one-dimensional metal nanowires with precise location and orientation control.

The arbitrary light manipulation by means of a digital micromirror device (DMD) allows us to trap and manipulate multiple metal nanoparticles in parallel using OTENT. As shown in Fig. 4.4a, we created six laser beams with the DMD to capture six 100 nm AgNSs, with one nanosphere in each beam. The successive dark-field optical images show the six AgNSs trapped into a circle pattern. As another example, we created and arranged six laser beams into a triangular pattern, where each beam trapped a single 140 nm AuNT (Fig. 4.4b). It should be noted that the metal nanoparticles trapped in parallel can interact with each other through optical binding.[138] However, considering the low optical power used in OTENT, the optical binding force was limited and did not significantly affect the trapping behaviour. Such a parallel nanoparticle manipulation represents an opportunity for dynamic lithography with single-particle resolution.

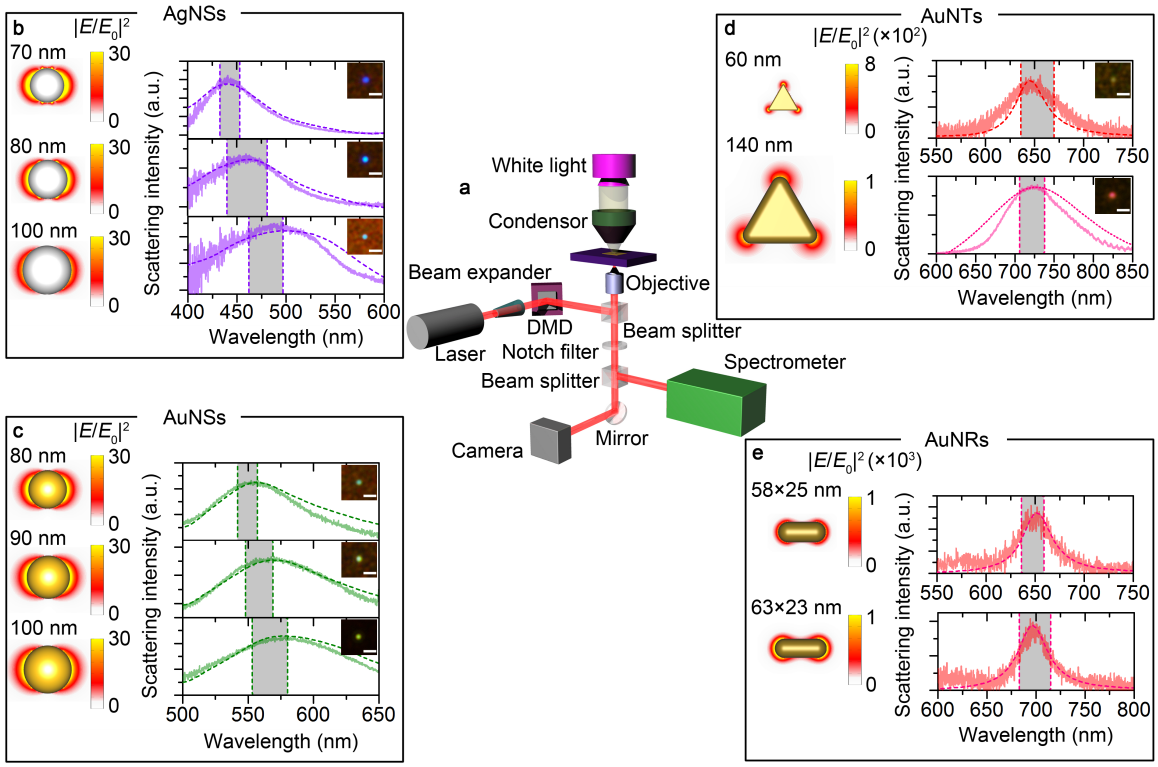

Figure 4.3: *In-situ* optical spectroscopy of different metal nanoparticles trapped *via* OTENT. (a) Optical setup of OTENT with *in-situ* dark-field optical imaging and spectroscopy. Dark-field optical images, experimental and simulated scattering spectra, and electric field profiles of single AgNSs (b) with diameters of 70, 90 and 100 nm; single AuNSs (c) with diameters of 80, 90 and 100 nm; single AuNTs (d) with side lengths of 60 and 140 nm; single AuNRs (e) with lengths of 50-60 and diameters of 19-25 nm and corresponding absorption peaks at around 650 nm (top panel); with lengths of 63-73 nm and diameters of 19-25 nm and corresponding absorption peaks at around 700 nm (bottom panel). The solid and dashed curves represent experimental and simulated scattering spectra, respectively. The grey rectangles represent the peak distributions recorded in multiple experiments. Scale bars: 2 μm.

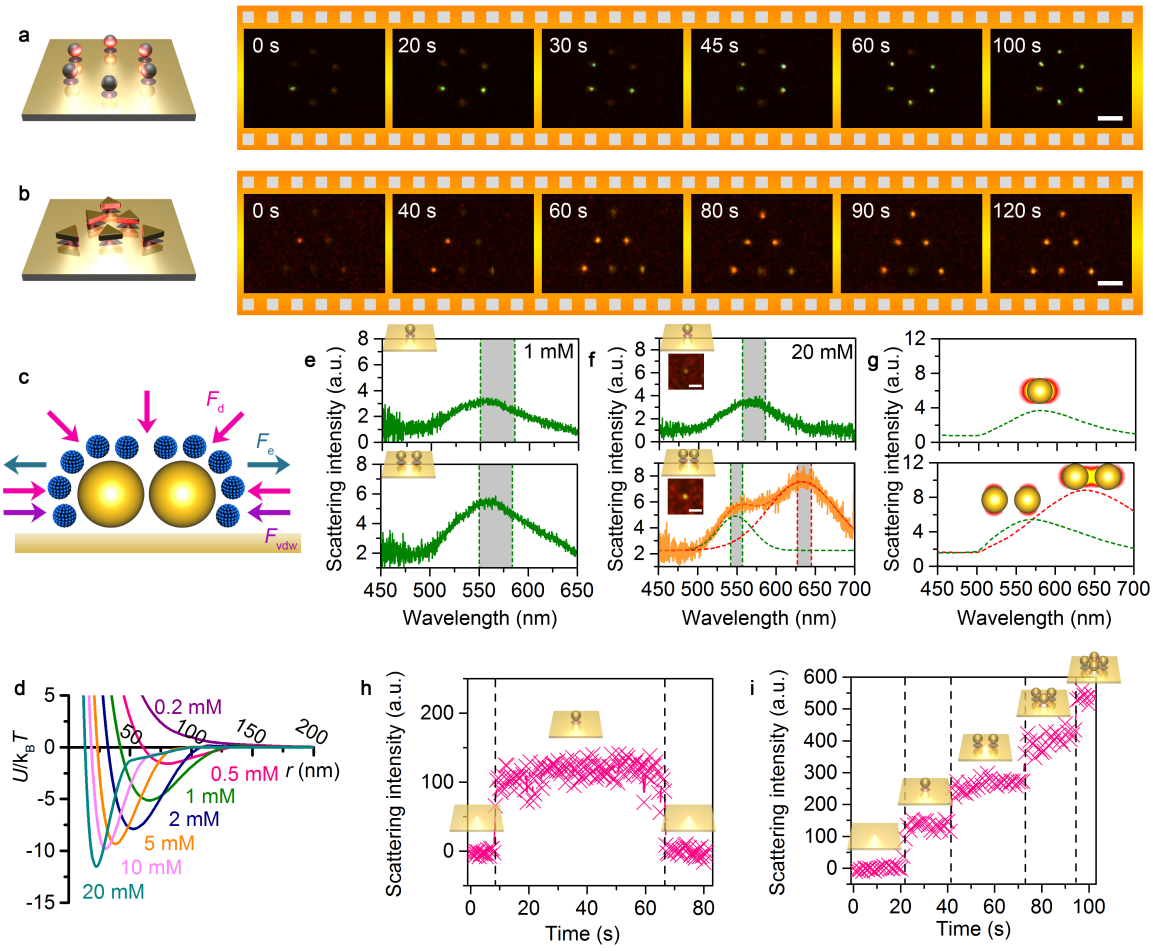

Figure 4.4: Parallel and multiple trapping *via* OTENT. Parallel trapping of (a) six 100 nm AgNSs into a circular pattern, and (b) six 140 nm AuNTs into a triangular pattern. (c) Interaction forces between two trapped nanoparticles. (d) Calculated interaction potential between two AuNSs at different CTAC concentrations. Scattering spectra of a single AuNS (top) and two AuNSs (bottom) in (e) 1 mM and (f) 20 mM CTAC solution. (g) Simulated scattering spectra of a single AuNS (top) and two AuNSs (bottom) in 20 mM CTAC solution. The red and green dashed curve represent the longitudinal and transverse plasmon mode, respectively (f and g). Trapping dynamics of (h) a single AuNS and (i) multiple AuNSs in 1 mM CTAC solution. The grey rectangles represent the peak distributions recorded in multiple experiments. The particle diameter is 100 nm in (d-i). Scale bars: 5 μm (a, b) and 2 μm (f).

We further explored OTENT to trap multiple metal nanoparticles using a single laser beam and to control the particle-particle interactions within the trap. Fig. 4.4c shows three interaction forces between two trapped particles, including the depletion attractive force F_d, van der Waals force F_{vdw}, and electrostatic repulsive force F_e. Assuming that optical heating leads to complete depletion of the CTAC micelles, we calculated the total interaction potential $U_{total} = U_d + U_{vdw} + U_e$, where U_d, U_{vdw}, and U_e are the depletion attraction potential, van der Waals potential, and electrostatic potential, respectively (Fig. 4.4d). The electrostatic interaction between CTAC micelles and AuNSs was also taken into consideration by treating the CTAC micelles as highly charged depletants.[139] We can see that an increase in CTAC concentration leads to a deeper attractive potential with a reduced interparticle gap, which arises from the increased osmotic imbalance and reduced electrostatic repulsion.

Understanding the interaction potential allows us to tune particle-particle plasmon coupling within the trap.[140-142] As a demonstration, we selected two different CTAC concentrations, 1 mM and 20 mM, to tune the interparticle gaps between 65 nm and 25 nm (Fig. 4.4d). We then selectively trapped a single 100 nm AuNS and two 100 nm AuNSs in the 1 mM CTAC solution for *in-situ* optical spectroscopy. As shown in the top and bottom panels of Fig. 4.4e, increased scattering intensity was observed with no spectral shift when the number of the trapped particles changed from one to two at a single thermal hot spot, revealing that no near-field coupling was achieved between the two 100 nm AuNSs. In contrast, we observed that the single scattering peak for a single trapped AuNS split into two peaks when two AuNSs were trapped in the 20 mM CTAC solution. A yellow spot in the dark-field optical image (mixture of the two scattering peaks) with increased scattering intensity also reveals optical coupling between both AuNSs. To further verify the LSP coupling observed in Fig. 4.4f, we simulated the scattering spectra and electric field

enhancement profiles of a single 100 nm AuNS and a 100 nm AuNS dimer with a gap of 25 nm (Fig. 4.4g). We can see that the AuNS dimer with near-field coupling exhibits a longitudinal mode at 638 nm and a transverse mode at 568 nm, which are redshifted and blue-shifted, respectively, with respect to the dipole mode at 580 nm for the single 100 nm AuNS. The simulations match well with the experimental spectra in Fig. 4.4f. This controllable near-field coupling allows us to precisely tune the optical properties of designer colloidal metamaterials.

We further demonstrated *in-situ* monitoring of the trapping dynamics by recording the time-dependent scattering intensity at a specific wavelength. A CTAC concentration of 1 mM was selected to avoid near-field coupling between the trapped particles, and the background from the thermoplasmonic substrate was removed. From Fig. 4.4h, we can see that, once a single 100 nm AuNS was captured by the thermoelectric field, the scattering intensity at 580 nm increased immediately. The scattering intensity fell back to zero once the particle was released. Without significant near-field coupling between the trapped particles, we can also estimate the number of trapped particles according to the recorded photon counts. As shown in Fig. 4.4i, the photon counts increased linearly with the number of AuNSs in the trap, which also verifies that no obvious near-field plasmonic coupling occurs between the multiple trapped AuNSs in 1 mM CTAC solution. It should be noted that the trapped particles can further absorb the incident laser power and increase the temperature around the trapping spot for improved trapping efficiency.

Through an innovative management of light, heat, and electric field in opto-thermoplasmonic fluidics, we developed OTENT for optical trapping and versatile manipulation of metal nanoparticles with single-particle resolution, using *in-situ* optical spectroscopy. In addition to their conventional role in surface modification of metal nanoparticles, ionic surfactants were further exploited to act as micellar ions that create

light-controlled thermoelectric fields, and as charged depletants to manipulate the interaction between trapped particles. As a general tweezing technique, OTENT is applicable to a wide range of metal, semiconductor, polymer, and dielectric nanostructures with charged or hydrophobic surfaces. So far, we have succeeded in trapping silicon nanospheres, silica beads, polystyrene beads, silicon nanowires, germanium nanowires, and metal nanostructures. However, OTENT relies on ionic surfactants in the nanoparticle suspensions to create a thermoelectric field. This requires a solvent environment replacement for nanoparticles that are not dispersed in the ionic surfactants. Challenges may arise for colloidal nanoparticles that cannot be easily modified by surfactants. Additionally, OTENT is primarily a two-dimensional operation platform. 3D manipulation can be realized by using optical fibres coated with photothermal layers. Nevertheless, we propose that, with its low-power and noninvasive operation, diverse options in the trapping wavelength, and generality in size, shape, and composition of the trapped nanoparticles, OTENT will become a powerful tool in colloid science, life sciences, and nanotechnology.

4.2 OPTO-THERMOELECTRIC ASSEMBLY OF PLASMONIC NANOPARTICLES[6]

Associated with the excitation of surface plasmons, metallic nanoparticles can manipulate light at the subwavelength scale where the intense localized electromagnetic field strongly couples with nanoscale objects, leading to various light-matter interaction and applications.[60, 143-147] The optical and electronic properties of plasmonic nanoparticles depend on the particle composition, size, and shape, as well as interparticle interactions.[148-152] Plasmonic nanoparticle assemblies that feature high particle density and small interparticle distance are important for many applications, mainly those based on the

[6] Section 4.2 was published in the journal: L. Lin*, **X. Peng***, M. Wang, L. Scarabelli, Z. Mao, L. M. Liz-Marzán, M. F. Becker, and Y. Zheng, Light-Directed Reversible Assembly of Plasmonic Nanoparticles Using Plasmon-Enhanced Thermophoresis, *ACS Nano*, 2016, 10, 9659-9668. I am a leading author.

multiple electromagnetic "hot spots" that form within the assemblies.[153-156] In particular, the capability of reversibly controlling nanoparticle assemblies with external stimuli enables dynamically tunable plasmon coupling for advanced applications. Reversible assembly has been demonstrated for functionalized metal nanoparticles, driven by external stimuli such as solution pH,[156, 157] local temperature,[158, 159] metal-ion coordination,[160] voltage,[161] and light.[162, 163]

The optical manipulation of plasmonic nanoparticles has advantages for applications such as nanofabrication,[42, 101, 102, 164-166] drug delivery[167, 168] and biosensing.[169, 170] Optical tweezers provide remote, real-time and versatile manipulation of colloidal particles in solution, rendering them highly effective in the reversible assembly of plasmonic nanoparticles.[169-173] In optical tweezers, the optical gradient forces are responsible for the assembly of nanoparticles into aggregates. When the working light is turned off, the assemblies can redisperse into solution due to repulsive electrostatic interactions among the nanoparticles carrying surface charges of the same sign. However, due to the strong light scattering from plasmonic nanoparticles, optical tweezers require tightly focused laser beams of high intensity (10-100 $mW/\mu m^2$)[169-173] to generate a sufficiently strong optical gradient force for the assembly of the nanoparticles. Therefore, unexpected photochemical or thermal reactions (or damage) can occur to molecular analytes under high-power laser illumination.[174, 175] Due to their enhanced local electromagnetic field and strong optical force, surface plasmon polaritons (SPPs) on metallic thin films have been harnessed to reduce the power requirement for optical assembly of nanoparticles over the film.[153] However, there are remaining limitations in exploiting plasmon-enhanced optical forces for the assembly of plasmonic nanoparticles. One limitation is that the high sensitivity of optical forces to plasmon resonances requires a strict overlap between the plasmon resonance wavelength of the nanoparticles and the

working wavelength of the laser beam. This implies that a certain type of laser beam can only work properly for a limited range of nanoparticles with specific plasmon resonances. Another drawback is that, despite the rapid and even ultrafast optical response, it takes a relatively long time (~10 min) to achieve the assembly of nanoparticles in solution because near-field optical trapping on a plasmonic substrate relies on diffusion to bring the nanoparticles into the desired configuration.

Herein, we present a versatile optical technique that uses plasmon-enhanced thermoelectric fields for efficient assembly of plasmonic nanoparticles with dynamic control over assembly size and pattern formation, at low optical power. By introducing a nonphotoresponsive cationic surfactant, namely cetyltrimethylammonium chloride (CTAC), into the plasmonic nanoparticle suspension, we can direct the positively charged nanoparticles toward the laser spot at the interface between a plasmonic substrate and the nanoparticle dispersion. Our experiments and simulations reveal that the plasmon-enhanced temperature gradient field and the thermally induced local electric field give rise to the delivery and assembly of plasmonic nanoparticles. By employing a holographic optical system to control the laser beam, we further achieved parallel and dynamic manipulation of multiple nanoparticle assemblies. Finally, we employed the nanoparticle assemblies with dynamically controlled electromagnetic “hot spots” for surface-enhanced Raman scattering (SERS) analysis of molecules in their native liquid environments. Using rhodamine 6G and methyl orange as model molecules, we investigated the effects of nanoparticle composition and geometry on SERS performance. By taking advantage of the parallel manipulation of multiple nanoparticle assemblies, we demonstrate SERS with enhanced sensitivity.

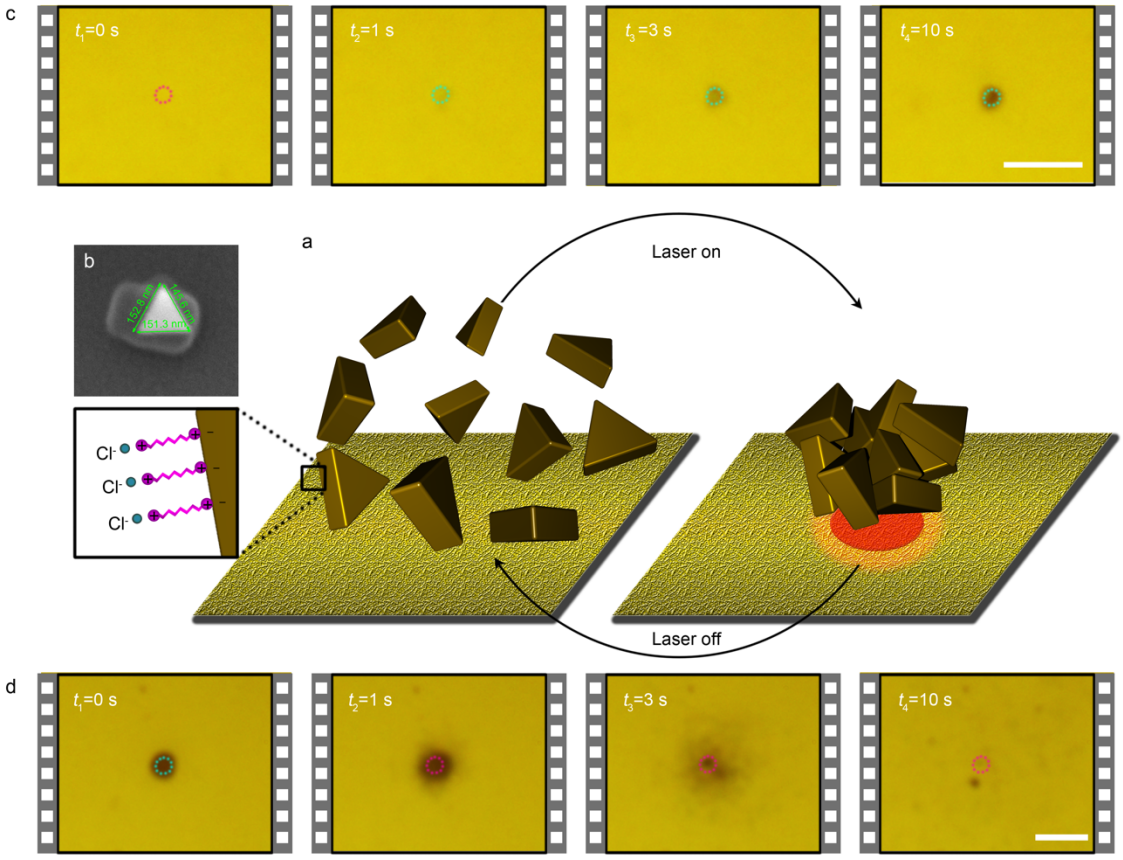

Figure 4.5: Light-directed reversible assembly of plasmonic nanoparticles based on plasmon-enhanced thermoelectric fields. (a) Schematic representation of the light-directed reversible assembly of positively charged AuNTs functionalized with CTAC. (b) Scanning electron micrograph of a single AuNT on the AuNIs substrate. (c) Successive optical images during light-directed assembly of AuNTs. (d) Successive optical images showing the disassembly of a AuNT aggregate after the laser is turned off. The red and blue dotted circles indicate that the laser is off and on, respectively. Scale bars: 10 μm.

Fig. 4.5a illustrates the basic concept of light-directed reversible assembly of plasmonic nanoparticles based on plasmon-enhanced thermoelectricity. We selected Au nanotriangles (AuNTs) as an illustrative example, but other nanoparticles such as Au nanospheres (AuNSs) and Ag nanospheres (AgNSs) have also been used to demonstrate

the generality of our technique. Our AuNTs feature an average side length of ~150 nm (Fig. 4.5b) and a main localized surface plasmon resonance wavelength of 720 nm, which exhibits significantly enhanced electromagnetic fields at the AuNT tips.[176, 177] The AuNTs were dispersed in an aqueous CTAC solution (10 mM). As displayed in the inset of Fig. 4.5a, above the critical micelle concentration (cmc, 0.13-0.16 mM),[178] CTAC forms a bilayer,[179] leading to a positive and hydrophilic surface of the nanoparticle, which is surrounded by Cl^- ions in an electric double layer.

A plasmonic substrate comprising Au nanoislands (AuNIs) was employed to induce the plasmon-enhanced photothermal effect, which allows us to use a low optical power to create an appropriate temperature-gradient field for the thermophoretic assembly of nanoparticles. It should be noted that the AuNIs substrate can be easily fabricated by deposition of a Au thin film followed by postannealing. When the plasmonic substrate is illuminated with a low power laser beam, the plasmonic heating of the AuNIs on the substrate increases the temperature of the surrounding environment. Thermoelectric fields then arise from the temperature gradient and enables the rapid formation of AuNT assemblies at the laser spot, in the vicinity of the substrate-solution interface (Fig. 4.5c). Successive optical images of the light-directed assembly process are shown in Fig. 4.5c, revealing the formation of a stable AuNT assembly at t_4 = 10 s. Importantly, the AuNTs can redisperse into the solution once the laser is turned off (Fig. 4.5d).

The assembly of AuNTs is caused by particle migration in the thermally induced local electric field, *i.e.* thermoelectric effect.[14, 15] As illustrated in Fig. 4.6a, a light-induced local temperature gradient imposes a non-uniform concentration of CTAC micelles, due to the thermal response of the positively charged micelles. The positive surface of CTAC micelles is surrounded by Cl^- ions, giving rise to an electric double layer. Treating these positive micelles as macroions, we obtain the Debye screening length λ_{DH}:

$$\lambda_{\mathrm{DH}} = (\frac{\varepsilon k_{\mathrm{B}} T}{2Ie^2})^{1/2} \quad (9)$$

where ε is the dielectric constant of the liquid, k_{B} is Boltzmann's constant, T is the absolute temperature, e is the electron charge, and I is the ionic strength. In the absence of added salt in the solvent, the ionic strength I is dominated by the total surfactant concentration, c, and the cmc. In the presence of the temperature gradient field, the asymmetric ion distribution in the electric double layer exerts a pressure and causes slip flow of the liquid, which can be described with the excess enthalpy h within an interaction length λ:[84]

$$\boldsymbol{v}_{\mathrm{s}} = D_T^{\mathrm{mic}} \nabla T = -\frac{1}{\eta} \int_0^{\infty} dz[zh(z) \frac{\nabla T}{T}] \quad (10)$$

where D_T^{mic} denotes the thermal diffusion coefficient of the micelles. Considering the Debye-Hückel approximation h=-1/2$\varepsilon(\zeta/\lambda)^2 e^{-2z/\lambda}$, where ζ is the surface potential. The thermal diffusion coefficient:

$$D_T^{\mathrm{mic}} = \frac{\varepsilon \zeta^2}{8\eta T} \quad (11)$$

where η is the viscosity of the liquid. A positive D_T^{mic} indicates that the liquid flow moves from cold to hot region, while in the laboratory frame, the micelles move in the opposite direction, *i.e.* from hot to cold region, which is independent on the sign of ζ. The highly charged micelles give rise to the surface potential, and it is estimated that D_T^{mic}~10^{-11} m^2/Ks for CTAC micelles at a concentration of 10 mM. Even though Cl^- ions have higher mass diffusion coefficient (2×10^{-9} m^2/s)[15] than the micelles (6×10^{-10} m^2/s),[180] the extremely low Soret coefficient of Cl^- ions (7×10^{-4} 1/K) leads to a lower $D_T^{\mathrm{Cl}^-}$~10^{-12} m^2/Ks.

The higher D_T^{mic} drives the positive CTAC micelles toward the cold region quickly and leads to the separation between negative and positive ions, thereby generating a temperature-dependent local electrostatic potential $\left(\frac{\nabla T}{T}\right)\psi_0$, as illustrated in Fig. 4.6a. This exerts an electric force on the positive AuNTs and drives migration of the particles toward the hot region (*i.e.* the laser beam spot) to form the assembly. According to Helmholtz-

Smoluchowski electrophoretic mobility $\varepsilon\zeta/\eta$, the thermal diffusion coefficient of the AuNTs can be calculated using:[9]

$$D_T^{\mathrm{NP}} = \frac{\varepsilon\zeta^{\mathrm{NP}}\psi_0}{\eta T} \tag{12}$$

We can estimate $D_T^{\mathrm{NP}} \sim 10^{-12}$ m^2/Ks, which agrees with the order of magnitude of the measured trapping velocity of the AuNTs (several micrometers per second).

To estimate the plasmon-enhanced photothermal effect and its role in the assembly of the plasmonic nanoparticles, we simulated the temperature gradient profiles at the substrate-solution interface upon illumination with a laser beam, as displayed in Figs. 4.6c-e. When a 532 nm laser beam (power: 0.1 mW, diameter: 2 μm) is incident on the plasmonic substrate, a moderate temperature gradient of ~0.6 K/μm is obtained on top of the substrate. The rapid migration of the AuNTs to the hot region at the interface between the substrate and solution leads to growth of the aggregate. It should be noted that the AuNTs assembled on top of the plasmonic substrate absorb light that would otherwise be transmitted through the substrate, which further increases the photothermal effect and the temperature gradient. As displayed in Fig. 4.6d, when a AuNT assembly with a diameter of 2 μm forms on top of the plasmonic substrate, the transmitted light through the substrate is completely absorbed by the AuNT assembly, leading to a temperature gradient of ~0.7 K/μm.

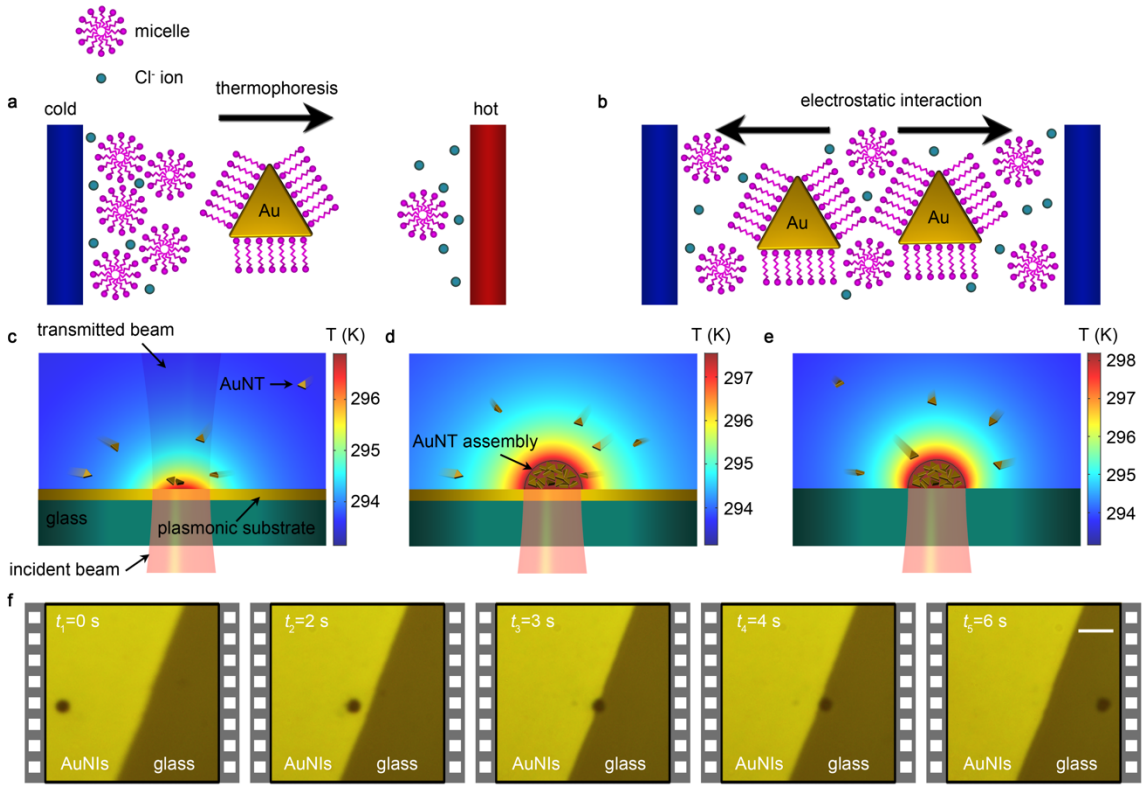

Figure 4.6: Working principle of light-directed reversible assembly of plasmonic nanoparticles (using AuNTs as an illustrative example). (a) Schematic illustration of the migration of a CTA^+-modified AuNT from the cold to the hot region in a light-induced temperature-gradient field, which is known as thermophoresis. (b) Schematic illustration of the release or redispersion of a AuNT assembly due to electrostatic repulsive interaction when the laser is off and the temperature-gradient field disappears. Simulated temperature distribution at the interface between plasmonic substrate and particle solution in a cross-sectional view: (c) Before the formation of a AuNT assembly; (d) after the formation of a AuNT assembly. (e) Simulated temperature distribution at the interface between a glass substrate and nanoparticle solution in a cross-sectional view, in the presence of a AuNT assembly, indicating that the light-directed AuNT assembly can be transported from the plasmonic substrate to the glass substrate. (f) Time-evolved optical images illustrate that we can transport the AuNT assembly from a plasmonic substrate to a glass substrate by simply translating the sample stage. Scale bar: 10 μm.

The optical power density used herein (~0.03 $mW/\mu m^2$) is at least 3 orders of magnitude lower than that used in optical tweezers for nanoparticle assembly.[169, 170, 173] We

find that an optimal optical power is required to create the stable assembly of nanoparticles with plasmon-enhanced thermophoresis. A too low optical power (< 0.01 mW/μm^2) cannot create a sufficiently strong local electric field to trap the nanoparticles as required for the assembly process. However, a too high optical power (> 0.15 mW/μm^2) will induce strong thermal convection and Brownian motion of the plasmonic nanoparticles, causing instability of the particle assembly.

Further, we find that, while the AuNIs-based plasmonic substrate is required to initiate the light-directed assembly of nanoparticles *via* the plasmon-enhanced photothermal effect, it is not essential to maintain and to dynamically manipulate the assemblies once formed. The nanoparticle assembly itself becomes a heating source to maintain the force balance. As shown in Fig. 4.6e, the light absorption by a AuNT assembly on a glass substrate can generate a temperature gradient of ~0.8 K/μm, which is even higher than that on the plasmonic substrate. Unlike the plasmonic substrate where the incident light is partially reflected at the interface between AuNIs and glass substrate, the glass substrate exhibits a significantly reduced reflection loss. The self-sustainability of the heating source sets the foundation for delivering a stable nanoparticle assembly over a non-plasmonic substrate. As experimentally demonstrated in Fig. 4.6f, a stable AuNT assembly with a diameter of 4 μm was generated over the plasmonic substrate at t_1, and transported across the AuNI/glass boundary at t_2 - t_4 and over the glass substrate at t_5 (6 s). The transport was achieved by simply translating the sample stage.

We exclude the contribution of optical tweezing effect to our light-directed assembly of nanoparticles. Focusing the same laser beam at the interface of a glass substrate and the nanoparticle dispersion could not initiate nanoparticle assembly, indicating that the optical force from the focused laser beam cannot trap and assemble the nanoparticles in this case. One may argue that the plasmon-enhanced optical force on the

plasmonic substrate can improve the trapping and assembling capability of nanoparticles. However, the AuNIs plasmonic substrate exhibits weak electromagnetic field enhancement under laser illumination, which is far away from the condition for the maximum optical gradient force that is strong enough for particle assembly.[181] To further verify our hypothesis, we irradiated the same laser beam at the interface of AuNIs substrate and nanoparticle suspensions without CTAC surfactant (AuNSs stabilized in PBS solution). As expected, no assembly of the nanoparticles occurred due to the absence of the thermoelectric effect.

Taking advantage of versatile light management *via* holographic optics, we achieved efficient manipulation of multiple nanoparticle assemblies. The optical setup is displayed schematically in Fig. 4.7a. A spatial light modulator (SLM) was used to dynamically control the laser beam in an arbitrary manner. Desired optical patterns on the plasmonic substrate were obtained by focusing an expanded laser beam that is modulated by the SLM onto the substrate.

Through engineering the optical patterns on the plasmonic substrate, we demonstrate simultaneous generation of 25 AuNT assemblies in a 5×5 square array (Fig. 4.7b). Another example is 17 AuNT assemblies in an "Au" pattern (Fig. 4.7c). Despite an optical power variation of ~20% among the different laser beams generated by the SLM, which is caused by the design algorithm, we can still generate the multiple AuNT assemblies with high uniformity and stability. Furthermore, we demonstrate the dynamic manipulation of the AuNT assemblies, as shown in Fig. 4.7d. In the demonstration, we generated 13 AuNT assemblies in a "UT" pattern at t_1. A series of transport processes of selected assemblies is implemented to transform the pattern, as shown from t_1 to t_6 in Fig. 4.7d.

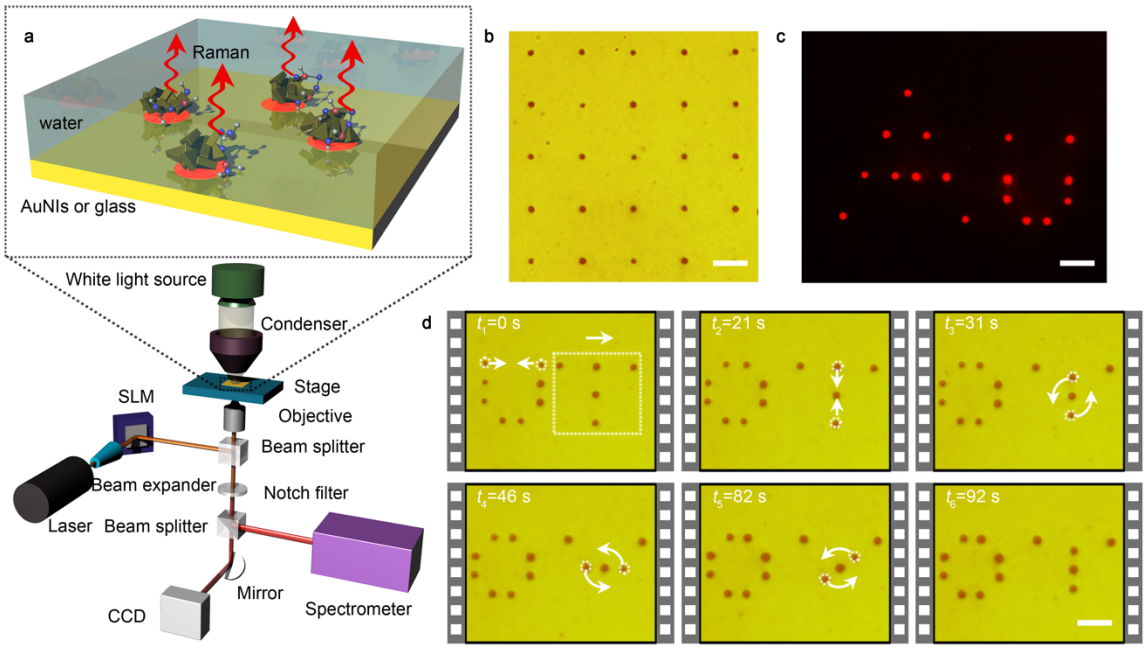

Figure 4.7: Parallel and dynamic manipulation of multiple nanoparticle assemblies. (a) Schematics of the optical setup for nanoparticle assembly manipulation and "multiplex" *in-situ* SERS. (b) Optical image of 25 AuNT assemblies in a 5×5 square array. (c) Dark-field optical image of 17 AuNT assemblies in an "Au" pattern. (d) Time-evolved optical images of dynamic manipulation of selected AuNT assemblies to transform the pattern. Scale bars: 10 μm. The total power of the 532 nm working laser beam is 7.9 mW, 3.6 mW and 3.6 mW for the parallel manipulation in (b), (c), and (d), respectively. The diameter of individual laser beams for single assemblies is 2 μm.

Since the formation of nanoparticle assemblies only relies on the photothermal effect from the plasmonic substrate and the CTAC surfactant, we expect that our technique is applicable to metallic nanoparticles with different materials, sizes. and shapes. Along this line, we demonstrate the light-directed assembly of metal nanoparticles of different compositions, sizes, and shapes, as discussed below. This versatile manipulation of the nanoparticle assemblies can be harnessed as dynamic lithography to form arbitrary patterns of dispersed nanoparticles at solid-liquid interfaces. With their reversible characteristics, the lithographic patterns can be "erased" and "rewritten" repeatedly. The minimum size of

a single nanoparticle assembly can reach ~1 μm with our current optical setup, which is determined by the size of the laser spot. The light-directed dynamic manipulation of multiple nanoparticle assemblies also allows us to develop an *in-situ* SERS platform with enhanced sensitivity, as discussed below.

Exploiting the plasmon-enhanced electromagnetic field at plasmonic nanostructures, SERS is an advanced analytical technique that can detect molecules with a sensitivity down to the single-molecule level.[182-185] A number of approaches have been implemented to enhance the localized electromagnetic field and improve the SERS sensitivity, including tailoring the particle shape[176, 186, 187] and inducing near-field coupling.[155, 188-192] The integration of optical tweezers with SERS (also known as SERS tweezers) is applied for analyzing biomolecules in their native environments and developing optofluidics-based lab-on-a-chip systems.[169-172] However, the high optical power required for nanoparticle manipulation in optical tweezers can potentially damage the biomolecules,[154] which limits the applications of SERS tweezers.

With low-power operation and reversible assembly of plasmonic nanoparticles, our plasmon-enhanced thermophoretic technique has advantages for its use in SERS tweezers, as demonstrated herein by *in-situ* molecular sensing. SERS measurements can also be applied to monitor the dynamics of light-directed nanoparticle assembly. Considering the critical role of CTAC in the assembly of nanoparticles, we investigated the effects of CTAC concentration on the performance of SERS based on our nanoparticle assemblies. For this study, we used AuNS assemblies as the SERS substrates and rhodamine 6G as the targeted molecules. A single laser beam was used for both inducing nanoparticle assembly and Raman excitation. As we show in Fig. 4.8a, SERS intensities at 614 cm^{-1} (C-C-C ring in-plane bending mode) and 1510 cm^{-1} (aromatic C-C stretching mode)[193] are highly sensitive to CTAC concentration. Specifically, both modes experience an increase and then a

decrease in intensity when CTAC concentration was increased from 2.5 to 75 mM. An optimal CTAC concentration of 10-25 mM was identified for the highest SERS intensities, which is likely due to the opposite trend of two different parameters with the concentration of CTAC molecules. On one hand, the increased concentration of CTAC molecules leads to an enhanced thermally induced electric field, which generates stable nanoparticle assemblies with stronger localized electromagnetic field and more intense SERS signals. On the other hand, the increased concentration of CTAC hinders the adsorption of the targeted molecules on the plasmonic nanoparticles, leading to weaker Raman enhancement.

We can further exploit the near field coupling between the plasmonic substrates and the plasmonic nanoparticle assemblies to improve the SERS performance. Figs. 4.8b-c summarize the dependence of the SERS intensities (of modes at 614 cm^{-1} and 1510 cm^{-1}) on the size of AuNT assemblies over a plasmonic substrate and a glass substrate, respectively. In both cases, the SERS intensity increases with the size of the aggregate, which can be attributed to the increased number of plasmonic "hot spots" and targeted molecules in the larger assemblies. A significant improvement of SERS performance is observed for assemblies over the plasmonic substrate due to assembly-substrate plasmon coupling. In addition, we notice that the SERS sensitivity of AuNT assemblies is almost an order of magnitude higher than that of AuNS assemblies because the AuNTs exhibit significantly enhanced electromagnetic fields at their tips. It should be noted that exposure time in Fig. 4.8a was ten-fold longer than that in Figs. 4.8b-c.

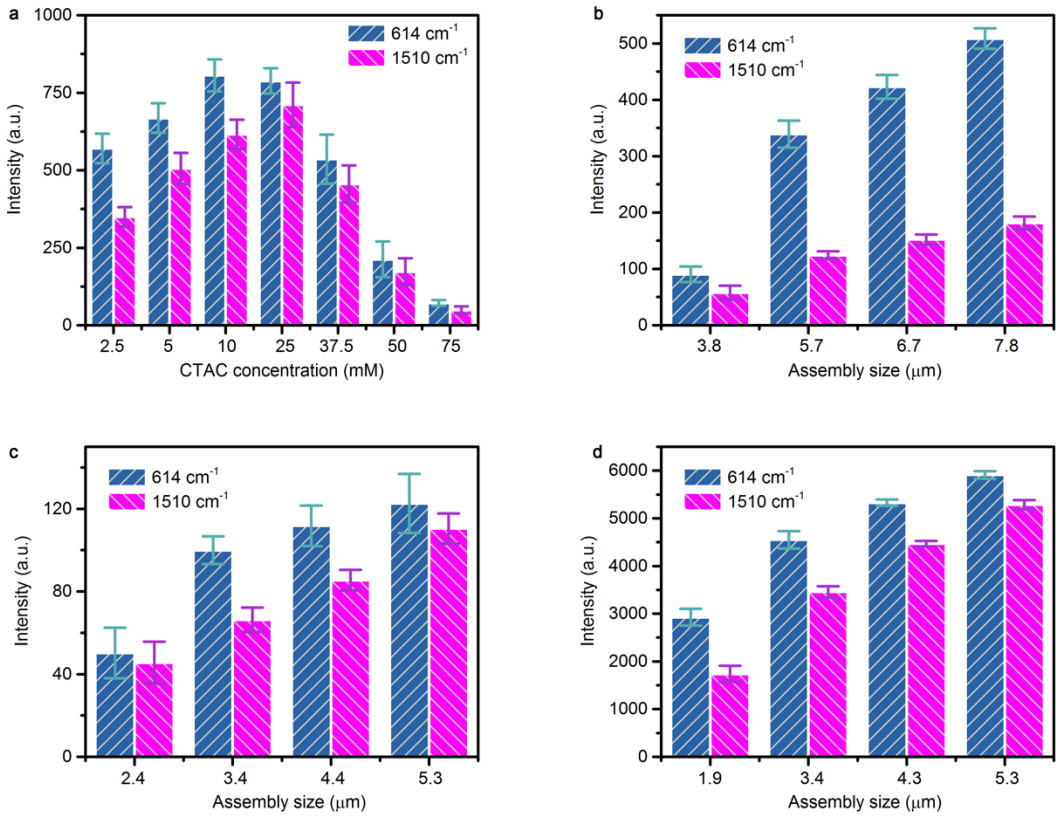

Figure 4.8: Parametric study of SERS of rhodamine 6G on plasmonic nanoparticle assemblies. (a) SERS intensities of 614 cm^{-1} and 1510 cm^{-1} modes as a function of CTAC concentration in the AuNS solution. The size of AuNS assemblies over the plasmonic substrate was maintained at 4.0±0.2 μm; (b) Assembly-size-dependent SERS intensities of the modes at 614 cm^{-1} and 1510 cm^{-1}, based on AuNT assemblies over a plasmonic substrate; (c) Assembly-size-dependent SERS intensities of the modes at 614 cm^{-1} and 1510 cm^{-1}, based on AuNT assemblies over a glass substrate; (d) Assembly-size-dependent SERS intensities of the modes at 614 cm^{-1} and 1510 cm^{-1}, based on AgNS assemblies over a plasmonic substrate. A 660 nm laser beam with a power of 0.27 mW and a diameter of 2 μm was used for both nanoparticle assembly and SERS measurements. The rhodamine 6G concentration was 1 mM. Acquisition times were 10 s in (a) and 1 s in (b)-(d).

We extended our technique to reversibly assemble AgNSs and then applied the AgNS assemblies for SERS detection of rhodamine 6G. Fig. 4.8d shows the dependence on assembly size of the SERS intensities for two modes (614 cm^{-1} and 1510 cm^{-1}). AgNSs

with a diameter of ~100 nm exhibit a plasmon resonance wavelength of 480 nm, which is much shorter than the wavelength of our working laser beam (660 nm). Compared with AuNTs, AgNSs exhibit smaller maximum assembly size because of the faster Brownian motion of the smaller AgNSs and the weaker photothermal effect at the AgNS assembly. Still, AgNS assemblies exhibit significantly higher SERS efficiency than AuNT assemblies, with an enhancement factor 1 order of magnitude higher. Our observation is consistent with previous studies regarding the superior SERS performance of Ag nanoparticles.[194]

We additionally evaluated the ultimate SERS sensitivity by studying the dependence of SERS signals on the concentration of rhodamine 6G, using a single AgNS assembly as SERS substrate. As shown in Fig. 4.9a, we obtained a detection limit of ~1 μM for an acquisition time of 10 s. To further enhance the SERS sensitivity, one strategy comprised drying of the nanoparticle assemblies. The hydrophobic interactions between the CTA^+ tails maintain the CTA^+ double layers, which exert the electrostatic repulsive force on the nanoparticles to maintain a certain interparticle distance. Solvent removal would eliminate the hydrophobic interaction and damage the CTA^+ double layers, thereby reducing the repulsive force. Therefore, we expected that a dried nanoparticle assembly would become more compact, with smaller interparticle distances due to stronger van der Waals interactions and weaker electrostatic repulsive forces. The more compact assemblies can thus enhance the local electromagnetic field at "hot spots" and the Raman signals of the molecules would be further amplified. Fig. 4.9b shows the time-resolved SERS spectra of rhodamine 6G recorded from a single AgNS assembly during solvent evaporation, indeed showing an increase of the signal.

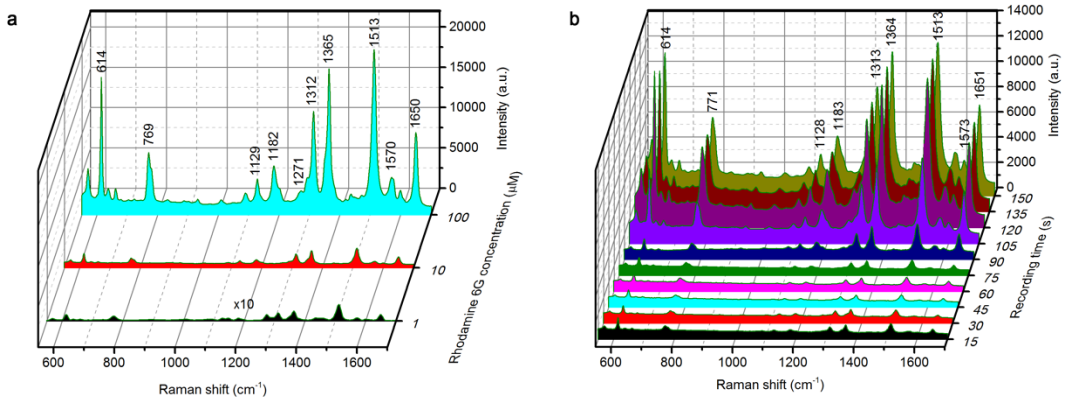

Figure 4.9: (a) SERS spectra recorded from single AgNS assemblies over a plasmonic substrate, for different concentrations of rhodamine 6G. The assembly size is 5.0±0.2 μm. (b) Time-resolved SERS spectra of rhodamine 6G (10 μM) based on a single AgNS assembly during the solvent evaporation. At 0 s, the assembly is immersed in the solvent. At 135 s, the assembly is 100% dry. A 660 nm laser beam with a diameter of 2 μm and a power of 0.27 mW (a) and 0.32 mW (b) was used for both nanoparticle assembly and SERS measurements. Acquisition times were 10 s (a) and 15 s (b).

We have developed a general method for light-directed reversible assembly of plasmonic nanoparticles based on plasmon-enhanced thermophoresis. The nonphotoresponsive CTAC surfactant forms a double layer to create a hydrophilic and positive nanoparticle surface. Such surface-functionalized nanoparticles can be driven into the hot region on top of a plasmonic substrate, under the plasmon-enhanced temperature-gradient field. The coordinated action from thermophoresis induced electric force, electrostatic repulsive force, and van der Waals attraction enables the reversible assembly of plasmonic nanoparticles regardless of their composition, size, and shape. Using a holographic optical system, we achieved parallel manipulation of multiple particle assemblies. Compared with optical tweezers, our thermophoretic method features lower optical power and higher assembly efficiency, with simpler optics. Furthermore, we

demonstrate that these plasmonic nanoparticle assemblies can be applied for SERS with enhanced sensitivity. With low power and parallel operation, reversible nanoparticle assembly, and general applicability to arbitrary nanoparticles, our technique will find applications in particle trapping, manipulation, patterning, and biosensing.

Chapter 5: Opto-Thermoelectric Printing

5.1 Opto-Thermoelectric Printing of Colloidal Particles in Salt Solutions[7]

Colloidal particles exhibit interesting properties, which are precisely tunable *via* their sizes, shapes, and compositions.[195-197] They are promising as building blocks for various functional devices.[198-202, 203, 204] To build such functional devices, one need transfer colloidal particles from aqueous solutions onto solid-state substrates. Interparticle, particle-solvent, particle-substrate, and solvent-substrate interactions need be precisely controlled to obtain desired patterns of colloidal particles on the substrates.[205-207] A myriad of printing techniques has been applied to create patterned colloidal particles on the substrates. Ink-jet printing can deposit colloidal particles into arbitrary patterns in a serial, non-contact, and maskless manner.[208, 209] Micro-contact printing can create patterned arrays of colloidal particles in parallel *via* transfer process using stamps.[38]

Recently, optical force has been harnessed to assemble colloidal particles at single-particle resolution. For example, holographic optical tweezers were applied to trap and organize individual particles into any desired patterns in suspensions, which were immobilized in polymer matrices *via* photo-polymerization.[210] UV-triggered click-chemistry was also applied to link optically trapped particles onto functionalized substrates.[211] Plasmon-enhanced optical scattering force was exploited to push plasmonic nanoparticles in suspensions onto the substrates where the nanoparticles were bonded with van der Waals force.[42, 102, 165, 212]

---

[7] Section 5.1 was published in the journal: L. Lin*, **X. Peng***, and Y. Zheng, Reconfigurable Opto-Thermoelectric Printing of Colloidal Particles, Chem. Commun., 2017, 53, 7357-7360. I am a leading author.

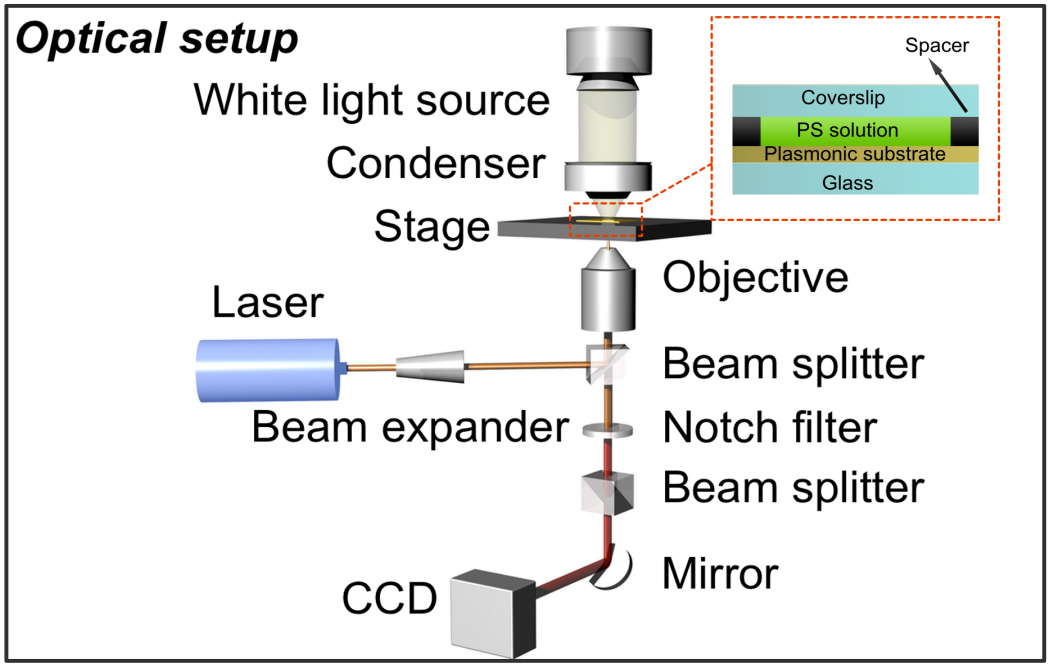

Figure 5.1: Schematic illustration of optical setup for opto-thermoelectric printing (OTP). In this figure, polystyrene colloidal particles (indicated by PS solution) are printed on plasmonic substrates.

Despite their versatile patterning of colloidal particles at single-particle resolution, current optical techniques have limitations. Specifically, optical tweezers require well-focused high-power laser beams and complex optics. Additional chemical reactions are often required to immobilize the optically assembled colloidal particles in polymer matrices or on substrates. While the plasmon-enhanced optical scattering force is capable of printing the particles on the substrate, it is only applicable to plasmonic nanoparticles.[213] Herein, to overcome the limitations, we have developed an opto-thermoelectric printing (OTP) technique that uses simple low-power optics. The OTP employs light-controlled thermophoresis to trap and print colloidal particles at single-particle resolution. Moreover,

the OTP allows us to selectively release the printed particles and to reprint them at new sites, enabling reconfigurable patterning of particles.

Thermophoresis has proved effective in low-power transport of particles and molecules in fluids.[17, 63, 114, 214] Driven by a thermoelectric field that arises from the concentration gradient of ions in the fluids, *i.e.*, the Seebeck effect, colloidal particles can migrate along a temperature gradient.[14, 15, 136] For the OTP, we balance light-induced macroscopic electric fields, localized electric fields, and particle-substrate depletion attraction to achieve optical trapping, printing, releasing and reprinting of colloidal particles. With its versatile and reconfigurable colloidal patterning using simple low-power optics, the OTP will find applications in cellular biology, tissue engineering, and fabrication of metasurfaces.[215-217]

Our experimental setup for the OTP is depicted in Fig. 5.1. For an initial demonstration, we chose a plasmonic substrate for its high opto-thermal conversion efficiency. The plasmonic substrate is consisted of networked Au nanoparticles of sizes of 20-40 nm on a glass slide, which exhibits localized surface plasmon resonances at a visible wavelength. A mixed solution of polystyrene (PS) spheres, NaCl (10-100 mM), and cetyltrimethylammonium chloride (CTAC) molecules (0.05-10 mM) was sandwiched between the substrate and a coverslip with a spacer of 120 μm in thickness (inset in Fig. 5.1). When a 532 nm laser beam was focused onto the plasmonic substrate, a plasmon-enhanced collective heating regime was established at the substrate-solution interface, leading to a temperature gradient that points toward the laser beam center.[181] The reconfigurable printing of colloidal particles was monitored with a CCD integrated into the optical microscope.

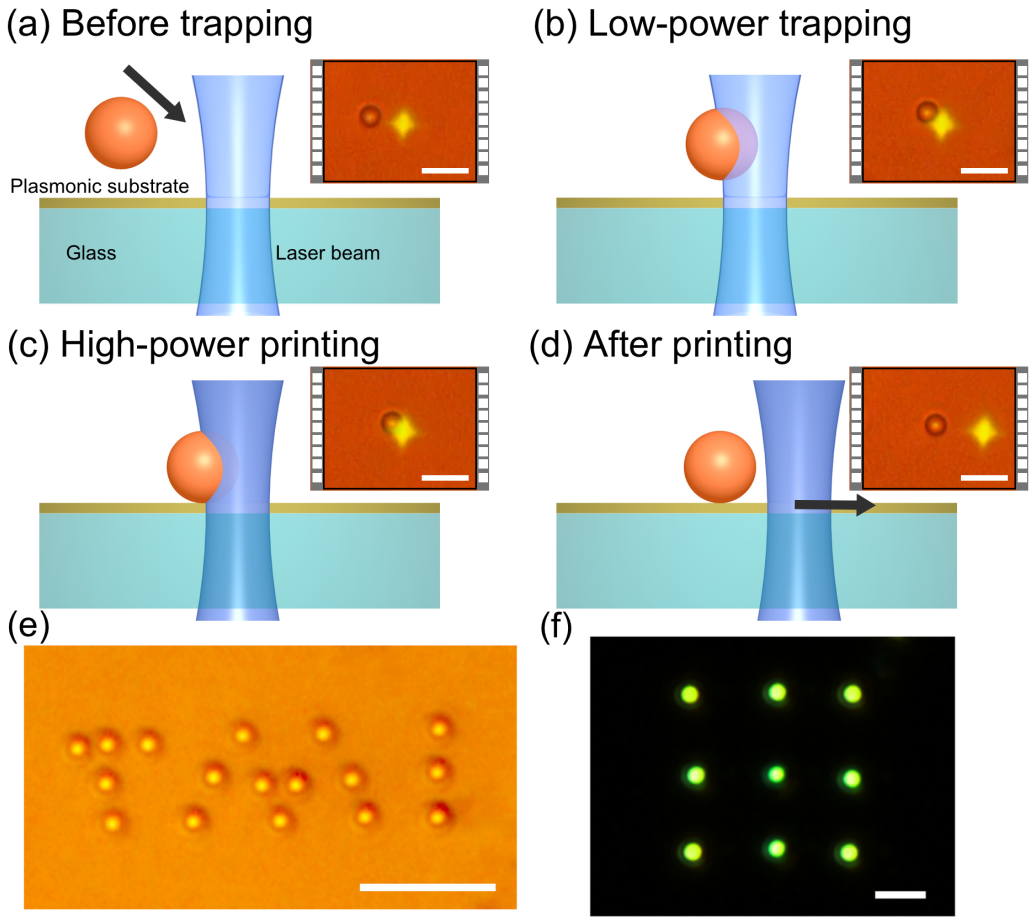

Figure 5.2: Opto-thermoelectric trapping and printing of colloidal particles. (a-d) Trapping and printing of a single 2 μm PS sphere by a single laser beam: (a) the sphere transport toward the laser beam, (b) trapping of the sphere at the laser beam with a low optical power, (c) printing of the trapped sphere at an increased optical power, (d) the printed sphere stayed at the original site on the substrate when the laser beam was moved away. Insets are optical images of the PS sphere and the laser beam spot at the different states. Scale bars: 4 μm. (e) A bright-field optical image of printed "TMI" pattern of 1 μm PS spheres on the substrate. Scale bar: 10 μm. (f) A dark-field optical image of printed 3-by-3 array of 500 nm PS spheres on the substrate after being dried. Scale bar: 5 μm.

Figs. 5.2a-d show schematics and experimental demonstration of the opto-thermoelectric trapping and printing of a single PS sphere with a diameter of 2 μm. Upon irradiation of the laser beam at a power of 0.72 mW/μm^2 on the substrate, a PS sphere

moved towards the laser beam (Fig. 5.2a) and was trapped at the edge of the laser beam (Fig. 5.2b). The trapped PS sphere can be transported to any targeted location by controlling the motorized stage of the optical microscope or steering the laser beam with a digital micromirror device. By simply increasing the laser power to 1.20 mW/μm^2, we printed the trapped PS sphere onto the substrate (Fig. 5.2c). The printed sphere would stay at the original site on the substrate when the laser beam was moved away (Fig. 5.2d).

The OTP is versatile in printing colloidal particles onto the substrate to form various patterns. For example, we printed seventeen 1 μm PS spheres into a "TMI" pattern (Fig. 5.2e) and nine 500 nm PS spheres into a 3×3 array (Fig. 5.2f) by directing the laser beam over the substrate. In the OTP, the bonding between the printed spheres and the substrate is quite strong. As shown in Fig. 5.2f, the printed pattern remained after the substrate was rinsed and dried.

To elucidate the working principle of the OTP, we have integrated experiments and theoretical analyses to understand both the trapping and printing mechanisms. As illustrated in Fig. 5.3a, a balance of the opto-thermoelectric repulsive force F_r (from a localized electrostatic field) and the opto-thermoelectric trapping force F_t (from a macroscopic electric field) on the PS sphere leads to its trapping at the edge of the laser beam and near the substrate-solution interface. In the following, we fully explain the particle-trapping mechanism by analyzing three major processes.

(I) The laser beam focused at the substrate-solution interface creates a well-defined temperature gradient (with the hottest region at the laser beam center and the substrate surface) due to the plasmon-enhanced opto-thermal effect. Both Na^+ and Cl^- ions in the mixed solution migrate from the hot to the cold region due to the thermophoresis effect. The different Soret coefficients of the ions, *i.e.*, $S_T(Na^+) > S_T(Cl^-)$, lead to accumulation of Na^+ and Cl^- ions in the cold and the hot region, respectively.[15] Thus, a macroscopic

electric field pointing from the cold to the hot region is established, which can trap positively charged particles at the laser beam with the opto-thermoelectric trapping force F_t.

(II) Since the as-purchased PS spheres in deionized (DI) water were negatively charged, we added cationic surfactant (*i.e.*, CTAC) to obtain the positively charged PS spheres due to the formation of CTAC double layers on the sphere surfaces. The positively charged PS sphere experiences a temperature-dependent electrostatic potential $-\frac{\nabla T}{T}\psi_0$ (ψ_0 is -16 mV for NaCl electrolytes) and migrates with a thermal diffusion velocity $\boldsymbol{u} = -\tau\frac{\varepsilon\zeta^{\mathrm{PS}}\psi_0}{\eta T}\nabla T$ to the hot region, where τ is the scaling factor considering the spatially varying temperature gradients, ζ^{PS} is the surface potential of the PS spheres, ε is the dielectric constant of the solvent, and η is the viscosity of the solvent.[9] $\frac{\varepsilon\zeta^{\mathrm{PS}}}{\eta}$ is the Helmholtz-Smoluchowski electrophoretic mobility from which the thermal diffusion coefficient is calculated as $D_{\mathrm{T}}^{\mathrm{EL}}(\mathrm{PS}) = \tau\frac{\varepsilon\zeta^{\mathrm{PS}}\psi_0}{\eta T}$.

(III) Meanwhile, the CTAC molecules above its critical micelle concentration (c_{cmc}=0.13 mM) also self-assemble into positively charged micelles. Under the macroscopic electric field, the CTAC micelles migrate from the cold to the hot region.[218] The Soret coefficient of the CTAC micelles is written as,[17]

$$S_{\mathrm{T\ (micelle)}} = -\frac{k_{\mathrm{B}}T\mu_{\mathrm{micelle}}}{e\,D_{\mathrm{micelle}}}\frac{\left(S_{\mathrm{T}}\,(\mathrm{Na}^+) - S_{\mathrm{T}}\,(\mathrm{Cl}^-)\right)}{2} \qquad (13)$$

where k_{B} is Boltzman constant, T is the temperature, e is the elementary charge, and μ_{micelle} and D_{micelle} are the electric mobility and mass diffusion coefficient of the micelles. The accumulation of the CTAC micelles at the hot region generates a localized electrostatic field pointing outwards the laser beam. Thus, an opto-thermoelectric repulsive force is exerted on the positively charged PS sphere. The repulsive force between a CTAC micelle and a charged PS sphere can be described by an electrostatic interaction potential[139]

$$U_{\mathrm{e}}^{\mathrm{dp}} = 4\pi\varepsilon\psi_{\mathrm{d}}\psi_{\mathrm{p}}\frac{r_{\mathrm{d}}r_{\mathrm{p}}}{r_{\mathrm{d}} + r_{\mathrm{p}} + r_{\mathrm{dp}}}\exp\left(-\kappa r_{\mathrm{dp}}\right) \tag{14}$$

where ε is the dielectric constant of the solvent, ψ_{d} and ψ_{p} are the surface potentials of the micelle and the sphere, r_{d} and r_{p} are the hard-sphere radii of the micelle and the sphere, r_{dp} is the distance between the micelle and the sphere, and κ is the inverse Debye length determined by the ionic strength. In our system, κ is mainly determined by the concentration of NaCl, which is at least 1 order of magnitude higher than the CTAC concentration. We neglect the influence of ionic strength on the hard-sphere radius of micelles since the NaCl concentration is still low (<0.1 M). The total opto-thermoelectric repulsive force F_{r} on the PS sphere due to an inhomogeneous distribution of the CTAC micelles can be estimated as

$$F_{\mathrm{r}} \propto c\left(\frac{\mathrm{d}c}{c}\right)\left(\frac{\mathrm{d}U_{\mathrm{e}}^{\mathrm{dp}}}{\mathrm{d}r_{\mathrm{dp}}}\right) \propto cS_{\mathrm{T\,(micelle)}}\nabla T\,\kappa\,\exp\left(-\kappa d_{\mathrm{dp}}\right) \tag{15}$$

where c is the average concentration of CTAC micelles that envelop the PS sphere. The balanced repulsive force F_{r} and trapping force F_{t} on the PS sphere lead to its stable trapping at the edge of the laser beam (Fig. 5.3a).

We have carried out a series of experiments to confirm the particle-trapping mechanism. Firstly, we did the parametric study on the sphere-trapping stability by measuring the escape velocity of a trapped PS sphere as a function of optical power and CTAC concentration. As shown in Fig. 5.3b, at a constant CTAC concentration, an increase of the optical power enhances the escape velocity and thus the trapping stability of the sphere. The enhanced trapping stability is consistent with our analysis of the repulsive force F_{r} and trapping force F_{t} on the PS sphere that are proportional to ∇T. However, one may expect a linear relation between the escape velocity and the optical power that is linearly proportional to ∇T. Instead, the increase rate of the escape velocity slows down at the

higher optical power. The deviation from a linear relation is attributed to thermoosmosis, which drives the PS sphere toward the cold region (*i.e.*, weakening the trapping).[219]

At a constant optical power, the escape velocity increases and then decreases when the CTAC concentration is increased (Fig. 5.3b), which is also consistent with our proposed trapping mechanism. Specifically, when the CTAC concentration was increased from 0.05 mM to 0.1 mM (which is below c_{cmc}), the density of positive surface charge on the PS sphere from the adsorbed CTAC surfactant was increased, enhancing the trapping force by the macroscopic electric field and thus the escape velocity. The surface charge density of the PS sphere was further increased when the CTAC concentration was continuously increased. Meanwhile, CTAC micelles formed when the CTAC concentration exceeded c_{cmc} (0.13 mM). The accumulated CTAC micelles at the hot region increased the repulsive force F_r on the positively charged PS sphere, reducing the escape velocity.

As summarized in a phase diagram in Fig. 5.3c, tuning NaCl concentration and optical power leads to various particle-manipulating regimes. At low NaCl concentrations (*i.e.*, <10 mM), the macroscopic electric field from the preferred accumulation of Na^+ and Cl^- ions in the cold and the hot region is weak. As a result, the trapping force F_t on the PS sphere is weaker than the opto-thermoelectric repulsive force F_r, which prevents the PS sphere from being trapped by the laser beam (known as "repelling" regime). At high NaCl concentrations (*i.e.*, >30 mM), the PS spheres in the solution sediment onto the substrate due to the small Debye screening length, which is known as "sedimentation" regime. The "trapping" regime occurs at moderate NaCl concentrations (*i.e.*, 10-30 mM) where, above the critical optical power,-the trapping force F_t on the PS sphere becomes stronger than the opto-thermoelectric repulsive force F_r to achieve the stable trapping of the sphere.

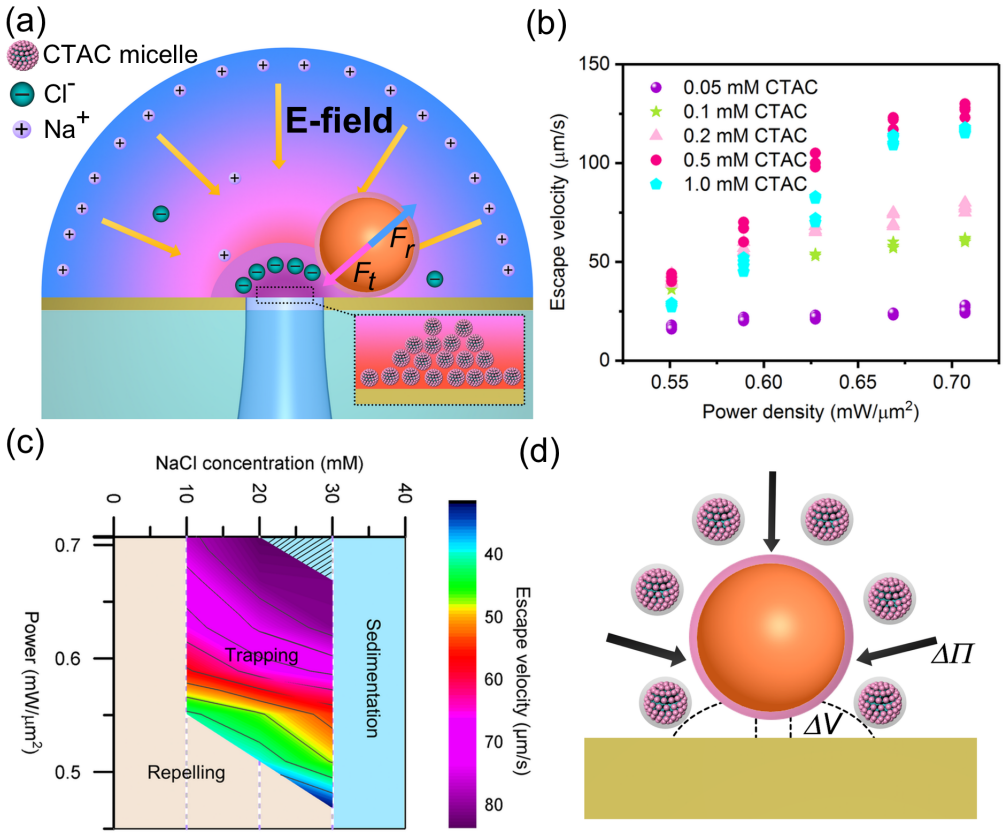

Figure 5.3: Working principle of the OTP. (a) Schematic illustration of the opto-thermoelectric trapping of a PS sphere at a balance between the thermoelectric trapping force F_t and the thermoelectric repulsive force F_r. Inset shows the accumulation of CTAC micelles at the hot region with the laser beam. (b) Escape velocity of a single trapped 2 μm PS sphere as a function of CTAC concentration and optical power. The NaCl concentration was fixed at 10 mM. (c) Phase diagram shows different particle-manipulation regimes at variable optical power and NaCl concentrations. The diagram is based on 2 μm PS spheres. The CTAC concentration was fixed at 0.2 mM. Colour bar in the trapping regime indicates that the escape velocity depends on the optical power and NaCl concentration. The printing regime is indicated by slash lines. (d) Schematic illustration of the micelle-mediated depletion attraction between the sphere and the substrate in the printing regime. ΔV is the depletion volume and $\Delta\Pi$ is the osmotic pressure difference between the bulk region and the depletion region.

More interestingly, the printing of the trapped PS spheres onto the substrate can be achieved by simply increasing the optical power, as indicated by "printing" regime in Fig.

5.3c. An increased optical power reduced the gap between the trapped particle and the substrate, leading to the entropy-driven depletion of the CTAC micelles at the particle-substrate interface and the formation of strong depletion attraction between the particle and the substrate. The depletion attraction acts as the binding force between the particle and the substrate in the OTP. As shown in Fig. 5.3d, an osmotic-pressure imbalance between the depletion region and the bulk region generates a pinning force to fix the particle on the substrate. The depletion attraction potential is described as $U_d = -\Delta V \Delta \Pi$, where ΔV is the depletion volume and $\Delta \Pi$ is the osmotic-pressure difference. When the laser is turned off, the depletion attraction can still overcome the electrostatic repulsive force to maintain the bonding between the particle and the substrate. By combing the optical trapping and on-demand printing, we can create arbitrary patterns of colloidal particles on the substrates.

Finally, we have achieved releasing of the printed particles from the substrate and reprint them at new sites on the substrate. The releasing and reprinting capabilities lead to a new concept of reconfigurable printing. As illustrated in Fig. 5.4a, by turning back on the laser and centering the laser beam to the printed particle, we can drive the accumulation of the CTAC micelles within the particle-substrate gap. The micelles in the gap weakens the depletion attraction between the particle and the substrate. Meanwhile, the repulsive electrostatic force F_r on the particle becomes stronger due to the accumulated micelles in the gap, eventually breaking the particle-substrate bonding and repelling the particle into the bulk solution Fig. 5.4b. In contrast to the depletion attraction, van der Walls forces that were applied to bind particles to substrates prevented the releasing of the particles.[220]

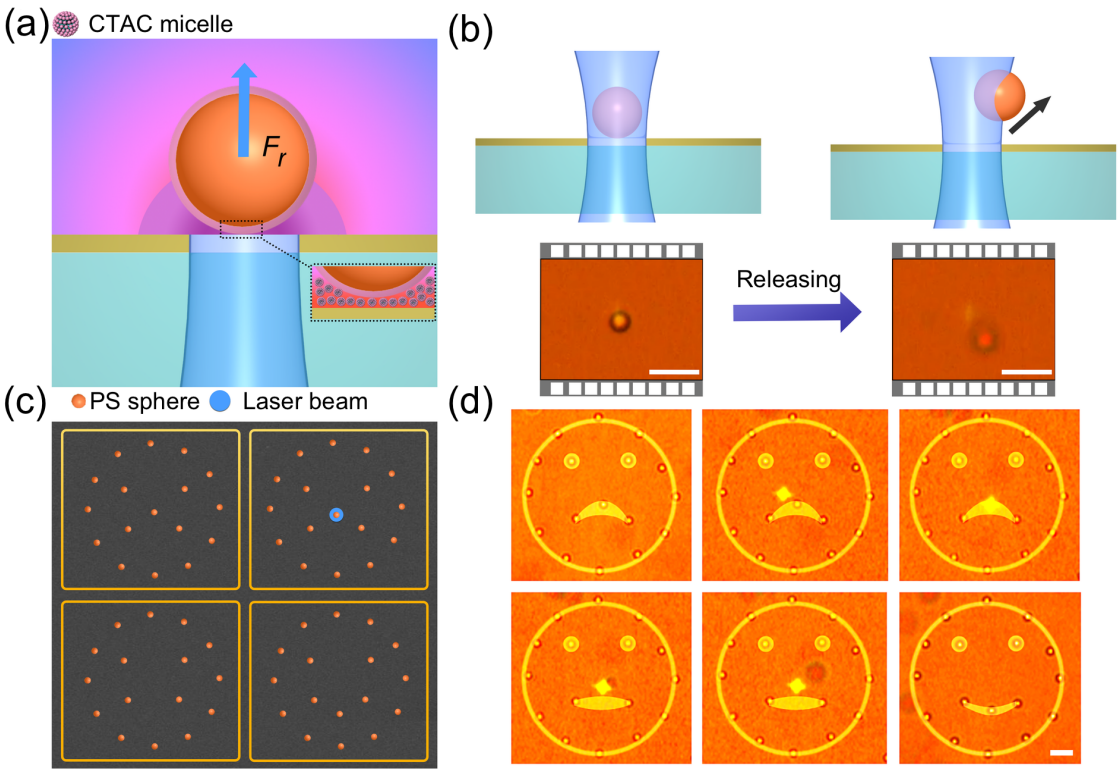

Figure 5.4: Releasing and reprinting of colloidal particles for the reconfigurable OTP. (a) Schematic illustration of the principle for releasing a printed particle from the substrate. Inset shows the accumulation of CTAC micelles in the gap between the particle and the substrate. (b) Schematics and optical images of the releasing of a 2 μm PS sphere that was previously printed on the substrate. Scale bars: 5 μm. (c) Schematics and (d) optical images of the reconfigurable printing of a "sad"-face pattern into a "smile"-face pattern consisted of 2 μm PS spheres. The transformation is done by releasing one of the spheres (as indicated by a blue circle in top-right frame of Fig. 5.4(c)) and re-printing it at a new site on the substrate. The yellow marks in (d) are added for a better visualization. The diamond-shaped spots in (d) are laser beams. Scale bar: 5 μm.

We have further demonstrated the reconfigurable printing, as shown in Figs. 5.4c-d. We initially printed multiple 2 μm PS spheres into a "sad"-face pattern. By controlling the laser beam to selectively release one of the printed spheres and to re-print it at a new site on the substrate, we transformed the "sad"-face pattern into a "smile"-face pattern.

In summary, we have developed an OTP technique to print patterns of colloidal particles on the substrates. By controlling macroscopic and localized opto-thermoelectric fields, we can optically trap and print colloidal particles. The bonding between the particles and substrates can be broken optically to release the particles, enabling reconfigurable printing. With its versatile low-power operation, the OTP will find applications in colloidal science and nanofabrication.

5.2 OPTO-THERMOELECTRIC PRINTING OF COLLOIDAL SUPERSTRUCTURES IN HYDROGEL SOLUTIONS[8]

Precise patterning of micro- and nano-structures with complex geometries and configurations is essential for fabrication of functional materials and devices.[221-223] Bottom-up assembly techniques through immobilization and patterning of colloidal particles with precise control of location, spacing, and orientation are particularly promising for the development of functional materials and devices.[224-227] First, colloidal particles as building blocks exhibit precisely tailorable properties down to atomic scale.[228] Second, high-quality crystallinity of colloidal particles from chemical synthesis is retained in the assembly process.[229] Third, assembly of colloidal particles into colloidal matter with precise geometric control will induce collective behaviors beyond what occurs in individual particles.[230, 231]

A wide range of techniques have been used to build colloidal superstructures and materials. As a widely applied technique, self-assembly autonomously builds colloidal particles into patterns, which is however often limited to thermodynamically stable colloidal structures.[232] DNA-guided assembly has also been extensively explored to

[8] Section 5.2 was published in the journal: **X. Peng***, J. Li*, L. Lin*, Y. Liu, and Y. Zheng, Opto-Thermophoretic Manipulation and Construction of Colloidal Superstructures in Photocurable Hydrogels, *ACS Appl. Nano Mater.*, 2018, **1**, 3998-4004. I am a leading author

construct programmable particle superlattices, periodic arrays, and asymmetric clusters.[233-236] In particular, the DNA origami technique can create plasmonic nanostructures with precise geometry and position, which can be used for enhanced Raman spectroscopy[237, 238] and tunable chiral structures.[239, 240]

Optical forces have been explored to pattern colloidal particles into arbitrary superstructures.[42, 109, 110, 164-166, 212, 241-244] One strategy is to trap and assemble particles into superstructures with optical tweezers and to immobilize the assembled superstructures through van der Waals forces[164, 166] or chemical linkages such as photopolymerization.[241, 243] Conventional optical tweezers require high power, which may cause irreversible photdamage to the colloidal particles.[174] Optical printing based on plasmon-enhanced optical radiation force is a low-power technique for precise patterning of plasmonic nanoparticles, however, plasmonic heating of already fixed nanoparticles prevents the assembly of particle dimers and clusters in near-field coupling regime.[42, 165, 212] To overcome this heating obstacle, Stefani's group proposed the use of laser beam that is off-resonance to the plasmon peak wavelength of the printed particles[165] or the use of substrates with high thermal conductivity.[244] Despite all the research efforts, the low-power and versatile optical assembly of colloidal superstructures still remains elusive.

Thermophoresis, which is directed migration of suspended particles under external temperature gradients, has been extensively studied for manipulation of colloidal particles.[15, 61, 64, 65, 69, 70, 219, 245, 246] Light-controlled thermophoresis has been judiciously harnessed for low-power optical manipulation of dielectric particles,[67, 68] plasmonic nanoparticles,[247] and biological cells.[77] However, most of opto-thermophoretic techniques have been limited to particle manipulation in aqueous solutions with relatively simple compositions. Immobilization of opto-thermophoretically assembled colloidal superstructures for device applications has remained challenging. Herein, we achieve low-

power opto-thermoelectric manipulation of colloidal particles in complex hydrogels and further demonstrate the all-optical construction of colloidal superstructures. Specifically, we exploit the micelle-mediated thermoelectric field and depletion attractive force in a light-controlled temperature field for versatile manipulation and assembly of colloidal particles in photocurable hydrogels. Furthermore, through UV-induced photopolymerization of the hydrogels, we successfully immobilize the assembled colloidal superstructures *via* the polymer joint. With the low operation power, versatile control, and *in-situ* polymerization-based bonding, our opto-thermoelectric manipulation in hydrogels will find applications in colloidal devices and materials science.

Figs. 5.5a-b illustrate the working principle of opto-thermoelectric trapping and patterning of a colloidal particle in a photocurable hydrogel. The colloidal particle is suspended in a mixture of cetyltrimethylammonium chloride (CTAC) molecules and photocurable hydrogel, which is sandwiched between a thermoplasmonic substrate and a glass cover slide. Above its critical micelle concentration (c_{cmc}: 0.13-0.16 mM), the cationic CTAC surfactant molecules self-assemble into positively charged micelles with a mean radius of 3 nm. CTAC molecules also adsorb on the colloidal particle surface through electrostatic and hydrophobic interactions, leading to a positively charged particle. The hydrogel consists of 10% poly(ethylene glycol) diacrylate (PEGD) 3400 polymers as the cross-linking reagent and 0.05% Irgacure 2959 as the photoinitiator. A temperature gradient is created by irradiating a laser beam onto the thermoplasmonic substrate consisting of a high density of Au nanoparticles, where the excitation of surface plasmons leads to high light-to-heat conversion efficiency. The difference in Soret coefficients between CTAC micelles (also known as macro ions) and Cl^- counter-ions causes the ionic separation. Thus, a localized thermoelectric field E_{T} is built to trap the positive particle, as shown in Fig. 5.5a. Once the particle is trapped and delivered to a target location,

ultraviolet (UV) light is applied to trigger the cross-linking reaction among dispersed PEGD chains and lock the particle onto the substrate, leading to the patterned or immobilized particle (Fig. 5.5b). A real-time process of trapping and patterning a 1 μm polystyrene (PS) bead is shown in Fig. 5.5c. The optical intensity for the opto-thermoelectric trapping ranges from 0.1 to 0.5 mW/μm^2, which is about 3 orders of magnitude lower than that of optical tweezers.[243, 248] With a typical power intensity of 0.2 mW/μm^2, particles can be effectively delivered to the trapping center within a surrounding region of 10 μm in radius.[247]

CTAC surfactant is critical to the low-power opto-thermoelectric manipulation. Meanwhile, the PEGD polymers, the main constituents of the hydrogels, also undergo thermophoresis, which may affect the migration behaviors of colloidal particles in the hydrogel solution. It has been reported that depletion of polymers can lead to accumulation of colloidal particles at the thermal hot spot in colloid-polymer mixtures.[18] To evaluate the contributions of the PEGD polymers and CTAC micelles to the trapping of colloidal particles, we studied the trapping kinetics of a single 500 nm PS sphere under a light-controlled temperature field in a pure hydrogel solution (Figs. 5.6a-b) and a hydrogel solution of 10 mM CTAC (Figs. 5.6c-d), respectively. Both solutions were confined in a 20 μm thin chamber to suppress the thermal convection and to rule out the thermofluidic effect on the colloidal dynamics.[249] The real-time trajectories of colloidal particles under the temperature field were recorded with a fast CCD camera. Under a temperature gradient ∇T with a magnitude of ~ 10 K/μm,[247] the 500 nm PS bead in the pure hydrogel solution underwent Brownian motion without significant confinement by the laser spot, as shown in Fig. 5.6b. It implies the depletion force arising from the 10% PEGD polymers was too weak to overcome the Brownian motion of the particle for its stable trapping.

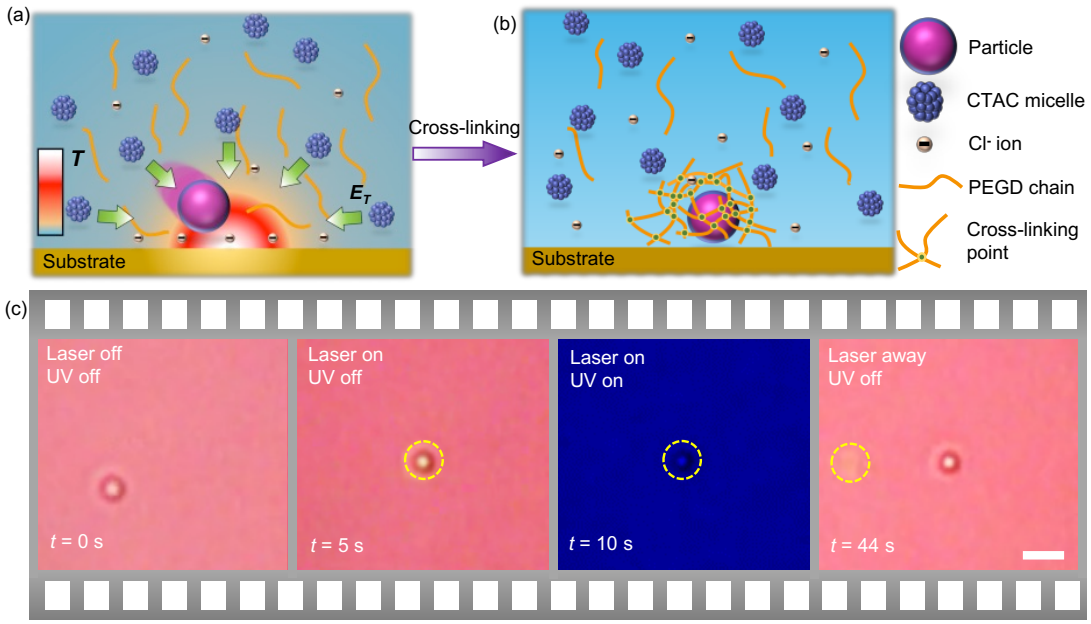

Figure 5.5: Opto-thermoelectric trapping and patterning of a colloidal particle in a hydrogel solution. (a) Schematic illustration of trapping of a colloidal particle in a thermoelectric field induced by the thermophoretic separation of dispersed CTAC micelles and Cl^- ions. (b) Schematic illustration of immobilization and patterning of the trapped colloidal particle through UV cross-linking. (c) Sequential optical images of trapping and patterning of a 1 μm PS sphere in a hydrogel solution with 20 mM CTAC. The thermoplasmonic substrate in (a-b) represents a quasicontinuous film consisting of a high density of Au nanoparticles. A 532 nm laser beam with a diameter of 2 μm and an optical intensity of 0.3 mW/μm^2 was used for opto-thermoelectric trapping. The laser beam is indicated by dashed circles in (c). Scale bar in (c): 2 μm.

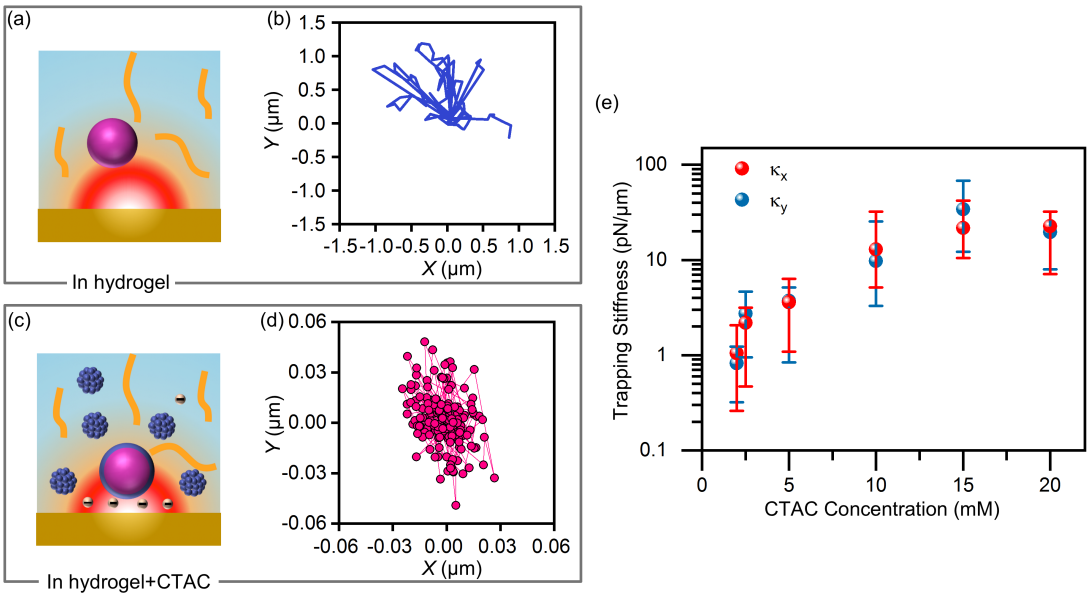

Figure 5.6: Effect of CTAC concentration on opto-thermoelectric trapping of colloidal particles. (a) Schematic illustration and (b) time trace of a 500 nm PS sphere under an optically controlled temperature field in a pure hydrogel solution. (c) Schematic illustration and (d) time trace of a 500 nm PS sphere under an optically controlled temperature field in a hydrogel solution with 10 mM CTAC. (e) Trapping stiffness for 500 nm PS spheres as a function of CTAC concentration. κ_x and κ_y are the trapping stiffness in the x and y directions, respectively. The error bars represent the deviation in five measurements with different particles. A (a-d) 20 μm and (e) 120 μm thick spacer were used to confine the solutions between a Au substrate and a coverslip, respectively. A 660 nm laser beam with a diameter of 943 nm and an optical power of 0.23 mW was irradiated onto the Au substrate

In contrast, the PS bead was stably trapped in the hydrogel solution with 10 mM CTAC, as shown in Fig. 5.6d. It should be noted that the temperature gradient ∇T is barely changed when introducing the CTAC into the hydrogel solution, for ∇T is determined by the heat transfer between the Au substrate and the hydrogel solution. Under the temperature gradient ∇T (~ 10 K/μm), both the CTAC micelles and Cl^- ions migrate from the hot to cold region with a drift velocity given by $\boldsymbol{u} = -D_T \nabla T$, where D_T is the thermophoretic

mobility. When it comes to steady state, a concentration gradient forms in the temperature field, *i.e.* $\nabla c = -S_{\mathrm{T}} c \nabla T$, where c is the micelle or ion concentration, and $S_{\mathrm{T}} = D_{\mathrm{T}}/D$ (D is the diffusion coefficient) is the corresponding Soret coefficient. Due to a much larger Soret coefficient of the CTAC micelles (~10^{-2} K^{-1}) than that of the Cl^- ions (~7.18×10^{-4} K^{-1}), the spatially redistributed CTAC micelles and Cl^- ions generate the thermoelectric field E_{T} that directs the positively charged PS beads along the temperature gradient, *i.e.* from the cold to hot region. Trapping of the beads is achieved at the laser spot with the balanced thermoelectric force and repulsive electrostatic force from the substrate. The substrate is also positively charged due to the coating of CTAC double layers.[179] To estimate the trapping stability, we conducted Gaussian fitting for the histogram of the particle displacements, which gives a variance σ of ~ 15 nm in both the *x* and *y* directions, corresponding to a trapping stiffness κ of ~ 37 pN/μm ($\kappa = \frac{2k_{\mathrm{B}}T}{\sigma^2}$). To generate the same trapping stiffness for a 500 nm PS sphere, optical tweezers typically require a power of ~100 mW,[243, 248] which is 3 orders of magnitude higher than the working power (0.23 mW) of our opto-thermoelectric tweezers.

Besides the opto-thermoelectric field from the thermophoretic migration of CTAC micelles and Cl^- ions, the interaction between the CTAC surfactant and the PEGD polymers should also be considered for the trapping behaviors of colloidal particles. Specifically, the association or binding of the CTAC micelles to the PEGD polymers, which scales linearly with the polymer concentration,[250] can significantly screen the thermoelectric field and increase the critical CTAC concentration for efficient opto-thermoelectric trapping. In the 10% PEGD polymer solution, which is typically the lowest concentration for UV cross-linking, we obtained a minimum CTAC concentration of 2 mM for trapping, which is 1 order of magnitude higher than that in aqueous solutions without hydrogels. When the CTAC concentration increases from 2 to 20 mM, the association effect becomes saturated

and the amount of free-form CTAC micelles increases linearly. It should be noted that the thermophoresis of CTAC micelles also introduces a depletion force between the particle and the substrate, which improves the trapping stiffness at high CTAC concentration. To verify our hypothesis, we measured the trapping stiffness of single 500 nm PS beads as a function of CTAC concentration from 2 to 20 mM (Fig. 5.6e). The trapping stiffness increases rapidly with the CTAC concentration in the range of 2-10 mM because of the enhanced particle-substrate depletion attraction and becomes relatively constant in the range of 10-20 mM. The trapping stiffness at 20 mM CTAC is improved by 1 order of magnitude because of the dominant depletion force.[247]

It is essential for a fabrication technique to pattern colloidal particles of various sizes and compositions while retaining their intrinsic physical properties. We have further integrated a high-performance spectrometer into our tweezers to carry out *in-situ* dark-field optical spectroscopy of the patterned particles, which include high-refractive-index silicon nanospheres (SiNSs) and plasmonic gold nanospheres (AuNSs). Fig. 5.7a shows the scattering spectra of a single 300 nm SiNS trapped in the hydrogel near the substrate (blue curve) and patterned onto the substrate after UV-induced cross-linking of the hydrogel (red curve). Two scattering peaks emerge at 675 and 765 nm, which correspond to the electric quadrupole and magnetic quadrupole due to Mie resonance of the SiNS, respectively.[251] No obvious change in the spectra of a 300 nm SiNS (Fig. 5.7a) and a 500 nm SiNS after the patterning indicates the cross-linking process does not change the surroundings' refractive index or the particles themselves. We have further demonstrated the patterning of 100 nm AuNS dimers that support the near-field coupling. As shown in Fig. 5.7b, the scattering peak (580 ± 10 nm) of a single AuNS splits into two peaks when two AuNSs are trapped and patterned in a hydrogel solution of 20 mM CTAC. Our finite-difference time-domain (FDTD) simulation reveals that the two peaks correspond to a longitudinal

mode (636 nm) and a transverse mode (570 nm) of the coupled AuNS dimer with a gap of ~30 nm. Repeated measurements of various AuNS dimers show that the longitudinal mode spans the range of 636 $\pm$ 10 nm, which represents a gap distance of 25-50 nm. The capability of patterning nanoparticles at the near-field coupling distance enables the construction of complex architectures with emerging properties.

We have applied the opto-thermoelectric manipulation and patterning to build diverse colloidal superstructures with colloidal particles of various sizes, dimensions and compositions. The interparticle depletion attraction interaction acts as the major "bonding" force to assemble the superstructures in hydrogels,[68] which are further immobilized *via* photopolymerization. Figs. 5.8a-c show two-dimensional (2D) close-packed colloidal superstructures of 1 μm, 2 μm, and 5 μm PS spheres, respectively. It is worth noting that the as-built superstructures remained intact even after the samples were rinsed and dried. The scanning electron micrograph in Fig. 5.8c shows the superstructure was joined by photocured hydrogels. Fig. 5.8d shows a one-dimensional (1D) chain of 2 μm PS spheres. Fig. 5.8e shows a 2D Saturn-ring structure consisting of a 5 μm PS sphere surrounded by eight 2 μm PS spheres. By further incorporating optical scattering force into the opto-thermoelectric system, we achieve out-of-plane manipulation to build three-dimensional (3D) superstructures. As an example, we show a 3D tetrahedron superstructure with four 2 μm PS spheres (Fig. 5.8f). To demonstrate the capability of building hybrid colloidal superstructures with particles of different compositions and sizes, we manage to arrange two 5 μm PS spheres and two 2 μm silica particles into two types of configurations (Figs. 5.8g-h). Figs. 5.8i-j show that three PS spheres with different sizes are arranged into left-handed or right-handed chiral configurations.

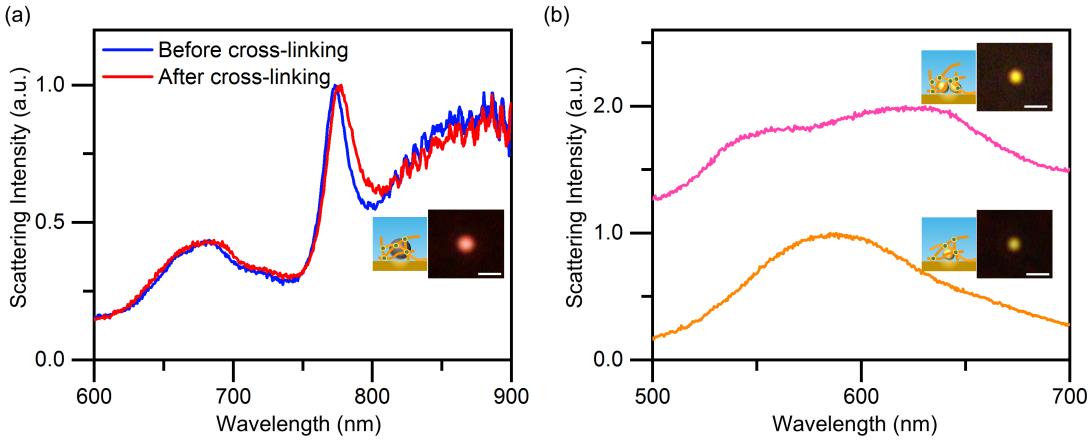

Figure 5.7: Optical spectroscopy of trapped and patterned nanoparticles in hydrogel solutions. (a) Dark-field scattering spectra of a 300 nm SiNS before and after cross-linking. (b) Dark-field scattering spectra of a single AuNS (bottom) and two AuNSs as a dimer (top) after cross-linking. The insets show the schematic illustrations and dark-field optical images for each curve after cross-linking. A 532 nm laser beam with a diameter of ~ 520 nm and a power intensity of 0.2 mW/μm^2 was used to trap the particles in a hydrogel solution of 20 mM CTAC. Scale bars in the insets of (a-b): 1 μm.

Exploiting micelle-mediated opto-thermoelectric fields for colloidal manipulation in hydrogels and UV-induced photopolymerization of the hydrogels, we have developed an opto-thermoelectric printing technique for versatile assembly of colloidal particles onto solid-state substrates. It is revealed that thermophoresis of the CTAC micelles, particle-substrate and particle-particle depletion attraction, and the micelle-polymer bonding contribute to the opto-thermoelectric trapping. The trapping efficiency can be optimized by tuning the CTAC concentration and a trapping stiffness of tens of pN/μm can be achieved for submicron colloidal particles. Using colloidal particles in a wide range of sizes and compositions as the building blocks, we demonstrate the assembly of complex colloidal superstructures with diverse configurations. Integrating *in-situ* spectroscopic analysis into the opto-thermoelectric system, we can study the responses of colloidal

superstructures to light fields. With its versatile, low-power, and noninvasive operation, the opto-thermoelectric patterning strategy will find applications in studies of light-matter interactions and nanofabrication of colloidal devices.

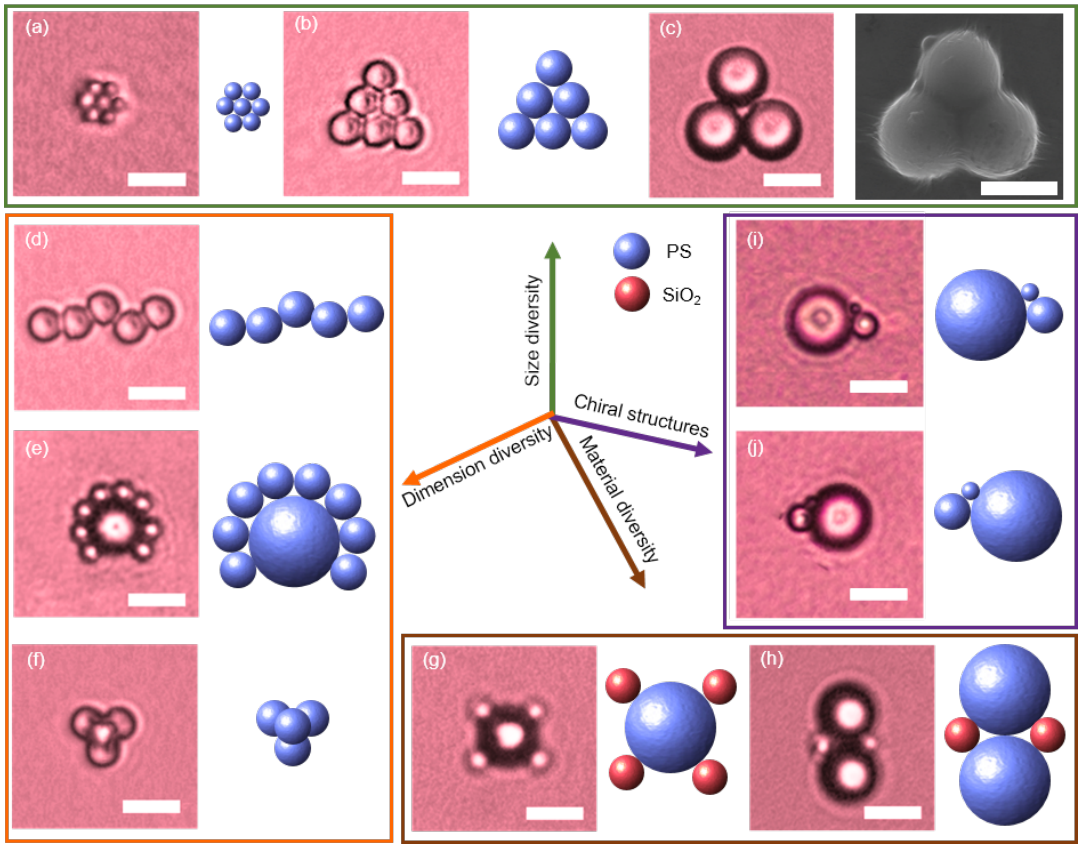

Figure 5.8: Opto-thermoelectric assembly and immobilization of various colloidal superstructures in hydrogel solutions. Assembly of (a) 1 μm, (b) 2 μm, and (c) 5 μm PS spheres into 2D close-packed superstructures. (d) 1D assembly of 2 μm PS spheres. (e) 2D hybrid assembly of a Saturn-ring superstructure with a 5 μm PS sphere and eight 2 μm PS spheres. (f) 3D assembly of a close-packed tetrahedron superstructure with four 2 μm PS spheres. (g) 2D hybrid assembly of a 5 μm PS sphere surrounded with four 2 μm silica spheres. (h) 2D hybrid assembly of two 5 μm PS spheres and two 2 μm silica spheres. (i-j) 2D hybrid assembly of a 1 μm, 2 μm, and 5 μm PS sphere into two close-packed superstructures with an opposite chirality. The pink images are the corresponding optical microscopy images. The inset in (c) shows the scanning electron micrograph of the corresponding superstructure after cross-linking of the hydrogel. All the colloidal superstructures were assembled in hydrogel solutions of 20 mM CTAC and patterned *via* UV-induced cross-linking. For assembly, 20 mM is an optimized concentration for strong depletion attraction between the assembled particles. A 532 nm laser beam with a diameter of 2 μm was used for assembly. Scale bars: 5 μm.

Chapter 6: Conclusion and Perspective[9]

Optothermal manipulation techniques, which exploit photon-phonon conversion and heat-directed migration, provide versatile control of diverse species such as colloidal particles, micelles, molecules, and living cells. Various approaches for optothermal manipulation of colloidal particles and living cells have been demonstrated through a combination of Marangoni convection, thermophoresis, thermoelectricity, and depletion attraction. In contrast to conventional optical tweezers, which often rely on optical gradient force generated with rigorous optics and a high-power laser, optothermal manipulation techniques use low-power and simple optics.

Optimization of light-controlled temperature gradients is the key to optothermal manipulation. Future development of this field relies on the rational management of optical heating. Specifically, any substrate with a high optothermal conversion efficiency and a low thermal conductivity is highly desired to improve the optothermal manipulation efficiency and to reduce optical power for noninvasive manipulation. There is also much room for optimization of the heating optics. For example, use of a femtosecond laser pulse for optical heating could limit both heat transfer and collective heating on the substrates, improving the temperature gradient for optothermal trapping.

The functionality of optothermal manipulation can be extended by multiple-field coupling. We have shown that coupling of light, temperature, and electric fields enables optothermoelectric manipulation. We expect that incorporation of a magnetic field into a light-controlled temperature field will enable opto-thermomagnetic manipulation. Examples include optical heating of ferromagnetic particles to around their Curie point, at

[9] Chapter 6 was published in the journal: L. Lin, E. H. Hill, **X. Peng**, and Y. Zheng, Optothermal Manipulations of Colloidal Particles and Living Cells, *Acc. Chem. Res.*, 2018, 51, 1465-1474. I am a co-author of this review paper.

which ferromagnetic materials lose their permanent magnetic properties. In addition, design of complex particles such as Janus particles with regions of different optical, thermal, electric, or magnetic responses could provide new manipulation scenarios and functionalities.

One of the most promising applications of optothermal manipulation is the assembly of functional colloidal materials and devices. Practical applications of colloidal materials and devices depend on the development of scalable and versatile assembly techniques. Through versatile control of configurations and interparticle interactions, optothermal manipulation techniques enable a wide range of functional colloidal devices such as colloidal waveguides, tunable lasers, and sensors.

Future use of optothermal techniques for noninvasive manipulation of biological objects will bring new revolutions in life sciences and early disease diagnostics. For example, the optothermal assembly of colloidal matter at single-particle resolution will provide a new platform for exploration of how matter organizes. Molecular manipulation across and inside living cells will also provide new insights into cellular drug delivery and intracellular biomolecular interactions. Recently, Reichl et al. demonstrated thermophoretic manipulation of molecules in living cells.[61] In contrast to electrophoresis where the electric field can be screened by the cell membrane and electrophoretic control can hardly function, opto-thermophoresis can be compatible with cellular environments. It should be noted that biological membranes significantly change across species and with environmental temperature and pH, providing both opportunities and challenges for optothermal manipulation of biological objects. In all cases, the temperature field should be carefully designed to avoid thermally induced biological damage.

We anticipate that with their low-power, noninvasive, and versatile manipulation of colloidal particles, living cells, and molecules, optothermal manipulation techniques will

not only accelerate progress in scientific research in colloidal science, life sciences, nanoscience, and materials sciences but also lead to new functional materials, nanomedicines, and diagnostic tools.

References

1. D. G. Grier, A Revolution in Optical Manipulation, *Nature*, 2003, **424**, 810-816.
2. L. Jauffred, A. C. Richardson and L. B. Oddershede, Three-Dimensional Optical Control of Individual Quantum Dots, *Nano Lett.*, 2008, **8**, 3376-3380.
3. P. M. Hansen, V. K. Bhatia, N. Harrit and L. Oddershede, Expanding the Optical Trapping Range of Gold Nanoparticles, *Nano Lett.*, 2005, **5**, 1937-1942.
4. A. Babynina, M. Fedoruk, P. Kühler, A. Meledin, M. Döblinger and T. Lohmüller, Bending Gold Nanorods with Light, *Nano Lett.*, 2016, **16**, 6485-6490.
5. A. N. Grigorenko, N. W. Roberts, M. R. Dickinson and ZhangY, Nanometric Optical Tweezers Based on Nanostructured Substrates, *Nature Photon.*, 2008, **2**, 365-370.
6. Y. Zheng, J. Ryan, P. Hansen, Y.-T. Cheng, T.-J. Lu and L. Hesselink, Nano-Optical Conveyor Belt, Part II: Demonstration of Handoff Between Near-Field Optical Traps, *Nano Lett.*, 2014, **14**, 2971-2976.
7. P. Y. Chiou, A. T. Ohta and M. C. Wu, Massively Parallel Manipulation of Single Cells and Microparticles Using Optical Images, *Nature*, 2005, **436**, 370-372.
8. R. Piazza and A. Parola, Thermophoresis in Colloidal Suspensions, *J. Phys.: Condens. Matter*, 2008, **20**, 153102.
9. A. Würger, Thermal Non-Equilibrium Transport in Colloids, *Rep. Prog. Phys.*, 2010, **73**, 126601.
10. J. S. Donner, G. Baffou, D. McCloskey and R. Quidant, Plasmon-Assisted Optofluidics, *ACS Nano*, 2011, **5**, 5457-5462.
11. L. Helden, R. Eichhorn and C. Bechinger, Direct Measurement of Thermophoretic Forces, *Soft Matter*, 2015, **11**, 2379-2386.
12. S. A. Putnam, D. G. Cahill and G. C. L. Wong, Temperature Dependence of Thermodiffusion in Aqueous Suspensions of Charged Nanoparticles, *Langmuir*, 2007, **23**, 9221-9228.
13. M. Braibanti, D. Vigolo and R. Piazza, Does Thermophoretic Mobility Depend on Particle Size?, *Phys. Rev. Lett.*, 2008, **100**, 108303.
14. A. Würger, Transport in Charged Colloids Driven by Thermoelectricity, *Phys. Rev. Lett.*, 2008, **101**, 108302.
15. M. Reichl, M. Herzog, A. Götz and D. Braun, Why Charged Molecules Move Across a Temperature Gradient: The Role of Electric Fields, *Phys. Rev. Lett.*, 2014, **112**, 198101.
16. D. Braun and A. Libchaber, Trapping of DNA by Thermophoretic Depletion and Convection, *Phys. Rev. Lett.*, 2002, **89**, 188103.

17. S. Duhr and D. Braun, Why Molecules Move Along a Temperature Gradient, *Proc. Natl. Acad. Sci. U. S. A.*, 2006, **103**, 19678-19682.

18. H.-R. Jiang, H. Wada, N. Yoshinaga and M. Sano, Manipulation of Colloids by a Nonequilibrium Depletion Force in a Temperature Gradient, *Phys. Rev. Lett.*, 2009, **102**, 208301.

19. E. Flores-Flores, S. A. Torres-Hurtado, R. Páez, U. Ruiz, G. Beltrán-Pérez, S. L. Neale, J. C. Ramirez-San-Juan and R. Ramos-García, Trapping and Manipulation of Microparticles Using Laser-Induced Convection Currents and Photophoresis, *Biomedi. Opt. Express*, 2015, **6**, 4079-4087.

20. T. Ito and S. Okazaki, Pushing the Limits of Lithography, *Nature*, 2000, **406**, 1027-1031.

21. F. Huo, G. Zheng, X. Liao, L. R. Giam, J. Chai, X. Chen, W. Shim and C. A. Mirkin, Beam Pen Lithography, *Nature Nanotechnol.*, 2010, **5**, 637-640.

22. T. Ozel, G. R. Bourret and C. A. Mirkin, Coaxial Lithography, *Nature Nanotechnol.*, 2015, **10**, 319-324.

23. M. Geissler and Y. N. Xia, Patterning: Principles and Some New Developments, *Adv. Mater.*, 2004, **16**, 1249-1269.

24. M. Rycenga, C. M. Cobley, J. Zeng, W. Li, C. H. Moran, Q. Zhang, D. Qin and Y. Xia, Controlling the Synthesis and Assembly of Silver Nanostructures for Plasmonic Applications, *Chem. Rev.*, 2011, **111**, 3669-3712.

25. X. Wang, J. Zhuang, Q. Peng and Y. Li, A General Strategy for Nanocrystal Synthesis, *Nature*, 2005, **437**, 121-124.

26. B. Wiley, Y. Sun and Y. Xia, Synthesis of Silver Nanostructures with Controlled Shapes and Properties, *Acc. Chem. Res.*, 2007, **40**, 1067-1076.

27. Y. Xia, P. Yang, Y. Sun, Y. Wu, B. Mayers, B. Gates, Y. Yin, F. Kim and H. Yan, One-Dimensional Nanostructures: Synthesis, Characterization, and Applications, *Adv. Mater.*, 2003, **15**, 353-389.

28. M. Dahl, Y. Liu and Y. Yin, Composite Titanium Dioxide Nanomaterials, *Chem. Rev.*, 2014, **114**, 9853-9889.

29. E. Rabani, D. R. Reichman, P. L. Geissler and L. E. Brus, Drying-Mediated Self-Assembly of Nanoparticles, *Nature*, 2003, **426**, 271-274.

30. J. C. Hulteen, D. A. Treichel, M. T. Smith, M. L. Duval, T. R. Jensen and R. P. Van Duyne, Nanosphere Lithography: Size-Tunable Silver Nanoparticle and Surface Cluster Arrays, *J. Phys. Chem. B*, 1999, **103**, 3854-3863.

31. C. L. Haynes and R. P. Van Duyne, Nanosphere Lithography: A Versatile Nanofabrication Tool for Studies of Size-Dependent Nanoparticle Optics, *J. Phys. Chem. B*, 2001, **105**, 5599-5611.

32. Y. Lu, Y. Yin, Z.-Y. Li and Y. Xia, Synthesis and Self-Assembly of Au@SiO2 Core−Shell Colloids, *Nano Lett.*, 2002, **2**, 785-788.

33. Y. Xia, Y. Yin, Y. Lu and J. McLellan, Template-Assisted Self-Assembly of Spherical Colloids into Complex and Controllable Structures, *Adv. Funct. Mater.*, 2003, **13**, 907-918.

34. A. Tao, P. Sinsermsuksakul and P. Yang, Tunable Plasmonic Lattices of Silver Nanocrystals, *Nature Nanotechnol.*, 2007, **2**, 435-440.

35. R. D. Piner, J. Zhu, F. Xu, S. Hong and C. A. Mirkin, "Dip-Pen" Nanolithography, *Science*, 1999, **283**, 661-663.

36. K. Salaita, Y. Wang and C. A. Mirkin, Applications of Dip-Pen Nanolithography, *Nature Nanotechnol.*, 2007, **2**, 145-155.

37. F. Huo, Z. Zheng, G. Zheng, L. R. Giam, H. Zhang and C. A. Mirkin, Polymer Pen Lithography, *Science*, 2008, **321**, 1658-1660.

38. J.-H. Ahn, H.-S. Kim, K. J. Lee, S. Jeon, S. J. Kang, Y. Sun, R. G. Nuzzo and J. A. Rogers, Heterogeneous Three-Dimensional Electronics by Use of Printed Semiconductor Nanomaterials, *Science*, 2006, **314**, 1754-1757.

39. P. J. Pauzauskie, A. Radenovic, E. Trepagnier, H. Shroff, P. Yang and J. Liphardt, Optical Trapping and Integration of Semiconductor Nanowire Assemblies in Water, *Nature Mater.*, 2006, **5**, 97-101.

40. C. Selhuber-Unkel, I. Zins, O. Schubert, C. Sönnichsen and L. B. Oddershede, Quantitative Optical Trapping of Single Gold Nanorods, *Nano Lett.*, 2008, **8**, 2998-3003.

41. B. K. Wilson, M. Hegg, X. Miao, G. Cao and L. Y. Lin, Scalable Nano-Particle Assembly by Efficient Light-Induced Concentration and Fusion, *Opt. Express*, 2008, **16**, 17276-17281.

42. S. Nedev, A. S. Urban, A. A. Lutich and J. Feldmann, Optical Force Stamping Lithography, *Nano Lett.*, 2011, **11**, 5066-5070.

43. M. C. Wu, Optoelectronic Tweezers, *Nature Photon.*, 2011, **5**, 322-324.

44. K.-W. Huang, Y.-C. Wu, J.-A. Lee and P.-Y. Chiou, Microfluidic Integrated Optoelectronic Tweezers for Single-Cell Preparation and Analysis, *Lab Chip*, 2013, **13**, 3721-3727.

45. K.-W. Huang, T.-W. Su, A. Ozcan and P.-Y. Chiou, Optoelectronic Tweezers Integrated with Lensfree Holographic Microscopy for Wide-Field Interactive Cell and Particle Manipulation on a Chip, *Lab Chip*, 2013, **13**, 2278-2284.

46. A. Jamshidi, S. L. Neale, K. Yu, P. J. Pauzauskie, P. J. Schuck, J. K. Valley, H.-Y. Hsu, A. T. Ohta and M. C. Wu, NanoPen: Dynamic, Low-Power, and Light-Actuated Patterning of Nanoparticles, *Nano Lett.*, 2009, **9**, 2921-2925.

47. W. Hu, K. S. Ishii, Q. Fan and A. T. Ohta, Hydrogel Microrobots Actuated by Optically Generated Vapour Bubbles, *Lab Chip*, 2012, **12**, 3821-3826.

48. A. Hashmi, G. Yu, M. Reilly-Collette, G. Heiman and J. Xu, Oscillating Bubbles: A Versatile Tool for Lab on a Chip Applications, *Lab Chip*, 2012, **12**, 4216-4227.

49. C. Zhao, Y. Xie, Z. Mao, Y. Zhao, J. Rufo, S. Yang, F. Guo, J. D. Mai and T. J. Huang, Theory and Experiment on Particle Trapping and Manipulation *via* Optothermally Generated Bubbles, *Lab Chip*, 2014, **14**, 384-391.

50. Z. Fang, Y.-R. Zhen, O. Neumann, A. Polman, F. J. García de Abajo, P. Nordlander and N. J. Halas, Evolution of Light-Induced Vapor Generation at a Liquid-Immersed Metallic Nanoparticle, *Nano Lett.*, 2013, **13**, 1736-1742.

51. O. Neumann, A. S. Urban, J. Day, S. Lal, P. Nordlander and N. J. Halas, Solar Vapor Generation Enabled by Nanoparticles, *ACS Nano*, 2013, **7**, 42-49.

52. G. Baffou, J. Polleux, H. Rigneault and S. Monneret, Super-Heating and Micro-Bubble Generation around Plasmonic Nanoparticles under CW Illumination, *J. Phys. Chem. C*, 2014, **118**, 4890-4898.

53. S. Baral, A. J. Green, M. Y. Livshits, A. O. Govorov and H. H. Richardson, Comparison of Vapor Formation of Water at the Solid/Water Interface to Colloidal Solutions Using Optically Excited Gold Nanostructures, *ACS Nano*, 2014, **8**, 1439-1448.

54. H. K. Raut, S. S. Dinachali, Y. C. Loke, R. Ganesan, K. K. Ansah-Antwi, A. Góra, E. H. Khoo, V. A. Ganesh, M. S. M. Saifullah and S. Ramakrishna, Multiscale Ommatidial Arrays with Broadband and Omnidirectional Antireflection and Antifogging Properties by Sacrificial Layer Mediated Nanoimprinting, *ACS Nano*, 2015, **9**, 1305-1314.

55. D. Wu, J.-N. Wang, L.-G. Niu, X. L. Zhang, S. Z. Wu, Q.-D. Chen, L. P. Lee and H. B. Sun, Bioinspired Fabrication of High-Quality 3D Artificial Compound Eyes by Voxel-Modulation Femtosecond Laser Writing for Distortion-Free Wide-Field-of-View Imaging, *Adv. Opt. Mater.*, 2014, **2**, 751-758.

56. F. Serra, M. A. Gharbi, Y. Luo, I. B. Liu, N. D. Bade, R. D. Kamien, S. Yang and K. J. Stebe, Curvature-Driven, One-Step Assembly of Reconfigurable Smectic Liquid Crystal "Compound Eye" Lenses, *Adv. Opt. Mater.*, 2015, **3**, 1287-1292.

57. N. Liu, M. L. Tang, M. Hentschel, H. Giessen and A. P. Alivisatos, Nanoantenna-Enhanced Gas Sensing in a Single Tailored Nanofocus, *Nature Mater.*, 2011, **10**, 631-636.

58. D. K. Wood, D. M. Weingeist, S. N. Bhatia and B. P. Engelward, Engelward, Single Cell Trapping and DNA Damage Analysis Using Microwell Arrays, *Proc. Natl. Acad. Sci. U. S. A.*, 2010, **107**, 10008-10013.

59. R. Yan, J. R. Simpson, S. Bertolazzi, J. Brivio, M. Watson, X. Wu, A. Kis, T. Luo, A. R. Hight Walker and H. G. Xing, Thermal Conductivity of Monolayer Molybdenum Disulfide Obtained from Temperature-Dependent Raman Spectroscopy, *ACS Nano*, 2014, **8**, 986-993.

60. T. B. Hoang, G. M. Akselrod, C. Argyropoulos, J. Huang, D. R. Smith and M. H. Mikkelsen, Ultrafast Spontaneous Emission Source Using Plasmonic Nanoantennas, *Nature Commun.*, 2015, **6**.

61. M. R. Reichl and D. Braun, Thermophoretic Manipulation of Molecules inside Living Cells, *J. Am. Chem. Soc.*, 2014, **136**, 15955-15960.

62. M. Braun and F. Cichos, Optically Controlled Thermophoretic Trapping of Single Nano-Objects, *ACS Nano*, 2013, **7**, 11200-11208.

63. M. Braun, A. P. Bregulla, K. Günther, M. Mertig and F. Cichos, Single Molecules Trapped by Dynamic Inhomogeneous Temperature Fields, *Nano Lett.*, 2015, **15**, 5499-5505.

64. C. L. C. Smith, A. H. Thilsted, J. N. Pedersen, T. H. Youngman, J. C. Dyrnum, N. A. Michaelsen, R. Marie and A. Kristensen, Photothermal Transport of DNA in Entropy-Landscape Plasmonic Waveguides, *ACS Nano*, 2017, **11**, 4553-4563.

65. E. L. Talbot, J. Kotar, L. Parolini, L. Di Michele and P. Cicuta, Thermophoretic Migration of Vesicles Depends on Mean Temperature and Head Group Chemistry, *Nature Commun.*, 2017, **8**, 15351.

66. T. Fukuyama, A. Fuke, M. Mochizuki, K. Kamei and Y. T. Maeda, Directing and Boosting of Cell Migration by the Entropic Force Gradient in Polymer Solution, *Langmuir*, 2015, **31**, 12567-12572.

67. L. Lin, X. Peng, Z. Mao, X. Wei, C. Xie and Y. Zheng, Interfacial-Entropy-Driven Thermophoretic Tweezers, *Lab Chip*, 2017, **17**, 3061-3070.

68. L. Lin, J. Zhang, X. Peng, Z. Wu, A. C. H. Coughlan, Z. Mao, M. A. Bevan and Y. Zheng, Opto-Thermophoretic Assembly of Colloidal Matter, *Science Advances*, 2017, **3**.

69. Z. Kang, J. Chen, S.-Y. Wu, K. Chen, S.-K. Kong, K.-T. Yong and H.-P. Ho, Trapping and Assembling of Particles and Live Cells on Large-Scale Random Gold Nano-Island Substrates, *Scientific Reports*, 2015, **5**, 9978.

70. R. Piazza, Thermophoresis: Moving Particles with Thermal Gradients, *Soft Matter*, 2008, **4**, 1740-1744.

71. J. Morthomas and A. Wurger, Thermoelectric Effect on Charged Colloids in the Huckel Limit, *Eur. Phys. J. E*, 2008, **27**, 425-434.

72. A. Majee and A. Wurger, Thermocharge of a Hot Spot in an Electrolyte Solution, *Soft Matter*, 2013, **9**, 2145-2153.

73. K. A. Eslahian, A. Majee, M. Maskos and A. Wurger, Specific Salt Effects on Thermophoresis of Charged Colloids, *Soft Matter*, 2014, **10**, 1931-1936.

74. L. Aboubakry, M. Arghya and W. Alois, Nanoscale Seebeck Effect at Hot Metal Nanostructures, *New J. Phys.*, 2017.

75. S. A. Putnam and D. G. Cahill, Transport of Nanoscale Latex Spheres in a Temperature Gradient, *Langmuir*, 2005, **21**, 5317-5323.

76. S. Iacopini and R. Piazza, Thermophoresis in Protein Solutions, *EPL*, 2003, **63**, 247.

77. L. Lin, X. Peng, X. Wei, Z. Mao, C. Xie and Y. Zheng, Thermophoretic Tweezers for Low-Power and Versatile Manipulation of Biological Cells, *ACS Nano*, 2017, **11**, 3147-3154.

78. J. L. Anderson, Colloid Transport by Interfacial Forces, *Annu. Rev. Fluid Mech.*, 1989, **21**, 61-99.

79. J. O. M. Bockris, M. A. V. Devanathan and K. Muller, On the Structure of Charged Interfaces, *Proc. R. Soc. London, A*, 1963, **274**, 55-79.

80. S. J. Marrink, M. Berkowitz and H. J. C. Berendsen, Molecular Dynamics Simulation of a Membrane/Water Interface: The Ordering of Water and Its Relation to the Hydration Force, *Langmuir*, 1993, **9**, 3122-3131.

81. V. V. Turov and I. F. Mironyuk, Adsorption Layers of Water on the Surface of Hydrophilic, Hydrophobic and Mixed Silicas, *Colloids Surf., A*, 1998, **134**, 257-263.

82. C. Macias-Romero, I. Nahalka, H. I. Okur and S. Roke, Optical Imaging of Surface Chemistry and Dynamics in Confinement, *Science*, 2017, **357**, 784-788.

83. J. K. G. Dhont and W. J. Briels, Single-Particle Thermal Diffusion of Charged Colloids: Double-Layer Theory in a Temperature Gradient, *Eur. Phys. J. E*, 2008, **25**, 61-76.

84. A. P. Bregulla, A. Würger, K. Günther, M. Mertig and F. Cichos, Thermo-Osmotic Flow in Thin Films, *Phys. Rev. Lett.*, 2016, **116**, 188303.

85. N. V. Churaev, B. V. Derjaguin and V. M. Muller, *Surface Forces*, Springer Science & Business Media, 2013.

86. A. Würger, Hydrodynamic Boundary Effects on Thermophoresis of Confined Colloids, *Phys. Rev. Lett.*, 2016, **116**, 138302.

87. M. Han, Thermophoresis in Liquids: A Molecular Dynamics Simulation Study, *J. Colloid Interface Sci.*, 2005, **284**, 339-348.

88. T. Tetsuro, I. Hirotaka, H. Itsuo and K. Satoyuki, Negative Thermophoresis of Nanoparticles Interacting with Fluids through a Purely-Repulsive Potential, *J. Phys.: Condens. Matter*, 2017, **29**, 475101.

89. D. J. Bonthuis, S. Gekle and R. R. Netz, Dielectric Profile of Interfacial Water and Its Effect on Double-Layer Capacitance, *Phys. Rev. Lett.*, 2011, **107**, 166102.

90. J. J. Karnes, E. A. Gobrogge, R. A. Walker and I. Benjamin, Unusual Structure and Dynamics at Silica/Methanol and Silica/Ethanol Interfaces—a Molecular Dynamics and Nonlinear Optical Study, *J. Phys. Chem. B*, 2016, **120**, 1569-1578.

91. S. R. Raghavan, H. J. Walls and S. A. Khan, Rheology of Silica Dispersions in Organic Liquids: New Evidence for Solvation Forces Dictated by Hydrogen Bonding, *Langmuir*, 2000, **16**, 7920-7930.

92. E.-L. Florin, A. Pralle, E. H. K. Stelzer and J. K. H. Hörber, Photonic Force Microscope Calibration by Thermal Noise Analysis, *Appl. Phys. A*, 1998, **66**, S75-S78.

93. Y. Naruke, S. Kosaka, T. Nakano, G. Kikugawa and T. Ohara, A Molecular Dynamics Study on Mass Transport Characteristics in the Vicinity of SiO2–Water/IPA Interfaces, *Int. J. Heat Mass Transfer*, 2015, **84**, 584-591.

94. M. M. Wang, E. Tu, D. E. Raymond, J. M. Yang, H. Zhang, N. Hagen, B. Dees, E. M. Mercer, A. H. Forster, I. Kariv, P. J. Marchand and W. F. Butler, Microfluidic Sorting of Mammalian Cells by Optical Force Switching, *Nat. Biotechnol.*, 2005, **23**, 83-87.

95. M. C. Zhong, X. B. Wei, J. H. Zhou, Z. Q. Wang and Y. M. Li, Trapping Red Blood Cells in Living Animals Using Optical Tweezers, *Nature Commun.*, 2013, **4**, 1768.

96. Y. Pang, H. Song, J. H. Kim, X. Hou and W. Cheng, Optical Trapping of Individual Human Immunodeficiency Viruses in Culture Fluid Reveals Heterogeneity with Single-Molecule Resolution, *Nature Nanotechnol.*, 2014, **9**, 624-630.

97. M. Gu, H. Bao, X. Gan, N. Stokes and J. Wu, Tweezing and Manipulating Micro- and Nanoparticles by Optical Nonlinear Endoscopy, *Light Sci. Appl.*, 2014, **3**, e126.

98. C. H. Streuli, N. Bailey and M. J. Bissell, Control of Mammary Epithelial Differentiation: Basement Membrane Induces Tissue-Specific Gene Expression in the Absence of Cell-Cell Interaction and Morphological Polarity, *J. Cell Biol.*, 1991, **115**, 1383-1395.

99. B. N. Manz and J. T. Groves, Spatial Organization and Signal Transduction at Intercellular Junctions, *Nat. Rev. Mol. Cell Biol.*, 2010, **11**, 342-352.

100. L. Friedrich and A. Rohrbach, Surface Imaging Beyond the Diffraction Limit with Optically Trapped Spheres, *Nature Nanotechnol.*, 2015, **10**, 1064-1069.

101. Z. Yan, M. Sajjan and N. F. Scherer, Fabrication of a Material Assembly of Silver Nanoparticles Using the Phase Gradients of Optical Tweezers, *Phys. Rev. Lett.*, 2015, **114**, 143901.

102. A. S. Urban, A. A. Lutich, F. D. Stefani and J. Feldmann, Laser Printing Single Gold Nanoparticles, *Nano Lett.*, 2010, **10**, 4794-4798.

103. J. Gluckstad, Microfluidics: Sorting Particles with Light, *Nature Mater.*, 2004, **3**, 9-10.

104. V. Garces-Chavez, D. McGloin, H. Melville, W. Sibbett and K. Dholakia, Simultaneous Micromanipulation in Multiple Planes Using a Self-Reconstructing Light Beam, *Nature*, 2002, **419**, 145-147.

105. M. Righini, A. S. Zelenina, C. Girard and R. Quidant, Parallel and Selective Trapping in a Patterned Plasmonic Landscape, *Nature Phys.*, 2007, **3**, 477-480.

106. M. L. Juan, M. Righini and R. Quidant, Plasmon Nano-Optical Tweezers, *Nature Photon.*, 2011, **5**, 349-356.

107. J. Berthelot, S. S. Acimovic, M. L. Juan, M. P. Kreuzer, J. Renger and R. Quidant, Three-Dimensional Manipulation with Scanning Near-Field Optical Nanotweezers, *Nature Nanotechnol.*, 2014, **9**, 295-299.

108. Y. Xie, C. Zhao, Y. Zhao, S. Li, J. Rufo, S. Yang, F. Guo and T. J. Huang, Optoacoustic Tweezers: A Programmable, Localized Cell Concentrator Based on Opto-Thermally Generated, Acoustically Activated, Surface Bubbles, *Lab Chip*, 2013, **13**, 1772-1779.

109. J. C. Ndukaife, A. V. Kildishev, A. G. A. Nnanna, V. M. Shalaev, S. T. Wereley and A. Boltasseva, Long-Range and Rapid Transport of Individual Nano-Objects by a Hybrid Electrothermoplasmonic Nanotweezer, *Nature Nanotechnol.*, 2016, **11**, 53-59.

110. B. J. Roxworthy, K. D. Ko, A. Kumar, K. H. Fung, E. K. C. Chow, G. L. Liu, N. X. Fang and K. C. Toussaint, Jr., Application of Plasmonic Bowtie Nanoantenna Arrays for Optical Trapping, Stacking, and Sorting, *Nano Lett.*, 2012, **12**, 796-801.

111. F. M. Weinert and D. Braun, Observation of Slip Flow in Thermophoresis, *Phys. Rev. Lett.*, 2008, **101**, 168301.

112. L. H. Thamdrup, N. B. Larsen and A. Kristensen, Light-Induced Local Heating for Thermophoretic Manipulation of DNA in Polymer Micro- and Nanochannels, *Nano Lett.*, 2010, **10**, 826-832.

113. F. M. Weinert and D. Braun, An Optical Conveyor for Molecules, *Nano Lett.*, 2009, **9**, 4264-4267.

114. M. Braun, A. Wurger and F. Cichos, Trapping of Single Nano-Objects in Dynamic Temperature Fields, *Phys. Chem. Chem. Phys.*, 2014, **16**, 15207-15213.

115. J. Guck, R. Ananthakrishnan, H. Mahmood, T. J. Moon, C. C. Cunningham and J. Käs, The Optical Stretcher: A Novel Laser Tool to Micromanipulate Cells, *Biophys. J.*, 2001, **81**, 767-784.

116. M. K. Kreysing, T. Kießling, A. Fritsch, C. Dietrich, J. R. Guck and J. A. Käs, The Optical Cell Rotator, *Opt. Express*, 2008, **16**, 16984-16992.

117. F. Guo, P. Li, J. B. French, Z. Mao, H. Zhao, S. Li, N. Nama, J. R. Fick, S. J. Benkovic and T. J. Huang, Controlling Cell–Cell Interactions Using Surface Acoustic Waves, *Proc. Natl. Acad. Sci. U. S. A.*, 2015, **112**, 43-48.

118. D. Ahmed, A. Ozcelik, N. Bojanala, N. Nama, A. Upadhyay, Y. Chen, W. Hanna-Rose and T. J. Huang, Rotational Manipulation of Single Cells and Organisms Using Acoustic Waves, *Nature Commun.*, 2016, **7**.

119. A. Lehmuskero, P. Johansson, H. Rubinsztein-Dunlop, L. Tong and M. Käll, Laser Trapping of Colloidal Metal Nanoparticles, *ACS Nano*, 2015, **9**, 3453-3469.

120. Z. Li, W. Mao, M. S. Devadas and G. V. Hartland, Absorption Spectroscopy of Single Optically Trapped Gold Nanorods, *Nano Lett.*, 2015, **15**, 7731-7735.

121. L. Bosanac, T. Aabo, P. M. Bendix and L. B. Oddershede, Efficient Optical Trapping and Visualization of Silver Nanoparticles, *Nano Lett.*, 2008, **8**, 1486-1491.

122. M. Pelton, M. Liu, H. Y. Kim, G. Smith, P. Guyot-Sionnest and N. F. Scherer, Optical Trapping and Alignment of Single Gold Nanorods by Using Plasmon Resonances, *Opt. Lett.*, 2006, **31**, 2075-2077.

123. P. M. Bendix, L. Jauffred, K. Norregaard and L. B. Oddershede, Optical Trapping of Nanoparticles and Quantum Dots, *IEEE J. Sel. Top. Quantum Electron.*, 2014, **20**, 15-26.

124. P. V. Ruijgrok, N. R. Verhart, P. Zijlstra, A. L. Tchebotareva and M. Orrit, Brownian Fluctuations and Heating of an Optically Aligned Gold Nanorod, *Phys. Rev. Lett.*, 2011, **107**, 037401.

125. L. Shao, Z.-J. Yang, D. Andrén, P. Johansson and M. Käll, Gold Nanorod Rotary Motors Driven by Resonant Light Scattering, *ACS Nano*, 2015, **9**, 12542-12551.

126. C. Min, Z. Shen, J. Shen, Y. Zhang, H. Fang, G. Yuan, L. Du, S. Zhu, T. Lei and X. Yuan, Focused Plasmonic Trapping of Metallic Particles, *Nat Commun*, 2013, **4**.

127. A. O. Govorov and H. H. Richardson, Generating Heat with Metal Nanoparticles, *Nano Today*, 2007, **2**, 30-38.

128. G. Baffou and R. Quidant, Thermo-Plasmonics: Using Metallic Nanostructures as Nano-Sources of Heat, *Laser Photonics Rev.*, 2013, **7**, 171-187.

129. J. Chen, H. Cong, F.-C. Loo, Z. Kang, M. Tang, H. Zhang, S.-Y. Wu, S.-K. Kong and H.-P. Ho, Thermal Gradient Induced Tweezers for the Manipulation of Particles and Cells, *Scientific Reports*, 2016, **6**, 35814.

130. L. Lin, X. Peng, M. Wang, L. Scarabelli, Z. Mao, L. M. Liz-Marzán, M. F. Becker and Y. Zheng, Light-Directed Reversible Assembly of Plasmonic Nanoparticles Using Plasmon-Enhanced Thermophoresis, *ACS Nano*, 2016, **10**, 9659-9668.

131. B. Nikoobakht and M. A. El-Sayed, Evidence for Bilayer Assembly of Cationic Surfactants on the Surface of Gold Nanorods, *Langmuir*, 2001, **17**, 6368-6374.

132. D. K. Smith and B. A. Korgel, The Importance of the CTAB Surfactant on the Colloidal Seed-Mediated Synthesis of Gold Nanorods, *Langmuir*, 2008, **24**, 644-649.

133. T. F. Tadros, in *Applied Surfactants: Principles and Applications*, Wiley-VCH Verlag GmbH & Co. KGaA, Weinheim, 2005, DOI: 10.1002/3527604812.ch3, ch. 3, pp. 53-72.

134. A. Majee and A. Würger, Charging of Heated Colloidal Particles Using the Electrolyte Seebeck Effect, *Phys. Rev. Lett.*, 2012, **108**, 118301.

135. D. A. Amos, J. H. Markels, S. Lynn and C. J. Radke, Osmotic Pressure and Interparticle Interactions in Ionic Micellar Surfactant Solutions, *J. Phys. Chem. B*, 1998, **102**, 2739-2753.

136. D. Vigolo, S. Buzzaccaro and R. Piazza, Thermophoresis and Thermoelectricity in Surfactant Solutions, *Langmuir*, 2010, **26**, 7792-7801.

137. J. Prikulis, F. Svedberg, M. Käll, J. Enger, K. Ramser, M. Goksör and D. Hanstorp, Optical Spectroscopy of Single Trapped Metal Nanoparticles in Solution, *Nano Lett.*, 2004, **4**, 115-118.

138. V. Demergis and E.-L. Florin, Ultrastrong Optical Binding of Metallic Nanoparticles, *Nano Lett.*, 2012, **12**, 5756-5760.

139. T. D. Iracki, D. J. Beltran-Villegas, S. L. Eichmann and M. A. Bevan, Charged Micelle Depletion Attraction and Interfacial Colloidal Phase Behavior, *Langmuir*, 2010, **26**, 18710-18717.

140. A. Ohlinger, S. Nedev, A. A. Lutich and J. Feldmann, Optothermal Escape of Plasmonically Coupled Silver Nanoparticles from a Three-Dimensional Optical Trap, *Nano Lett.*, 2011, **11**, 1770-1774.

141. L. Tong, V. D. Miljković, P. Johansson and M. Käll, Plasmon Hybridization Reveals the Interaction between Individual Colloidal Gold Nanoparticles Confined in an Optical Potential Well, *Nano Lett.*, 2011, **11**, 4505-4508.

142. M. Blattmann and A. Rohrbach, Plasmonic Coupling Dynamics of Silver Nanoparticles in an Optical Trap, *Nano Lett.*, 2015, **15**, 7816-7821.

143. N. J. Halas, S. Lal, W. S. Chang, S. Link and P. Nordlander, Plasmons in Strongly Coupled Metallic Nanostructures, *Chem. Rev.*, 2011, **111**, 3913-3961.

144. B. Lee, J. Park, G. H. Han, H.-S. Ee, C. H. Naylor, W. Liu, A. T. C. Johnson and R. Agarwal, Fano Resonance and Spectrally Modified Photoluminescence Enhancement in Monolayer MoS2 Integrated with Plasmonic Nanoantenna Array, *Nano Lett.*, 2015, **15**, 3646-3653.

145. R. Chikkaraddy, B. de Nijs, F. Benz, S. J. Barrow, O. A. Scherman, E. Rosta, A. Demetriadou, P. Fox, O. Hess and J. J. Baumberg, Single-Molecule Strong Coupling at Room Temperature in Plasmonic Nanocavities, *Nature*, 2016, **535**, 127-130.

146. Z. Zhu, W. Liu, Z. Li, B. Han, Y. Zhou, Y. Gao and Z. Tang, Manipulation of Collective Optical Activity in One-Dimensional Plasmonic Assembly, *ACS Nano*, 2012, **6**, 2326-2332.

147. W. Liu, Z. Zhu, K. Deng, Z. Li, Y. Zhou, H. Qiu, Y. Gao, S. Che and Z. Tang, Gold Nanorod@Chiral Mesoporous Silica Core–shell Nanoparticles with Unique Optical Properties, *J. Am. Chem. Soc.*, 2013, **135**, 9659-9664.

148. K. G. Stamplecoskie, J. C. Scaiano, V. S. Tiwari and H. Anis, Optimal Size of Silver Nanoparticles for Surface-Enhanced Raman Spectroscopy, *J. Phys. Chem. C*, 2011, **115**, 1403-1409.

149. J. J. Mock, M. Barbic, D. R. Smith, D. A. Schultz and S. Schultz, Shape Effects in Plasmon Resonance of Individual Colloidal Silver Nanoparticles, *J. Chem. Phys.*, 2002, **116**, 6755-6759.

150. N. E. Motl, A. F. Smith, C. J. DeSantis and S. E. Skrabalak, Engineering Plasmonic Metal Colloids through Composition and Structural Design, *Chem. Soc. Rev.*, 2014, **43**, 3823-3834.

151. K. H. Su, Q. H. Wei, X. Zhang, J. J. Mock, D. R. Smith and S. Schultz, Interparticle Coupling Effects on Plasmon Resonances of Nanogold Particles, *Nano Lett.*, 2003, **3**, 1087-1090.

152. Z. Zhu, H. Meng, W. Liu, X. Liu, J. Gong, X. Qiu, L. Jiang, D. Wang and Z. Tang, Superstructures and SERS Properties of Gold Nanocrystals with Different Shapes, *Angew. Chem. Int. Ed.*, 2011, **50**, 1593-1596.

153. P. P. Patra, R. Chikkaraddy, R. P. N. Tripathi, A. Dasgupta and G. V. P. Kumar, Plasmofluidic Single-Molecule Surface-Enhanced Raman Scattering from Dynamic Assembly of Plasmonic Nanoparticles, *Nature Commun.*, 2014, **5**, 4357.

154. B. Fazio, C. D'Andrea, A. Foti, E. Messina, A. Irrera, M. G. Donato, V. Villari, N. Micali, O. M. Maragò and P. G. Gucciardi, SERS Detection of Biomolecules at Physiological pH *via* Aggregation of Gold Nanorods Mediated by Optical Forces and Plasmonic Heating, *Scientific Reports*, 2016, **6**, 26952.

155. J. Ye, F. Wen, H. Sobhani, J. B. Lassiter, P. V. Dorpe, P. Nordlander and N. J. Halas, Plasmonic Nanoclusters: Near Field Properties of the Fano Resonance Interrogated with SERS, *Nano Lett.*, 2012, **12**, 1660-1667.

156. P. Taladriz-Blanco, N. J. Buurma, L. Rodriguez-Lorenzo, J. Perez-Juste, L. M. Liz-Marzan and P. Herves, Reversible Assembly of Metal Nanoparticles Induced by Penicillamine. Dynamic Formation of SERS Hot Spots, *J. Mater. Chem.*, 2011, **21**, 16880-16887.

157. W. Li, I. Kanyo, C.-H. Kuo, S. Thanneeru and J. He, pH-Programmable Self-Assembly of Plasmonic Nanoparticles: Hydrophobic Interaction Versus Electrostatic Repulsion, *Nanoscale*, 2015, **7**, 956-964.

158. Z. Li, Z. Zhu, W. Liu, Y. Zhou, B. Han, Y. Gao and Z. Tang, Reversible Plasmonic Circular Dichroism of Au Nanorod and DNA Assemblies, *J. Am. Chem. Soc.*, 2012, **134**, 3322-3325.

159. Y. Liu, X. Han, L. He and Y. Yin, Thermoresponsive Assembly of Charged Gold Nanoparticles and Their Reversible Tuning of Plasmon Coupling, *Angew. Chem. Int. Ed.*, 2012, **51**, 6373-6377.

160. S. Si, M. Raula, T. K. Paira and T. K. Mandal, Reversible Self-Assembly of Carboxylated Peptide-Functionalized Gold Nanoparticles Driven by Metal-Ion Coordination, *ChemPhysChem*, 2008, **9**, 1578-1584.

161. B. Su, J.-P. Abid, D. J. Fermín, H. H. Girault, H. Hoffmannová, P. Krtil and Z. Samec, Reversible Voltage-Induced Assembly of Au Nanoparticles at Liquid|Liquid Interfaces, *J. Am. Chem. Soc.*, 2004, **126**, 915-919.

162. R. Klajn, K. J. M. Bishop and B. A. Grzybowski, Light-Controlled Self-Assembly of Reversible and Irreversible Nanoparticle Suprastructures, *Proc. Natl. Acad. Sci. U. S. A.*, 2007, **104**, 10305-10309.

163. P. K. Kundu, D. Samanta, R. Leizrowice, B. Margulis, H. Zhao, M. Börner, UdayabhaskararaoT, D. Manna and R. Klajn, Light-Controlled Self-Assembly of Non-Photoresponsive Nanoparticles, *Nature Chem.*, 2015, **7**, 646-652.

164. Y. Bao, Z. Yan and N. F. Scherer, Optical Printing of Electrodynamically Coupled Metallic Nanoparticle Arrays, *J. Phys. Chem. C*, 2014, **118**, 19315-19321.

165. J. Gargiulo, S. Cerrota, E. Cortés, I. L. Violi and F. D. Stefani, Connecting Metallic Nanoparticles by Optical Printing, *Nano Lett.*, 2016, **16**, 1224-1229.

166. M. J. Guffey and N. F. Scherer, All-Optical Patterning of Au Nanoparticles on Surfaces Using Optical Traps, *Nano Lett.*, 2010, **10**, 4302-4308.

167. A. Kyrsting, P. M. Bendix, D. G. Stamou and L. B. Oddershede, Heat Profiling of Three-Dimensionally Optically Trapped Gold Nanoparticles using Vesicle Cargo Release, *Nano Lett.*, 2011, **11**, 888-892.

168. S. D. Brown, P. Nativo, J.-A. Smith, D. Stirling, P. R. Edwards, B. Venugopal, D. J. Flint, J. A. Plumb, D. Graham and N. J. Wheate, Gold Nanoparticles for the Improved Anticancer Drug Delivery of the Active Component of Oxaliplatin, *J. Am. Chem. Soc.*, 2010, **132**, 4678-4684.

169. L. Tong, M. Righini, M. U. Gonzalez, R. Quidant and M. Kall, Optical Aggregation of Metal Nanoparticles in a Microfluidic Channel for Surface-Enhanced Raman Scattering Analysis, *Lab Chip*, 2009, **9**, 193-195.

170. E. Messina, E. Cavallaro, A. Cacciola, R. Saija, F. Borghese, P. Denti, B. Fazio, C. D'Andrea, P. G. Gucciardi, M. A. Iatì, M. Meneghetti, G. Compagnini, V. Amendola and O. M. Maragò, Manipulation and Raman Spectroscopy with Optically Trapped Metal Nanoparticles Obtained by Pulsed Laser Ablation in Liquids, *J. Phys. Chem. C*, 2011, **115**, 5115-5122.

171. I. Y. Stetciura, A. Yashchenok, A. Masic, E. V. Lyubin, O. A. Inozemtseva, M. G. Drozdova, E. A. Markvichova, B. N. Khlebtsov, A. A. Fedyanin, G. B. Sukhorukov, D. A. Gorin and D. Volodkin, Composite SERS-Based Satellites Navigated by Optical Tweezers for Single Cell Analysis, *Analyst*, 2015, **140**, 4981-4986.

172. F. Svedberg, Z. Li, H. Xu and M. Käll, Creating Hot Nanoparticle Pairs for Surface-Enhanced Raman Spectroscopy through Optical Manipulation, *Nano Lett.*, 2006, **6**, 2639-2641.

173. H. Yoshikawa, T. Matsui and H. Masuhara, Reversible Assembly of Gold Nanoparticles Confined in an Optical Microcage, *Phys. Rev. E*, 2004, **70**, 061406.

174. G. González-Rubio, A. Guerrero-Martínez and L. M. Liz-Marzán, Reshaping, Fragmentation, and Assembly of Gold Nanoparticles Assisted by Pulse Lasers, *Acc. Chem. Res.*, 2016, **49**, 678-686.

175. G. González-Rubio, J. González-Izquierdo, L. Bañares, G. Tardajos, A. Rivera, T. Altantzis, S. Bals, O. Peña-Rodríguez, A. Guerrero-Martínez and L. M. Liz-Marzán, Femtosecond Laser-Controlled Tip-to-Tip Assembly and Welding of Gold Nanorods, *Nano Lett.*, 2015, **15**, 8282-8288.

176. L. Scarabelli, M. Coronado-Puchau, J. J. Giner-Casares, J. Langer and L. M. Liz-Marzán, Monodisperse Gold Nanotriangles: Size Control, Large-Scale Self-Assembly, and Performance in Surface-Enhanced Raman Scattering, *ACS Nano*, 2014, **8**, 5833-5842.

177. R. Jin, Y. Cao, C. A. Mirkin, K. L. Kelly, G. C. Schatz and J. G. Zheng, Photoinduced Conversion of Silver Nanospheres to Nanoprisms, *Science*, 2001, **294**, 1901-1903.

178. C. Pignolet, M. Euvrard, A. Foissy and C. Filiâtre, Electrodeposition of Latex Particles in the Presence of Surfactant: Investigation of Deposit Morphology, *J. Colloid Interface Sci.*, 2010, **349**, 41-48.

179. S. Gómez-Graña, F. Hubert, F. Testard, A. Guerrero-Martínez, I. Grillo, L. M. Liz-Marzán and O. Spalla, Surfactant (Bi)Layers on Gold Nanorods, *Langmuir*, 2012, **28**, 1453-1459.

180. T. G. Movchan, I. V. Soboleva, E. V. Plotnikova, A. K. Shchekin and A. I. Rusanov, Dynamic Light Scattering Study of Cetyltrimethylammonium Bromide Aqueous Solutions, *Colloid J.*, 2012, **74**, 239-247.

181. L. Lin, X. Peng, Z. Mao, W. Li, M. N. Yogeesh, B. B. Rajeeva, E. P. Perillo, A. K. Dunn, D. Akinwande and Y. Zheng, Bubble-Pen Lithography, *Nano Lett.*, 2016, **16**, 701-708.

182. S. Nie and S. R. Emory, Probing Single Molecules and Single Nanoparticles by Surface-Enhanced Raman Scattering, *Science*, 1997, **275**, 1102-1106.

183. A. Campion and P. Kambhampati, Surface-Enhanced Raman Scattering, *Chem. Soc. Rev.*, 1998, **27**, 241-250.

184. K. Kneipp, Y. Wang, H. Kneipp, L. T. Perelman, I. Itzkan, R. R. Dasari and M. S. Feld, Single Molecule Detection Using Surface-Enhanced Raman Scattering (SERS), *Phys. Rev. Lett.*, 1997, **78**, 1667-1670.

185. P. L. Stiles, J. A. Dieringer, N. C. Shah and R. P. V. Duyne, Surface-Enhanced Raman Spectroscopy, *Annu. Rev. Anal. Chem.*, 2008, **1**, 601-626.

186. A. Garcia-Leis, J. V. Garcia-Ramos and S. Sanchez-Cortes, Silver Nanostars with High SERS Performance, *J. Phys. Chem. C*, 2013, **117**, 7791-7795.

187. J. M. McLellan, Z.-Y. Li, A. R. Siekkinen and Y. Xia, The SERS Activity of a Supported Ag Nanocube Strongly Depends on Its Orientation Relative to Laser Polarization, *Nano Lett.*, 2007, **7**, 1013-1017.

188. H. Wang, C. S. Levin and N. J. Halas, Nanosphere Arrays with Controlled Sub-10-nm Gaps as Surface-Enhanced Raman Spectroscopy Substrates, *J. Am. Chem. Soc.*, 2005, **127**, 14992-14993.

189. D.-K. Lim, K.-S. Jeon, J.-H. Hwang, H. Kim, S. Kwon, Y. D. Suh and J.-M. Nam, Highly Uniform and Reproducible Surface-Enhanced Raman Scattering from DNA-Tailorable Nanoparticles with 1-nm Interior Gap, *Nature Nanotechnol.*, 2011, **6**, 452-460.

190. S. Chen, L.-Y. Meng, H.-Y. Shan, J.-F. Li, L. Qian, C. T. Williams, Z.-L. Yang and Z.-Q. Tian, How to Light Special Hot Spots in Multiparticle–Film Configurations, *ACS Nano*, 2015, **10**, 581-587.

191. S. H. Shams Mousavi, A. A. Eftekhar, A. H. Atabaki and A. Adibi, Band-Edge Bilayer Plasmonic Nanostructure for Surface Enhanced Raman Spectroscopy, *ACS Photonics*, 2015, **2**, 1546-1551.

192. W. Li, P. H. C. Camargo, X. Lu and Y. Xia, Dimers of Silver Nanospheres: Facile Synthesis and Their Use as Hot Spots for Surface-Enhanced Raman Scattering, *Nano Lett.*, 2009, **9**, 485-490.

193. P. Hildebrandt and M. Stockburger, Surface-Enhanced Resonance Raman Spectroscopy of Rhodamine 6G Adsorbed on Colloidal Silver, *J. Phys. Chem.*, 1984, **88**, 5935-5944.

194. U. Kreibig and M. Vollmer, *Optical Properties of Metal Clusters*, Springer, Berlin, 1995.

195. D. V. Talapin, J.-S. Lee, M. V. Kovalenko and E. V. Shevchenko, Prospects of Colloidal Nanocrystals for Electronic and Optoelectronic Applications, *Chem. Rev.*, 2010, **110**, 389-458.

196. S. Sun, C. B. Murray, D. Weller, L. Folks and A. Moser, Monodisperse FePt Nanoparticles and Ferromagnetic FePt Nanocrystal Superlattices, *Science*, 2000, **287**, 1989-1992.

197. M. Bruchez, M. Moronne, P. Gin, S. Weiss and A. P. Alivisatos, Semiconductor Nanocrystals as Fluorescent Biological Labels, *Science*, 1998, **281**, 2013-2016.

198. Y. A. Vlasov, X.-Z. Bo, J. C. Sturm and D. J. Norris, On-Chip Natural Assembly of Silicon Photonic Bandgap Crystals, *Nature*, 2001, **414**, 289-293.

199. G. von Freymann, V. Kitaev, B. V. Lotsch and G. A. Ozin, Bottom-up Assembly of Photonic Crystals, *Chem. Soc. Rev.*, 2013, **42**, 2528-2554.

200. E. A. Kamenetzky, L. G. Magliocco and H. P. Panzer, Structure of Solidified Colloidal Array Laser Filters Studied by Cryogenic Transmission Electron Microscopy, *Science*, 1994, **263**, 207-210.

201. S. H. Park and Y. Xia, Assembly of Mesoscale Particles over Large Areas and Its Application in Fabricating Tunable Optical Filters, *Langmuir*, 1999, **15**, 266-273.

202. L. Huang, C.-J. Wang and L. Y. Lin, Comparison of Cross-Talk Effects between Colloidal Quantum Dot and Conventional Waveguides, *Opt. Lett.*, 2007, **32**, 235-237.

203. P. D. Howes, R. Chandrawati and M. M. Stevens, Colloidal Nanoparticles as Advanced Biological Sensors, *Science*, 2014, **346**, 1247390.

204. H. Jans and Q. Huo, Gold Nanoparticle-Enabled Biological and Chemical Detection and Analysis, *Chem. Soc. Rev.*, 2012, **41**, 2849-2866.

205. S. C. Glotzer, M. J. Solomon and N. A. Kotov, Self-Assembly: From Nanoscale to Microscale Colloids, *AIChE J.*, 2004, **50**, 2978-2985.

206. L. V. Andreeva, A. V. Koshkin, P. V. Lebedev-Stepanov, A. N. Petrov and M. V. Alfimov, Driving Forces of the Solute Self-Organization in an Evaporating Liquid Microdroplet, *Colloids Surf., A*, 2007, **300**, 300-306.

207. P. J. Yunker, T. Still, M. A. Lohr and A. G. Yodh, Suppression of the Coffee-Ring Effect by Shape-Dependent Capillary Interactions, *Nature*, 2011, **476**, 308-311.

208. E. Tekin, P. J. Smith and U. S. Schubert, Inkjet Printing as a Deposition and Patterning Tool for Polymers and Inorganic Particles, *Soft Matter*, 2008, **4**, 703-713.

209. M. Singh, H. M. Haverinen, P. Dhagat and G. E. Jabbour, Inkjet Printing—Process and Its Applications, *Adv. Mater.*, 2010, **22**, 673-685.

210. S. Ito, H. Yoshikawa and H. Masuhara, Optical Patterning and Photochemical Fixation of Polymer Nanoparticles on Glass Substrates, *Appl. Phys. Lett.*, 2001, **78**, 2566-2568.

211. D. Walker, D. P. Singh and P. Fischer, Capture of 2D Microparticle Arrays *via* a UV-Triggered Thiol-yne "Click" Reaction, *Adv. Mater.*, 2016, **28**, 9846-9850.

212. J. Do, M. Fedoruk, F. Jäckel and J. Feldmann, Two-Color Laser Printing of Individual Gold Nanorods, *Nano Lett.*, 2013, **13**, 4164-4168.

213. J. P. Hoogenboom, D. L. J. Vossen, C. Faivre-Moskalenko, M. Dogterom and A. v. Blaaderen, Patterning Surfaces with Colloidal Particles Using Optical Tweezers, *Appl. Phys. Lett.*, 2002, **80**, 4828-4830.

214. D. Vigolo, R. Rusconi, H. A. Stone and R. Piazza, Thermophoresis: Microfluidics Characterization and Separation, *Soft Matter*, 2010, **6**, 3489-3493.

215. J. D. Joannopoulos, P. R. Villeneuve and S. Fan, Photonic Crystals: Putting a New Twist on Light, *Nature*, 1997, **386**, 143-149.

216. R. Xie and X.-Y. Liu, Electrically Directed On-Chip Reversible Patterning of Two-Dimensional Tunable Colloidal Structures, *Adv. Funct. Mater.*, 2008, **18**, 802-809.

217. R. Xie and X.-Y. Liu, Controllable Epitaxial Crystallization and Reversible Oriented Patterning of Two-Dimensional Colloidal Crystals, *J. Am. Chem. Soc.*, 2009, **131**, 4976-4982.

218. S. Duhr and D. Braun, Thermophoretic Depletion Follows Boltzmann Distribution, *Phys. Rev. Lett.*, 2006, **96**, 168301.

219. W. Alois, Thermal Non-Equilibrium Transport in Colloids, *Rep. Prog. Phys.*, 2010, **73**, 126601.

220. M.-P. Valignat, O. Theodoly, J. C. Crocker, W. B. Russel and P. M. Chaikin, Reversible Self-Assembly and Directed Assembly of DNA-Linked Micrometer-Sized Colloids, *Proc. Natl. Acad. Sci. U. S. A.*, 2005, **102**, 4225-4229.

221. B. D. Gates, Q. Xu, J. C. Love, D. B. Wolfe and G. M. Whitesides, Unconventional Nanofabrication, *Annu. Rev. Mater. Res.*, 2004, **34**, 339-372.

222. B. D. Gates, Q. Xu, M. Stewart, D. Ryan, C. G. Willson and G. M. Whitesides, New Approaches to Nanofabrication: Molding, Printing, and Other Techniques, *Chem. Rev.*, 2005, **105**, 1171-1196.

223. S. R. Quake and A. Scherer, From Micro- to Nanofabrication with Soft Materials, *Science*, 2000, **290**, 1536-1540.

224. M. Shimomura and T. Sawadaishi, Bottom-Up Strategy of Materials Fabrication: A New Trend in Nanotechnology of Soft Materials, *Curr. Opin. Colloid Interface Sci.*, 2001, **6**, 11-16.

225. J. W. Durham and Y. Zhu, Fabrication of Functional Nanowire Devices on Unconventional Substrates Using Strain-Release Assembly, *ACS Appl. Mater. Interfaces*, 2013, **5**, 256-261.

226. Y. Wu, N. Dong, S. Fu, J. D. Fowlkes, L. Kondic, M. A. Vincenti, D. de Ceglia and P. D. Rack, Directed Liquid Phase Assembly of Highly Ordered Metallic Nanoparticle Arrays, *ACS Appl. Mater. Interfaces*, 2014, **6**, 5835-5843.

227. T. Liu, T. Keiper, X. Wang, G. Yang, D. Hallinan, J. Zhao and P. Xiong, Molecular Patterning and Directed Self-Assembly of Gold Nanoparticles on GaAs, *ACS Appl. Mater. Interfaces*, 2017, **9**, 43363-43369.

228. S.-M. Yang, S.-H. Kim, J.-M. Lim and G.-R. Yi, Synthesis and Assembly of Structured Colloidal Particles, *J. Mater. Chem.*, 2008, **18**, 2177-2190.

229. S.-L. Kuai, X.-F. Hu, A. Haché and V.-V. Truong, High-quality Colloidal Photonic Crystals Obtained by Optimizing Growth Parameters in a Vertical Deposition Technique, *J. Cryst. Growth*, 2004, **267**, 317-324.

230. O. D. Velev and E. W. Kaler, *In Situ* Assembly of Colloidal Particles into Miniaturized Biosensors, *Langmuir*, 1999, **15**, 3693-3698.

231. A.-P. Hynninen, J. H. J. Thijssen, E. C. M. Vermolen, M. Dijkstra and A. van Blaaderen, Self-Assembly Route for Photonic Crystals with a Bandgap in the Visible Region, *Nature Mater.*, 2007, **6**, 202.

232. G. M. Whitesides and B. Grzybowski, Self-Assembly at All Scales, *Science*, 2002, **295**, 2418-2421.

233. Y. Tian, T. Wang, W. Liu, H. L. Xin, H. Li, Y. Ke, W. M. Shih and O. Gang, Prescribed Nanoparticle Cluster Architectures and Low-Dimensional Arrays Built Using Octahedral DNA Origami Frames, *Nature Nanotechnol.*, 2015, **10**, 637.

234. O. Gang and A. V. Tkachenko, DNA-Programmable Particle Superlattices: Assembly, Phases, and Dynamic Control, *MRS Bull.*, 2016, **41**, 381-387.

235. Q.-Y. Lin, J. A. Mason, Z. Li, W. Zhou, M. N. O'Brien, K. A. Brown, M. R. Jones, S. Butun, B. Lee, V. P. Dravid, K. Aydin and C. A. Mirkin, Building Superlattices

from Individual Nanoparticles *via* Template-Confined DNA-Mediated Assembly, *Science*, 2018, **359**, 669-672.

236. N. B. Schade, M. C. Holmes-Cerfon, E. R. Chen, D. Aronzon, J. W. Collins, J. A. Fan, F. Capasso and V. N. Manoharan, Tetrahedral Colloidal Clusters from Random Parking of Bidisperse Spheres, *Phys. Rev. Lett.*, 2013, **110**, 148303.

237. V. V. Thacker, L. O. Herrmann, D. O. Sigle, T. Zhang, T. Liedl, J. J. Baumberg and U. F. Keyser, DNA Origami Based Assembly of Gold Nanoparticle Dimers for Surface-Enhanced Raman Scattering, *Nature Commun.*, 2014, **5**, 3448.

238. P. Kühler, E.-M. Roller, R. Schreiber, T. Liedl, T. Lohmüller and J. Feldmann, Plasmonic DNA-Origami Nanoantennas for Surface-Enhanced Raman Spectroscopy, *Nano Lett.*, 2014, **14**, 2914-2919.

239. A. Kuzyk, R. Schreiber, Z. Fan, G. Pardatscher, E.-M. Roller, A. Högele, F. C. Simmel, A. O. Govorov and T. Liedl, DNA-Based Self-Assembly of Chiral Plasmonic Nanostructures with Tailored Optical Response, *Nature*, 2012, **483**, 311.

240. X. Shen, A. Asenjo-Garcia, Q. Liu, Q. Jiang, F. J. García de Abajo, N. Liu and B. Ding, Three-Dimensional Plasmonic Chiral Tetramers Assembled by DNA Origami, *Nano Lett.*, 2013, **13**, 2128-2133.

241. C. Mio and D. W. M. Marr, Optical Trapping for the Manipulation of Colloidal Particles, *Adv. Mater.*, 2000, **12**, 917-920.

242. A. S. Urban, S. Carretero-Palacios, A. A. Lutich, T. Lohmuller, J. Feldmann and F. Jackel, Optical Trapping and Manipulation of Plasmonic Nanoparticles: Fundamentals, Applications, and Perspectives, *Nanoscale*, 2014, **6**, 4458-4474.

243. L. A. Shaw, S. Chizari, R. M. Panas, M. Shusteff, C. M. Spadaccini and J. B. Hopkins, Holographic Optical Assembly and Photopolymerized Joining of Planar Microspheres, *Opt. Lett.*, 2016, **41**, 3571-3574.

244. J. Gargiulo, T. Brick, I. L. Violi, F. C. Herrera, T. Shibanuma, P. Albella, F. G. Requejo, E. Cortes, S. A. Maier and F. D. Stefani, Understanding and Reducing Photothermal Forces for the Fabrication of Au Nanoparticle Dimers by Optical Printing, *Nano Lett.*, 2017, **17**, 5747-5755.

245. J. Chen, Z. Kang, S. K. Kong and H.-P. Ho, Plasmonic Random Nanostructures on Fiber Tip for Trapping Live Cells and Colloidal Particles, *Opt. Lett.*, 2015, **40**, 3926-3929.

246. L. Aboubakry, M. Arghya and W. Alois, Nanoscale Seebeck Effect at Hot Metal Nanostructures, *New J. Phys.*, 2018, **20**, 025001.

247. L. Lin, M. Wang, X. Peng, E. N. Lissek, Z. Mao, L. Scarabelli, E. Adkins, S. Coskun, H. E. Unalan, B. A. Korgel, L. M. Liz-Marzán, E.-L. Florin and Y. Zheng, Opto-Thermoelectric Nanotweezers, *Nature Photon.*, 2018, **12**, 195-201.

248. K. C. Neuman and S. M. Block, Optical Trapping, *Rev. Sci. Instrum.*, 2004, **75**, 2787-2809.

249. B. J. Roxworthy, A. M. Bhuiya, S. P. Vanka and K. C. Toussaint Jr, Understanding and Controlling Plasmon-Induced Convection, *Nature Commun.*, 2014, **5**, 3173.

250. K. Holmberg, B. Jönsson, B. Kronberg and B. Lindman, *Surfactants and Polymers in Aqueous Solution*, Wiley Online Library, 2003.

251. L. Shi, J. T. Harris, R. Fenollosa, I. Rodriguez, X. Lu, B. A. Korgel and F. Meseguer, Monodisperse Silicon Nanocavities and Photonic Crystals with Magnetic Response in the Optical Region, *Nature Commun.*, 2013, **4**, 1904.